Systematic Development and Characterization of a Polypyrrole Hybrid for Dynamic Random Access Memory

by

Matt Andrew Pilapil

A Thesis submitted to the Faculty of Graduate Studies of the University of Manitoba in partial fulfillment of the requirements for the degree of

Master of Science

Department of Chemistry
University of Manitoba
Winnipeg, Manitoba, Canada

Abstract

Conducting polymers have emerged as a class of innovative materials with tunable properties that are useful in a diverse range of applications. For example, the electronic properties and molecular structure of these materials can be modified electrochemically. Reported in 2008, the creation of a conducting polymer hybrid system PPy(Li^+DBS^-) that exhibits novel time and potential dependent conductivity can be utilized to create dynamic memory. Unlike modern silicon-based devices which are limited by scaling factors such as quantum tunneling, this system is expected to have exceptional scaling properties allowing memory devices to operate down to the low nm range. The work embodied within this thesis describes results based on the scaling properties of PPy(Li^+DBS^-) from 5 to 45 μm on the potential dependent current transients that are used as a basis for dynamic memory applications. The deviation from theorized conduction systems has led to a thorough understanding of the anisotropic nature of PPy(Li^+DBS^-) determined through finite elemental simulation methods. The temperature dependence of the system is also studied to verify activation energies associated with carrier and ion mobility.

Dedication

This thesis is dedicated to my grandmother (my mother's mother), Lola Teresa Maranon or simply known as Lola. From the beginning of my education at the University of Manitoba Lola was gracious enough to take me into her home. She treated me as though I was one of her own children from making sure I was well fed to being clothed. Lola's kindness and hospitality was not granted with anything in return; all she asked was to see me complete my studies and become successful at whatever I chose to do. Unfortunately she will not be here to see that day as Lola passed away suddenly on January 24, 2009.

Lola, I could never express in words or actions my gratitude of your love and support for me but whatever I continue do will be a tribute to your life. To all those that we have loved and lost thank you for being there when you could.

Acknowledgements

I would like to thank the numerous people who have assisted in the work contained within this thesis:

First of all, my supervisors, Dr. Freund and Dr. Thomson, for giving me the opportunity to work on a remarkable project, as they were able to give me a significant amount of guidance, and support. Their time, patience and knowledge were greatly appreciated.

Secondly, members of the Freund and Thomson research group: Rajesh Pillai, Jun Hui Zhao, Graeme Suppes, Mike McDonald, Denise McInnes, Dr. Bhavana Deore, Dr. Sergei Rudenja, Dr. Amin Rahman, Dr. Eftekhar Hossain, Dr. Shaune McFarlane, and Dr. Kevin McEleney (the SEM images you obtained are simply magnificent).

Dwayne Chrusch and all involved with the NSFL for the technical assistance with the microfabrication process of our device.

Dr. Greg Bridges and Graham Ferrier for their guidance with the COMSOL simulations.

Members of the defense committee, Dr. Douglas Buchanan, and Dr. Jennifer van Wijingaarden.

Brandy Kinkead and Kathy Black for the many times they helped me through the rough days of editing.

Justin Rak-Banville for all the technological assistance within this technology laden era.

Everyone in the Chemistry Department.

Finally, my friends, and family that helped support me through the many years of my education.

Table of Contents

List of Figures

List of Schemes

Chapter 1 Introduction and Background

1.1 Memory Devices and Designs

1.1.1 Introduction

The ever-increasing world of technology continues to produce revolutionary changes within computers and electronics. An important technological component of these many devices is digital memory, typically used to store digital data. The digital form of data is based solely on a binary language of ones (1s) and zeros (0s), which are commonly referred to as binary digits (bits). The addressable unit of digital data is based on eight bits which correspond to a byte; these bytes can be accessed via large portions where every four or eight bytes result in a single word. Word length is dependent upon several factors such as the computing system, memory type, and the particular mode of retrieval.[1-3]

There are two primary uses of digital data which can either be for temporary retention or long term storage. Mass storage devices such as optical media (CDs and DVDs), magnetic devices (hard disk drives) and flash memory (USB flash drives) are often used for storing copious amounts of digital data for extended periods of time. Flash memory has gained considerable attention as this is a specific type of non-volatile electrically erasable programmable read only memory (EEPROM) altered by high potentials. A major shortfall of mass storage devices are the rotary mechanisms (CDs, DVDs and hard disk drives) or large memory bytes (flash memory) which take a longer period of time to

retrieve data; though they are advantageous in their ability to retain data upon the removal of power (non-volatile).

In contrast, the storage and retrieval of temporary data is several orders of magnitude faster than that of mass storage devices but requires constant power to retain information (volatile). Random access memory (RAM), a common type of volatile memory, can provide temporary data storage and retrieval in a constant period of time as there is no physical movement of mechanical parts. While there is always a need for long term data storage, RAM has the ability to retain momentary data through a few cycles. RAM can allow electronic devices to perform and execute a multitude of tasks at a given time, which is important for the increasing need for faster technology, but is highly volatile due to its inability to store data without a continuous applied potential .[1-3]

Cost and performance are critical figures of merit in the design and fabrication of conventional RAM devices. The elevated cost of fabricating high performance devices is mainly due to the capital costs; including but not limited to the sophisticated lithographic process, sterile environments (low particle density) and the purity of materials required. In contrast, a lower performance device can be fabricated in a few steps resulting in a product with a significantly reduced cost. With current processing techniques, typical RAM devices are limited by the materials they are comprised of. Essentially, researchers are being compelled to design new and innovative materials for RAM devices that can be competitive with current technology. The goal of novel

materials for memory devices is to increase performance without having to increase fabrication costs. [1-5]

1.1.2 Dynamic Random Access Memory

The first patent for dynamic random access memory (DRAM) was filed by Dennard in 1967 while working in conjunction with IBM. Within 5 years, IBM released a commercial product that began a new era in computing.[6] Currently RAM architecture comes in two forms, static RAM (SRAM), which uses cross coupling inverter circuits (flip-flop), and dynamic RAM (DRAM), which functions through capacitor charging.[1, 2]

The impact that DRAM has had on the consumer market can be seen by the volume of DRAM units shipped per year since 1970. An increase of DRAM units shipped by bits per chip had shown a 4 fold increase every year until the 128 megabit (Mb) product was introduced to the market in 1996; the shipping rates had increased then began to slow down to a rate of 2 fold per year.[7] The success of DRAM within today's markets is due to the integration within electronics and nanosecond (ns) access speeds, making them highly desirable for computing systems. The low cost factor comes from DRAMs simple design comprised of an array of 1T-1C junctions, consisting of a metal oxide semiconductor field effect transistor (MOSFET or 1T) as the switch, and a capacitor (1C) serving as the storage component (Figure 1).[1, 2]

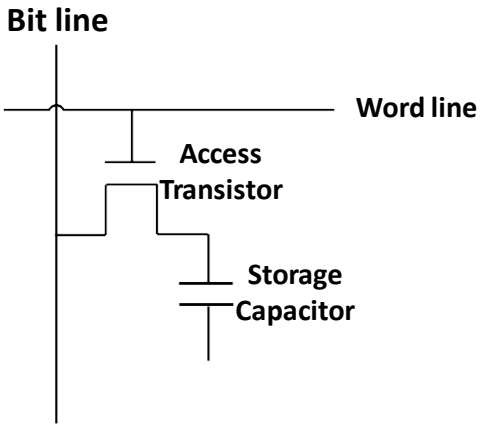

Figure 1: 1T-1C DRAM cell – The 1T-1C DRAM cell is the most common structure and design used for conventional digital memory. A single bit is charged onto a capacitor via the bit line which can be read by accessing the transistor through the word line.[2]

The success of the 1T-1C DRAM cell is attributed to the silicon (Si)-based dielectrics of Si oxide (SiO_2) and nitride (SiN_x). The transistor component of the 1T-1C cell works as a switch controlled through the horizontal word line. Applying a potential to the word line opens the FET gates to all the bits associated with that word while the potential of a particular bit line allows a single bit to be charged onto a capacitor. The storage component (i.e. the capacitor) is considered "leaky" and must be continually refreshed every ~100 milliseconds (ms) which can be addressed through computer components and programming. Once the power is lost within the system, control over the transistor and charging of the capacitor cannot be maintained therefore all data is lost; referring to the high volatility of memory retention within computing systems.[1, 2]

The corresponding SRAM cell is intricately designed with six field effect transistors (FETs) and two resistors, or simply six FETs, which designate a single bit (Figure 2).

SRAM operates using flip-flops which maintain two stable states where the “1” state has the right transistor (M3) in the on position and the left (M3) off, while the “0” state is opposite. SRAM architecture consisting solely of transistors does not need to be periodically refreshed resulting in faster access speeds, although the complexity of the device reduces density and elevates fabrication costs. SRAM is typically seen in similar technology as DRAM although they serve different purposes, with SRAM acting mainly as data buffers, cache memories, and temporary images for printers and monitors.[1, 2]

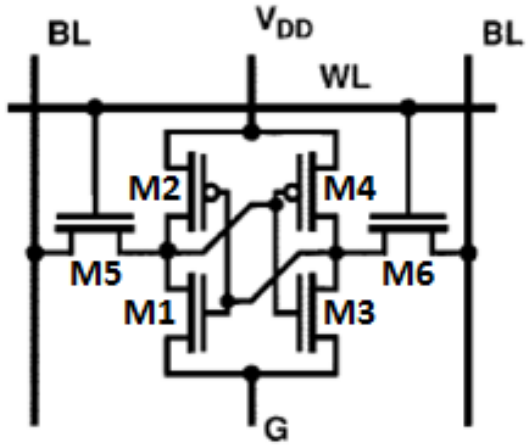

Figure 2: 6T SRAM cell – The cell is written by applying a potential to the dual bit line (*BL*) and accessed via the word line (*WL*). A positive potential (V_{DD}) is applied where the entire cell can be grounded at (*G*). The “1” state has the right transistor (M3) in the on position and the left (M3) off while the “0” state is the opposite.[8]

1.1.3 Transistors and Their Limits

Silicon-based materials are fundamental to the fabrication of transistors and integrated circuits. Planar Si based transistors began as a series of patents in 1928 by Julius Edgar [9,

[10] followed by the first experimental results from Bell Laboratories in 1947.[11] In 1960, during the Solid State Device Research Conference, the first working model of the modern Si MOSFET was presented (the transistor by which DRAM traditionally operates).[12]

After the demonstration of the first Si MOSFET, the growth of the Si industry was forecasted for nearly four decades by Moore's law whereby Gordon E. Moore (one of the Intel's co-founders) predicted that on average the number of transistors contained on an integrated circuit would double approximately every two years and thereby decrease in cost (Figure 3).[5, 13]

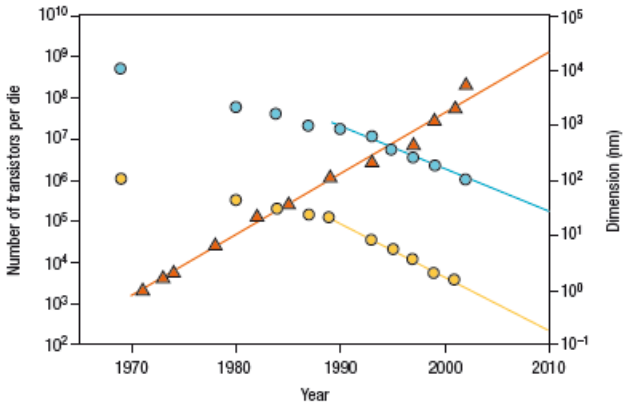

14

Figure 3: Moore's law and transistor scaling limits – Over the past 40 years the number of transistors (*red triangles*) per die have followed the exponential increase of Moore's Law, while the minimal lateral feature size (*blue circles*) and physical oxide thickness (*orange circles*) have decreased in size at the same rate that the transistor has improved in performance.

The historic trends seen in transistors predicted by Moore's law were possible due to the scaling parameters within integrated circuits.[6] Improvements within the fabrication

techniques, specifically by means of lithography and etching (wet and dry), have enabled the scaling of DRAM components down to the nanometre (nm) scale.[8]

The forecast for the steady growth of the Si industry predicted by Moore's Law is now reaching a plateau due to the scaling limits within conventional transistors.[5, 8, 15-24] Many researchers have noted to further scale down past 10 nm, MOSFETs would become highly susceptible to perturbations in structural properties resulting from quantum effects (i.e. tunnelling current).[14, 25] Industries have maximized the potential of DRAM elements and begun exploring alternative architectures and materials to surpass the barrier evident within Si based materials.[14, 23, 25] While there are alternative semiconductors being considered to replace doped Si, numerous issues still arise, therefore novel materials and architectures are being explored.[26-29]

1.1.4 Notable Innovative Materials

An increased awareness that Si-based materials are reaching their potential limits has led the International Technology Roadmap for Semiconductors (ITRS) to declare that the Si-industry has hit a "red brick wall."[5] With the confines of current materials and processes there are challenges that will be extremely difficult to meet with traditional technologies.[5] Researchers have begun exploring new, innovative materials and designs that exhibit useful electronic behaviours as a bulk property. Enabling electronic signals from the bulk of a material which does not suffer from interfacial and scaling issues

faced by standard Si-based materials can be highly beneficial.[30, 31] These materials must present electronic characteristics that are well behaved in order to be competitive with conventional materials and eventually replace what has been successful for several decades.[26-29] There have been several materials and structures created from inorganic and organic materials that demonstrate themselves as suitable alternatives for memory devices, but the ones discussed here are perhaps the most prominent: phase change materials, memristors, and organic films.

1.1.4.1 Phase Change Materials

Chalcogenide glass is a specific type of phase change material which can become highly ordered (crystalline) or disordered (amorphous) based on the specific heats of fusion (the amount of thermal energy required to alter a material from one state to another). Studied since the 1960's, chalcogenide glasses are comprised of a variable compound of germanium, antimony, and tellurium.[32] The main attraction of phase change materials for memory devices is their scaling properties which allow a single junction to be reduced down to 22 nm which is smaller than conventional Si-based devices.[30] Chemical modification through specific tuning of the elemental ratios of the alloy can control the rates of crystallization resulting in switching rates (< 50 ns) comparable to the conventional RAM devices (< 15 ns). [33, 34]

Phase change memory operates on the ability to switch between the crystalline and amorphous states by local thermal heating at a contact region. Currently the requirements to switch a material from crystalline to amorphous requires ~3 volt (V) pulse for about ~15 ns, but to switch from amorphous to crystalline only requires ~1.5 V pulse for ~75 ns. For use in memory applications, the write states of low resistance (crystalline) are used as the "1" state and the high resistance (amorphous) as the "0" while a lower potential where no change in the material occurs would be used as the read state.[30]

The use of chalcogenide glasses as non-volatile RAM (NVRAM) coupled with a MOS transistor has been thoroughly studied and the performance stability reported up to one trillion cycles.[35] Previously reported research[30, 32-35] has provided concrete evidence that chalcogenide materials are suitable for NVRAM. In 2005, Samsung announced the world's first phase change random access memory (PRAM) and later in mid 2009, the mass production of sample 512 Mb PRAM chips began.[36] With Samsung currently aware of the "red brick wall" that Si has approached, other large industry companies are likely to follow suit with alternative materials that could potentially revolutionize the electronic world.

1.1.4.2 Memristors

The evolution of passive circuitry elements began with the discovery of the capacitor in 1745, the resistor in 1827, and eventually the inductor in 1831, but later on, in 1971, Chua postulated that a fourth component, the memristor (an abbreviation for memory resistor) should also exist (Figure 4). With six possible combinations using two components of the four circuitry elements, there were three remaining combinations; two others were predefined as the physical laws of magnetism and electricity, while the last missing element Chua dubbed the memristor. The memristor would contain circuitry elements of charge and flux which would generate behaviour most similar to a nonlinear resistor with memory capabilities.[37]

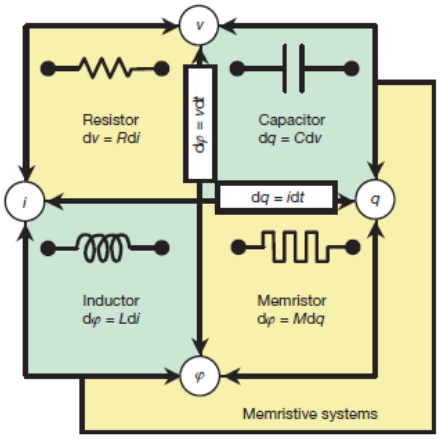

Figure 4: Circuitry elements – Chua mathematically proposed that the original three passive circuit elements could be defined using two terms from the four circuit quantities of charge, current, voltage and magnetic flux. The memristor was proposed as the fourth circuit element to contain the circuit quantities of charge and flux.[38]

Memristors could potentially revolutionize technology as they could replace existing DRAM devices and enable the retention of data without the need for a continuous potential. Computing systems would be able to continue where they left off when the power had been cycled on or off.[31] The memristor was merely a theory until 2008, when Williams et al. at HP Labs unveiled to the electronic community a physical model of a nanoscale memristor.[29, 31, 39-42] The design of the memristor consists of a platinum (Pt) crossbar array with an interstitial layer of titanium oxide (TiO_2). The unique electronic signal that a single intersection generates is a result of changes in the oxidation state within the TiO_2 layer.[29] Chua predicted that the current-voltage (*I-V*) behaviour of a memristor when sweeping through a potential window a bow-tie like response would be generated; when the sweep would be stopped the charge on the memristor would be retained, similar to a capacitor and thereby accessed at a later period of time.[37] With the current technology used to process a single junction to ~5 nm (through electron beam lithography) within a crossbar array and the ability to stack these devices on top of each other, the creation of an extremely dense device is possible surpassing existing device densities by several orders.[42] The current density ~4 x 10^3 $A \cdot cm^{-2}$ from a single junction is considerably larger for a device with dimensions in the nm regime.

Prior to the reports of the memristor by the HP research group, in 2007 McCreery's research group [43] reported on similar materials regarding the behaviour of molecular heterojunctions containing nm thick molecular layers combined with a TiO_2 layer. TiO_2 is not the only metal oxide to produce bistable responses; there have been previous

reports of metal oxides (binary and ternary) proposed as possible DRAM devices.[44-49] Other materials that display the characteristic bow-tie response may yet be defined as a memristor.[44-49] These materials are is still in their infancy and requires thorough study to understand the mechanism by which metal oxide memristors operate. With the current research being conducted, integration of memristors into future technology shows great promise.

1.1.4.3 Organic Films

The need to diverge from conventional inorganic materials has brought forth uniquely designed organic compounds as possible substitutes for electronic applications. Organic materials present attractive alternatives due to the abundant availability of chemicals and compounds which are straightforward to modify and process.[50] Unlike conventional inorganic semiconductors which are limited by interfacial processes (scale as a function of electrode area), organic materials are able to exhibit molecular or bulk property changes (scale as a function of electrode distance) thereby presenting better scaling properties. Most of the research utilizing organic materials has been centred around materials that are analogous to inorganic semiconductors and their use in common architectures such as transistors,[51] p-n junctions,[52] and light emitting diodes (LED's).[53]

Recent advances within digital memory using organic materials have gained considerable attention, specifically for non volatile memory, since there are few reports regarding volatile memories. In recent years a significant amount of research has been geared towards developing purely organic devices capable of electrical switching,[54] with only a few examples of non-volatile memory reported using conducting polymers [55, 56] and their composites (which incorporate nanoparticles).[34, 57-59] The memory effect that many of these organic materials display is typically due to the charge storage which includes charge trapping, separation, and transfer as the active mechanisms.[60-62] The common electrode architecture utilized is a thin film of organic material amid two ohmic contacts, but there have also been reports of three electrode architectures,[63] multiple layers [64] and a combination with different material systems such as chalcogenides.[65] A considerable amount of research is being conducted using organic materials although a great deal more is required for the design and development of organic digital volatile memory. The Organic Electronics Association's (OE-A) White Paper "OE-A Roadmap for Organic and Printed Electronics" currently does not recognize the potential of organic materials for volatile RAM applications.[66, 67]

Several devices have already come out onto the market utilizing organics for read only memories (ROM) or write once read many (WORM) memories.[68, 69] In 2006, a Swedish company, Thin Film Electronics, announced the development of a non-volatile random access memory (NV-RAM) by printed circuitry techniques.[70] These NV-RAM devices have gradually entered the market because of their low power consumption and ability to cycle more than one million times without degradation, enabling them to last a

minimum of ten years.[54] With a continual influx of organic electronic materials aimed towards the consumer market, society will eventually recognize the potential that these materials have for a multitude of applications.

The work embodied in this thesis deals with a conjugated doped polymer of polypyrrole (PPy) electrochemically modified on gold (Au) electrodes to contain both immobile anions of dodecylbenzenesulfonate (DBS^-) and mobile cations of lithium (Li^+). The system is able to exhibit novel time and potential dependent conductivity based on Li^+ mobility, which can be utilized to create a dynamic memory device.[28, 71]

1.2 Introduction to Conducting Polymers

For a considerable period of time, the scientific community understood polymers solely as common insulating materials; consideration of polymers with a greater purpose was not explored in any depth. During the 1970`s, a collaboration began with three scientists, Hideki Shirakawa, Alan J. Heeger and Alan G. MacDiarmid, which led to the remarkable discovery of an oxidized polymer with extremely high conductivity. The chemical modification of crystalline polyacetylene through the insertion of p-type dopants of halogens, such as chlorine, bromine, and, most notably, iodine, which lead to a conductivity most akin to metallic materials.[72] A new era of research began based on developing doped conjugated polymer systems due to this initial collaboration. The outstanding impact of the discovery was acknowledged by the scientific community in

the year 2000 when the Nobel Prize was given to the three collaborators "for the discovery and development of electroactive polymers."[73, 74] However, prior to their discovery, in 1862 Henry Letheby first reported the synthesis of polyaniline under anodic conditions, which was simply abandoned due to the incompatibility with many other systems.[73, 74]

1.2.1 History of Polypyrrole

With the numerous discoveries of uniquely designed conjugated/conducting polymers known to date, polypyrrole is one of those polymers extensively researched. Since the initial findings in 1963 of the first known synthesis of iodine doped polypyrrole,[75-77] the research within the field of conducting polymers continues to yield a variety of polypyrrole systems. The multitude of research conducted with polypyrrole can be attributed to the chemical and thermal stability, a thorough understanding of the chemical [78] and electrochemical synthesis,[79] and the range of conductivities that can be produced from various polypyrrole derivatives.[80]

Conjugated polymer systems are commonly synthesized by the oxidation of a monomer, either through electropolymerization on a conductive substrate by applying an external potential or through the use of a chemical oxidant present in solution to induce polymerization. Different processing techniques typically yield varying forms, as electrochemical procedures produce films of uniform thickness, where the chemical

route can lead to colloids and aggregates or films.[74] Electrochemical procedures are often used when creating polypyrrole films, as the thickness and morphology can be controlled by monitoring the charge passed.[81] A general technique for the electrochemical deposition of polypyrrole is the application of anodic conditions to a conducting substrate which can oxidize pyrrole in the presence of an electrolytic medium.[78] When the polymer chain reaches a critical length, the solubility limit is exceeded resulting in polymer precipitation onto an electrode surface.[74] Alternative methods by which conducting polymers can be synthesized, such as photochemical initiation [82] and enzyme catalyzed reactions [83] are generally less pursued for research purposes but are none the less interesting and unique ways for processing polypyrrole.

1.2.2 Structure and Properties of Polypyrrole

Research aimed toward the design and development of polypyrrole began well before there was a thorough understanding of the mechanism by which the polymerization of pyrrole occurs.[84] There are currently several mechanisms proposed that have presented strong arguments, although the mechanism proposed by Diaz et al. is the most widely accepted.[79, 85-87] Theoretical studies have confirmed correlations based on the reactivity of unpaired electron density to the radical cations.[88,89] Also through spectroelectrochemical studies, the radical ion (polaron) coupling that occurs is shown to follow the Diaz mechanism.[85]

Pyrrole polymerization begins with an initiation step, where the oxidation of a pyrrole monomer gives rise to a radical cation. These radical cations can then couple to other radical cations to generate a bipyrrole complex. Similar to the monomer, bipyrrole can readily oxidize and couple to other radical cations of monomers, oligomers, or polymeric chains.[90] Termination of the reaction simply proceeds via nucleophilic attack of water molecules or impurities that can occur within the polymer chain (Scheme 1).[85]

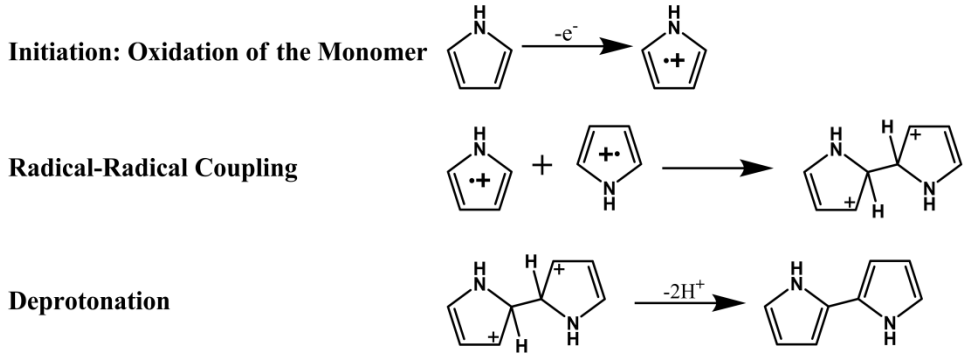

Scheme 1: Pyrrole polymerization mechanism.

The synthesis of oxidized conducting polypyrrole does not result in a neutral polymer, but rather leads to a charged state where every three to four pyrrole units are positively charged (Scheme 2). These positive charges must be charge balanced during oxidation by the addition of anions (dopants) which are interstitially incorporated within the polypyrrole chains.[91] When small mobile anions are incorporated during oxidation, the polymer (P^+) can be reduced resulting in the dopant anion (A^-) diffusing back into an electrolyte solution ($A^- + C^+$), and thus creating a neutral undoped polymer (P^0) (Equation 1.1).[81]

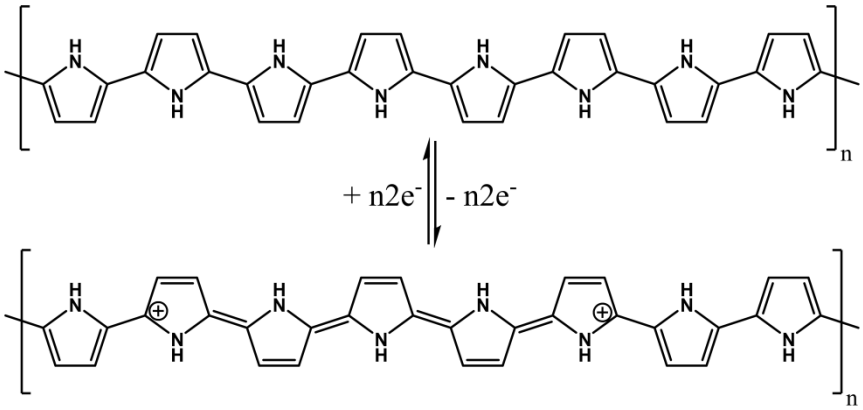

Scheme 2: Interconversion of polypyrrole from the neutral to oxidized form.

$$P^{+}(A^{-}) + C^{+} + e^{-} \leftrightarrow P^{0} + A^{-} + C^{+} \quad (1.1)$$

$$P^{+}(A^{-}) + C^{+} + e^{-} \leftrightarrow P^{0}\,(A^{-}C^{+}) \quad (1.2)$$

In contrast, when large anions (A^{-}) become entrapped within the polymer film (P^{+}) during oxidation, a charge balancing cation (C^{+}) is required upon reduction to stabilize the anion ($A^{-}C^{+}$) thereby neutralizing the charge of the polymer (P^{0}) (Equation 1.2). There are several reports indicating that the doping level in polypyrrole can significantly alter the band structure resulting in a considerable molecular mass change upon reduction.[92-97] The incorporation of dopants within polypyrrole can direct a degree of structural order thereby affecting the conductivity of the polymer.[91] Dopants which exhibit planar geometry can be used to direct polymer chains resulting in anisotropy within polymer films, while non planar dopants can direct the system towards an isotropic nature.[98, 99] Anisotropy can also be induced by decreasing the polymerization temperature, applying high anodic potentials, or creating high dopant to monomer

molar ratios within the electrolyte solution.[99] The structural properties of a polymer film can in turn affect the conductivity of the devised polymer system.[100]

1.2.3 Intrinsically Doped Polypyrrole

The doping process involved within conducting polymers is quite different from its counterpart of Si. Conventional semiconductors like crystalline Si can be doped with either donor or acceptor atoms to incorporate electrons and holes within the band gap. N-type semiconductors commonly consist of Group IV elements doped with elements from Group V, which act as electron donors to increase the Fermi level towards the conduction band (CB). The majority of the electrical conductivity is attributed to the CB and thus the electrons are the main charge carriers for the system. In contrast, p-type semiconductors are typically a combination of Group IV elements with Group III as the dopants, which in this case act as electron acceptors to lower the Fermi level towards the valence band (VB) and the electrical conductivity of the system is derived from holes.[1, 3, 101] The doping effects based on inorganic semiconductors do not alter the band structure or the density of states.[73]

Conjugated polymer systems have been reported to incorporate up to 33 wt% of either donor or acceptor type dopants.[102-104] By applying either anodic or cathodic potentials to an electrode, polymers can be doped to form p- or n-type semiconductors. Surfactant molecules are considered to be suitable dopants since they can be

incorporated into a conjugated polymer system such as polypyrrole. [105-108] Surfactant like dopants are known to form discrete arrangements of micelles in solution which can in turn direct the polymerization.[109] The anion DBS^- has been reported to be incorporated within a polypyrrole film due to the amphiphilic nature of the molecule which contains both a hydrophilic head and hydrophobic tail. A significant amount of work has been conducted by Smela et al.[81, 110-113] towards the understanding of ion mobility occurring within polypyrrole doped DBS^- systems. Smela et al. have reported the reduction-oxidation (REDOX) reaction of $PPy(DBS^-)$ in a solution of lithium perchlorate ($LiClO_4$) where the lithium ion (Li^+) is able to diffuse in and out of the film to either charge balance DBS^- or return the polymer back to its oxidized state as per Equation 1.2.

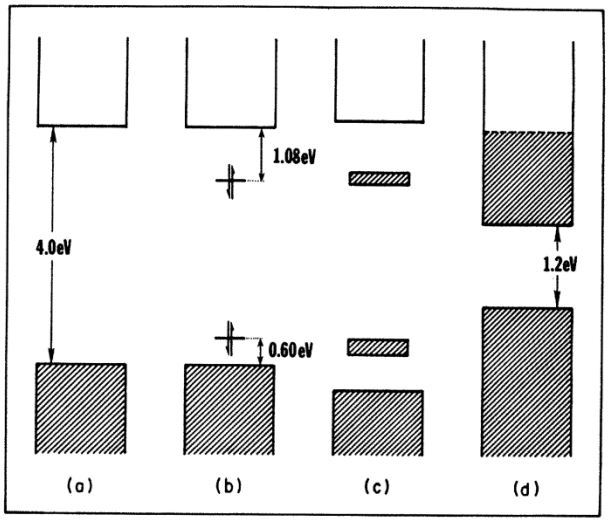

Figure 5: Valence effective Hamiltonian calculations [102-104] of the band structure of polypyrrole upon sodium doping - a) The band gap of pure, undoped polypyrrole **b)** The more stable bipolaron appears in the band gap above the valence band and below the conduction band **c)** Further doping up to 33-mol % results in bipolaron bands **d)** A hypothetical doping level of 100-mol %. [102-104] (Reprinted figure with permission from

Bredas, J. L.; Scott, J. C.; Yakushi, K.; Street, G. B., Polarons and Bipolarons in Polypyrrole - Evolution of the Band-Structure and Optical-Spectrum Upon Doping. *Physical Review B*, *30* (2), 1023-1025, 1984. Copyright 1984 by the American Physical Society)

Understanding polymer morphology can be useful when determining parameters such as conductivity. Specifically, polypyrrole's morphology has been probed using in-situ atomic force microscopy (AFM) and scanning tunnelling microscopy (STM). Using an atomically smooth surface of highly oriented pyrolytic graphite (HOPG), the oxidative polymerization of polypyrrole on the surface of HOPG has been analyzed.[114] Upon reduction, depending on the size of the dopant, it was determined that there were only minute changes within the films morphology. Therefore the main factor for determining polymer structure was due to the oxidative polymerization process.

1.2.4 Design Strategy for a Hybrid of Polypyrrole

Conducting polymers have enabled a number of new innovative material systems that can be defined by their heterogeneity and dynamic properties. A substantial amount of research has been directed toward developing conducting polymers for the integration into electronics,[115] in effect to replace their inorganic counterparts. With the discovery of polyacetylene and the ability to tune the conductivity based on chemical modification, the main focus of many researchers has been aimed at tuning band gaps by altering the structure [102-104] or carrier type (either p- or n-type).[116] A focus of polymer research has been devoted to understanding and controlling the interstitial

ionic charge carriers that can become immobilized within a conjugated polymer.[117] Polypyrrole which is a common conjugated polymer combined with a surfactant molecule of DBS^- and Li^+ was utilized within this study although it was first reported in 2008 by Freund and Thomson et al.[28] Polypyrrole is initially oxidized in the presence of a large bulky anion DBS^-, which becomes entrapped within the polymer film and, furthermore, upon reduction in an electrolyte solution containing metal cations (M^+), is able to incorporate M^+ into the polymer backbone to charge balance the DBS^- (Scheme 3).

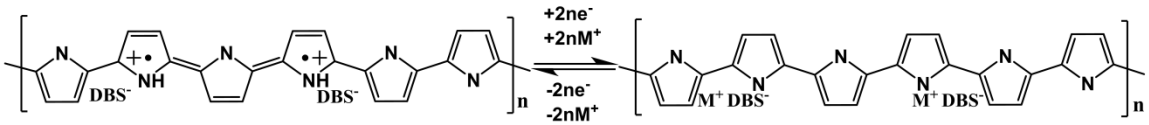

Scheme 3: Polymer hybrid mechanism

1.2.4.1 Proposed Model of PPy(Li^+DBS^-)

Ion mobility is commonly seen within electrolyte systems of polymers, such as polymer electrolytes or proton exchange membranes (PEMs). A very common PEM, known as Nafion has been around since the 1960's and is the main constituent upon which fuel cells are based.[118] In the mid 1980's, polypyrrole was shown to be a good dynamic ion conducting membrane [119] and the work done by Smela et al. defined physical and optical measurements for ion mobility within an electrolyte media using PPy(DBS^-).[113]

The strategy employed to create the polymer hybrid of PPy(Li^+DBS^-) utilized within this thesis was intended for use in the solid/dry state (free of electrolyte) where Li^+ can charge balance the DBS^- contained within the polymer matrix of polypyrrole. A similar description of the system was reported by Krieger et al. in 2001 where the application of an external field would cause inter-phase ionic motion within their designed polymer system.[120] The unique electronic properties of the polymer hybrid of PPy(Li^+DBS^-) can be seen in a two electrode setup where an induced field can overcome the ionic bonding of Li^+ with DBS^- thereby causing the Li^+ to become mobile within the polymer.

The three different schematics in Figure 6 are the proposed mechanisms of charge transport for the polymer hybrid of PPy(Li^+DBS^-). Initially (Figure 6a) when there is no electric field applied to the system, charge balancing ions are distributed throughout the polymer spanning a distance *(L)* between a set of contacting gold (Au) electrodes. The large immobile anions of DBS^- (*indicated in red*) are entrapped within the polymer and charge balanced by Li^+ (*indicated in blue*) inserted during the reduction process. The application of a low or medium field, results in the field dropping between the two electrodes where the conduction current is either due to an ohmic or space-charge-limited current (SCLC) (discussed in detail within Chapter 3 - 3.1.2 and 3.13). The main contributor for the conduction current is due to the injection of positive carriers (holes) (*indicated in white*) into the polymer hybrid material (Figure 6b). Once there is an applied field large enough to overcome the ionic pairing (Figure 6c), the induced motion of Li^+ can result in the cationic redistribution throughout the film (discussed in detail

within Chapter 3 - 3.1.4). The field induced movement of Li^+ away from the anode leaves behind the DBS^- stabilizing the injection of positive charge carriers thereby creating a conduction region (L_x), effectively reducing the distance between contacts from *L* to *L'*.

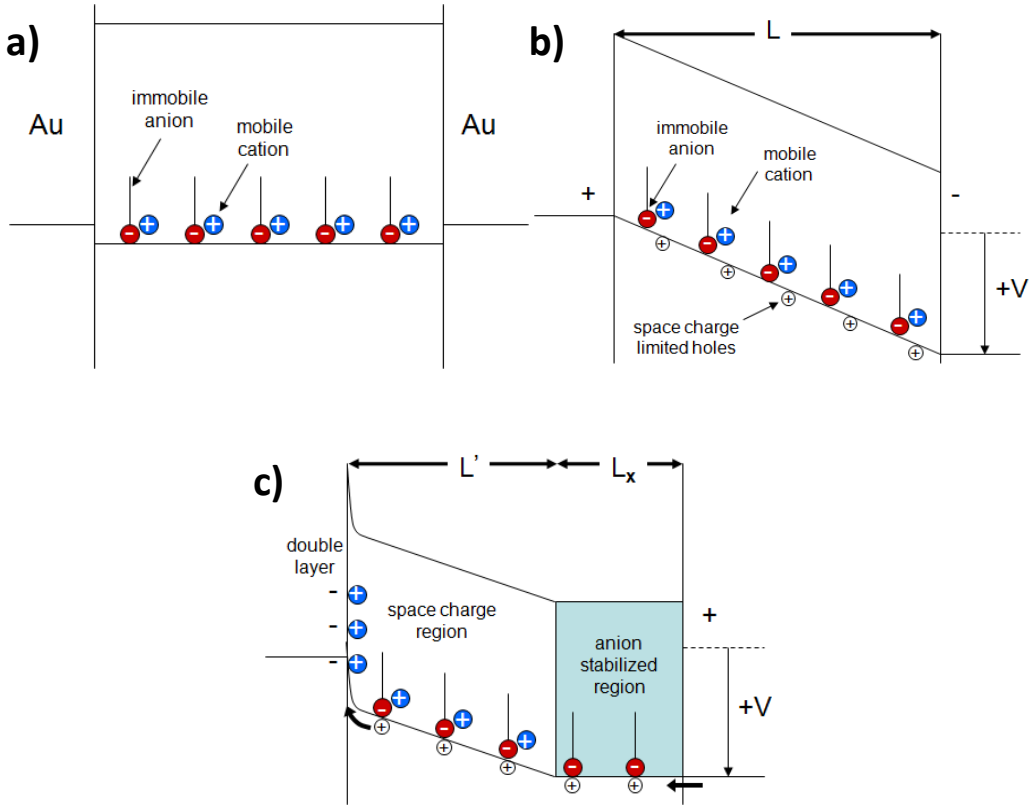

Figure 6: Proposed conduction model of field generation carrier current.[28]

Due to the unique property of field induced ionic motion of Li^+ within the polymer hybrid of $PPy(Li^+DBS^-)$, the system is able to exhibit novel potential and time dependent conductivity. With the overall goal of integrating $PPy(Li^+DBS^-)$ into DRAM devices it is

important to quantify the scaling factors that occur within this system. Since there are only a handful of reports based on conducting polymers that possess characteristic time dependent behaviour useful for memory applications, understanding the scaling properties of PPy(Li^+DBS^-) can potentially be useful for similar systems.[54-56, 58, 59, 63, 120-122]

Chapter 2 Experimental Approach

2.1 Design and Fabrication of a Test Device

The polymer hybrid system PPy(Li^+DBS^-) discussed within this work has been previously studied with dimensions in the micrometer (μm) [28] and nanometre (nm) range.[71] However a systematic investigation of the scaling properties has yet to be performed. Previous devices had complex 3-dimensional (3-D) designs making it difficult to understand the scaling properties of the fields and associated current. A structurally simple design with only one dimension to be altered, was designed and fabricated for the systematic investigation of PPy(Li^+DBS^-).

2.1.1 Proof of Concept Devices

Previously, devices utilized for the study of PPy(Li^+DBS^-) were an interdigitated array (IDA) (Figure 7) and a crossbar array (Figure 8). The gold (Au) IDA electrodes were obtained from the Biomedical Microsensors Laboratory at North Carolina State University (Figure 7a). The IDA was composed of a set of alternating Au bars spaced 20 μm apart, 2.8 mm long and 0.075 mm wide. The total exposed area for polymer deposition on an IDA was 6.09 mm^2 (Figure 7b). Polymer was grown on both electrodes to a total amount of charge per unit area of 1.23 $C \cdot cm^{-2}$ resulting in a thickness of 6 μm, which was enough to completly bridge the 20 μm spacing (Figure 7c).[28]

The other configuration chosen was a crossbar array which has been utilized by many reasearchers to create high density devices with good scalability.[123, 124] The 10 x 10 crossbar array was fabricated to consist of 20 µm wide Au electrodes perpendicularly crossed with a ~500 nm dielectric spacer of SiO_2 (Figure 8a). Polymer was then grown from the bottom electrode and monitored until contact was made to the top electrode where a Au/polymer/Au junction could be made (Figure 8b and c).[71]

Both designs gave similar non-linear current-voltage (*I-V*) behaviour, though the currents were reported to increase by an order of magnitude from the IDA to crossbar array (discussed in detail in Chapter 3 Section 3.1.1).

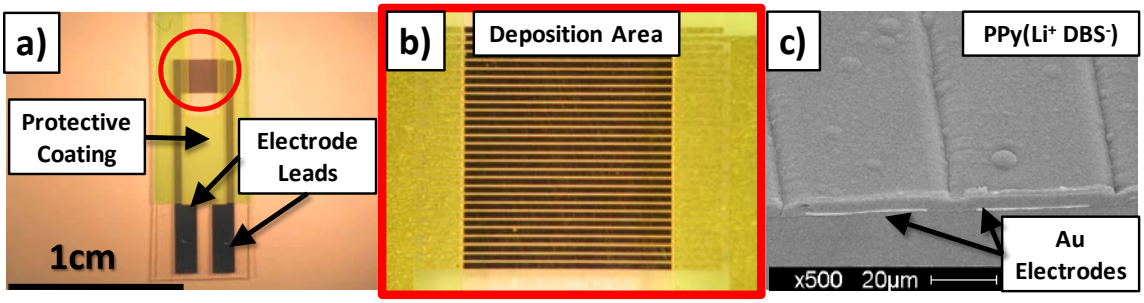

Figure 7: IDA design – a) A single IDA used for the preliminary testing of PPy(Li^+DBS^-). **b)** A close up of the alternating Au lines connected by the electrode leads at the bottom of the IDA. **c)** An SEM image of PPy(Li^+DBS^-) grown on the IDA.

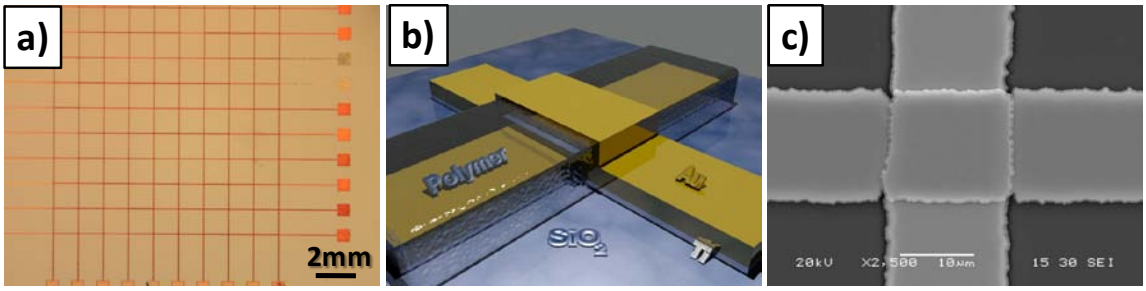

Figure 8: Crossbar design – a) A 10 x 10 crossbar array of intersecting Au lines. **b)** A rendered image of a single crossbar junction on a SiO_2 substrate and separated by a layer of SiO_2. The bottom electrode is initially utilized when growing the polymer until it reaches the top electrode forming the junction. **c)** A SEM image of a single crossbar junction with PPy(Li^+DBS^-) grown onto the Au bars.

2.1.2 Design Schematic

The fixed dimensions of the Au electrodes in the IDA and crossbar array limited their use for the systematic analysis of various polymers in a well defined manner (explained in detail within Chapter 3 Section 3.1.1). Therefore a simple design of a set of parallel bars was chosen as the electrodes for polymer growth, with only one dimension varied while all other dimensions were kept constant. The polymer was grown spanning the two electrodes of variable distances (*L*) of 2, 5, 10, 15, 20, 25, 30, 35, 40, and 45 µm as these dimensions were attainable with the available microfabrication processes. The electrode design was extended to allow contact through a commercially available edge connector to enable quick and simple connections with the fabricated device. The final design feature was to add a contact pad at the end of an electrode which could be used to measure the resistance with a finite contact of a probe station (Section 2.2.4, Figure 9

and Figure 10a); the resistance of the Au bars was determined to be ~10 ohms (Ω) which is minor compared to the deposited polymers.

In order to control the area on which the polymer would be electrochemically deposited, several windows of 500, 250 and 100 µm were designed onto a single mask (Figure 10b). Preliminary testing of polymer deposition revealed that the amount required to bridge the distance between the two electrodes with a window larger than 100 µm would take an extensive period of time, therefore only the 100 µm window was chosen for polymer deposition.

The electrode patterns and windows were designed using L-Edit (Tanner Research), a computer program for designing micro-electro-mechanical systems (MEMS). The designs were then submitted to the University of Alberta nanofabrication facility in Edmonton Alberta to be printed onto 5" soda lime glass squares 0.09" thick for use as masks in the lithographic process of fabrication (Figure 10).

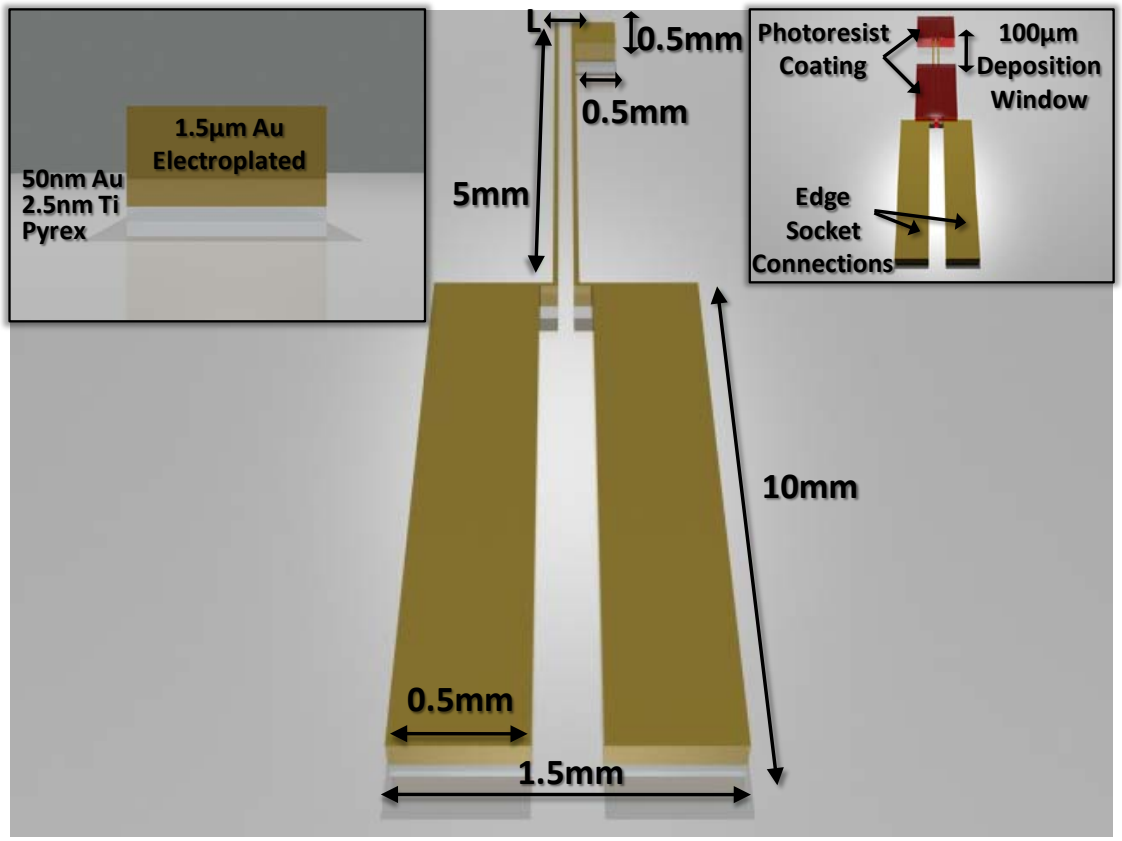

Figure 9: Parallel bar design – The above image depicts all dimensions of a single junction used for the systematic analysis of various polymers where *L* defines the variable distance between a set of electrodes. The left inset shows the different layers of the electrode on a Pyrex substrate with the e-beam evaporated Ti and Au as well as an electroplated Au layer. The right inset shows the designation for each area of the electrode with large contact pads to contact an edge connector and the polymer deposition window defined by the photoresist.

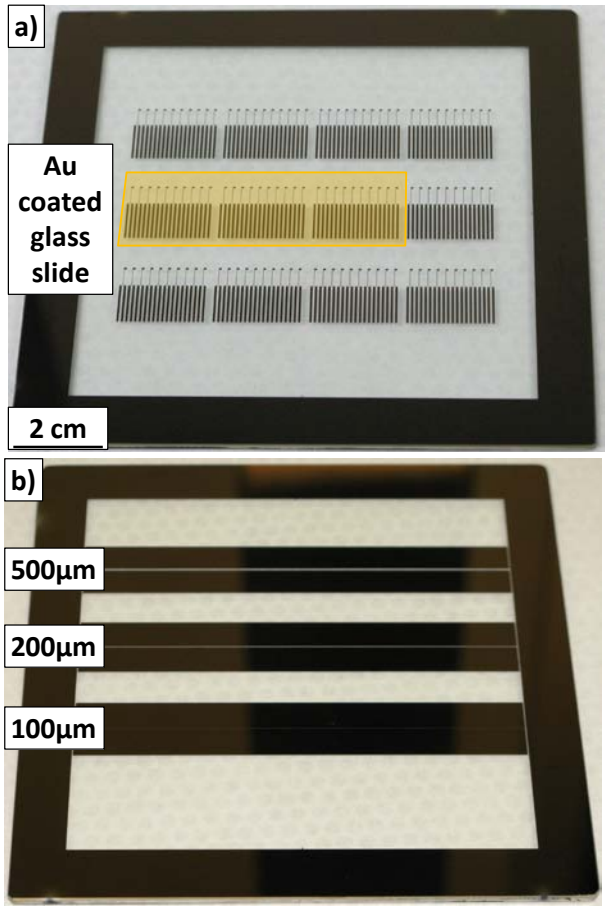

Figure 10: Printed Mask Designs – a) A 3 x 4 array of device patterns printed onto a single mask. The highlighted region shows 3 devices that can be patterned onto a single Au slide. **b)** Three different sized windows used to control the deposition of the polymer.

2.1.2 Device Fabrication

The facilities at the University of Manitoba Nano-Systems Fabrication Laboratory (NSFL) (class 10-100) housed all necessary equipment for fabricating the designed device. An optimized fabrication process for creating the device is discussed in detail within the subsequent sections.

2.1.2.1 Au Plating

Gold coated substrates are commonly used for the electrodeposition of conducting polymers since they do not readily oxidize under deposition conditions and are used as the electrodes within this study. Pyrex slides coated with electron-beam (e-beam) evaporated Au (500 angstroms (Å) thick) over a titanium (Ti) (25 Å thick) adhesion layer were purchased from Platypus technologies. The as-received Au substrates were too smooth resulting in the delamination of polymer from the Au electrodes during processing; therefore an extra layer of Au (1.5 µm thick) was electrochemically deposited onto the commercial slides as per the procedure designed by Smela et al. prior to the lithographic process.[125]

Contamination with other laboratory chemicals frequently interfered with the plating process, resulting in non-uniform films; therefore a thorough cleaning of all plating materials was required. Materials used for the plating process were cleaned in freshly made piranha solution (H_2SO_4:H_2O_2:H_2O=1:2:4 volume ratio), then thoroughly rinsed with deionized (DI) water and, isopropanol and finally stored in DI water until platting. *Acid piranha solutions utilized for removing trace organic residues must be handled with caution as these have the potential to react violently.* Therefore, proper safety precautions must be taken when preparing and especially when disposing of piranha solutions to keep them away from all organics and metals placing into acid only waste. Other materials not compatible with acid piranha cleaning (such as the reference

electrode) were specifically designated only for the plating process to avoid contamination.

A 1:20 mixture (1 troy ounce/500 mL) of a commercial plating solution (Oromerse SO Part B, Technic Inc.) in 1.7 M sodium sulphite (Na_2SO_3) was used for Au deposition. Combining the plating solution with Na_2SO_3 helped sustain the pH so as to prevent $Na_2Au(SO_3)_2$ from decomposing.[126] The optimal plating pH was previously reported to be above 8.9, plating Au at lower pH's would result in non-uniform films.[125] Gold deposition was achieved using a three electrode setup with a CHI-760C Bipotentiostat (CH Instruments) workstation, with an Ag/AgCl reference electrode, a platinum (Pt) foil counter electrode, and the commercial Au coated Pyrex substrate as the working electrode (Figure 11). The electrochemical technique of cyclic voltametry (CV) was utilized, by scanning a potential window of -0.6 to -1.4 V at a rate of 50 $mV \cdot s^{-1}$ (Figure 12a). From the CV of the Au solution (Figure 12b), the current begins to decrease at a potential of -0.7 V determined to be an optimal plating potential. A constant potential of -0.7 V was applied to the working electrode with an area of 16.51 cm^2 until a charge of 21.18 coulombs (C) was reached, yielding a thickness of Au ~1.5 µm (0.8 Ccm^{-2} for every 1 µm determined from profilometry measurements, Section 2.2.5).

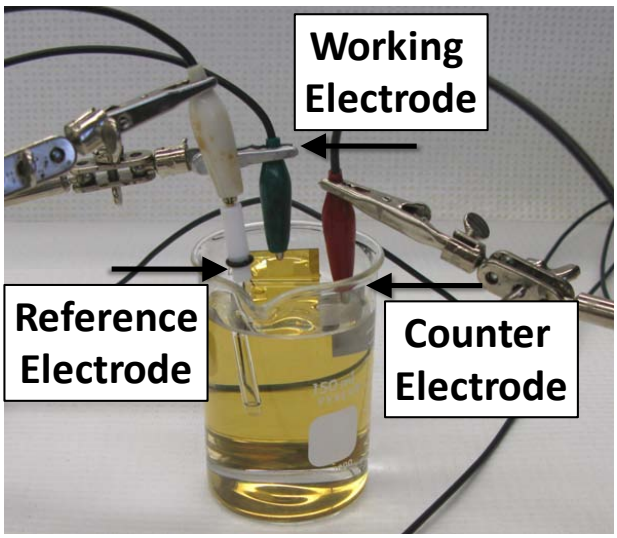

Figure 11: Three electrode setup used for Au deposition – The Ag/AgCl reference electrode (*white lead*), platinum (Pt) foil counter electrode (*red lead*), and commercial Au coated Pyrex substrate as the working electrode (*green lead*) all connected to and controlled by a CH Instruments workstation.

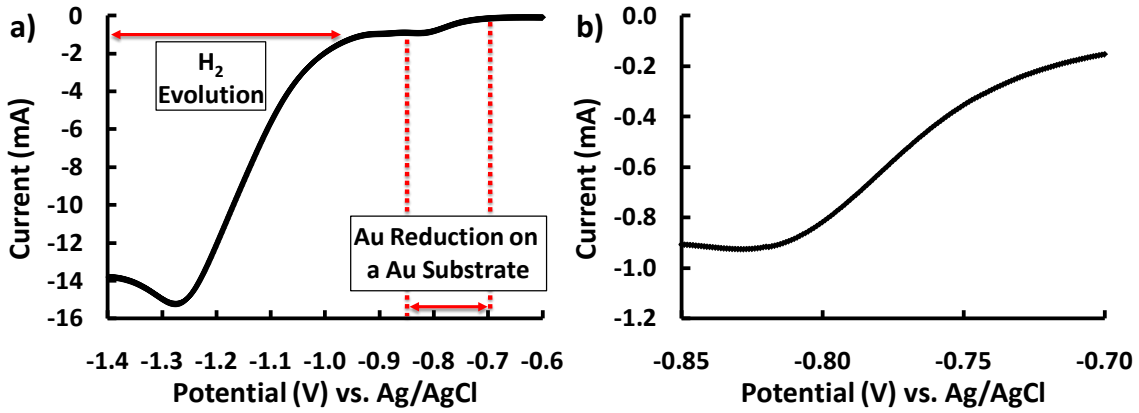

Figure 12: CV of Au in Au plating solution – a) The CV of the commercial Au substrate in a 1:20 plating solution where the optimal plating potential is from ~-0.7 to -0.85 V. Lower potentials less than -0.7 V would typically degrade the Au substrate destroying the primary seed layers of Au and Ti due to H_2 evolution. **b)** A close up of the Au reduction beginning at ~-0.7 and goes to ~-0.85 V which is characteristic of an Au substrate.

More negative potentials less than -0.7 V could be used for less time, but were found to produce non-uniform films due to H_2 evolution, destroying the seed layers of Au and Ti. There are distinct differences between the commercial Au substrates and the electroplated Au as seen with the optical and scanning electron microscope (SEM) images, where the initial surface is shinny and featureless (Figure 13a and c) then becomes lustreless and granular (Figure 13b and d). Once the plating process was complete the samples were thoroughly rinsed with DI water, dried with N_2, and stored in a polypropylene (PP) container.

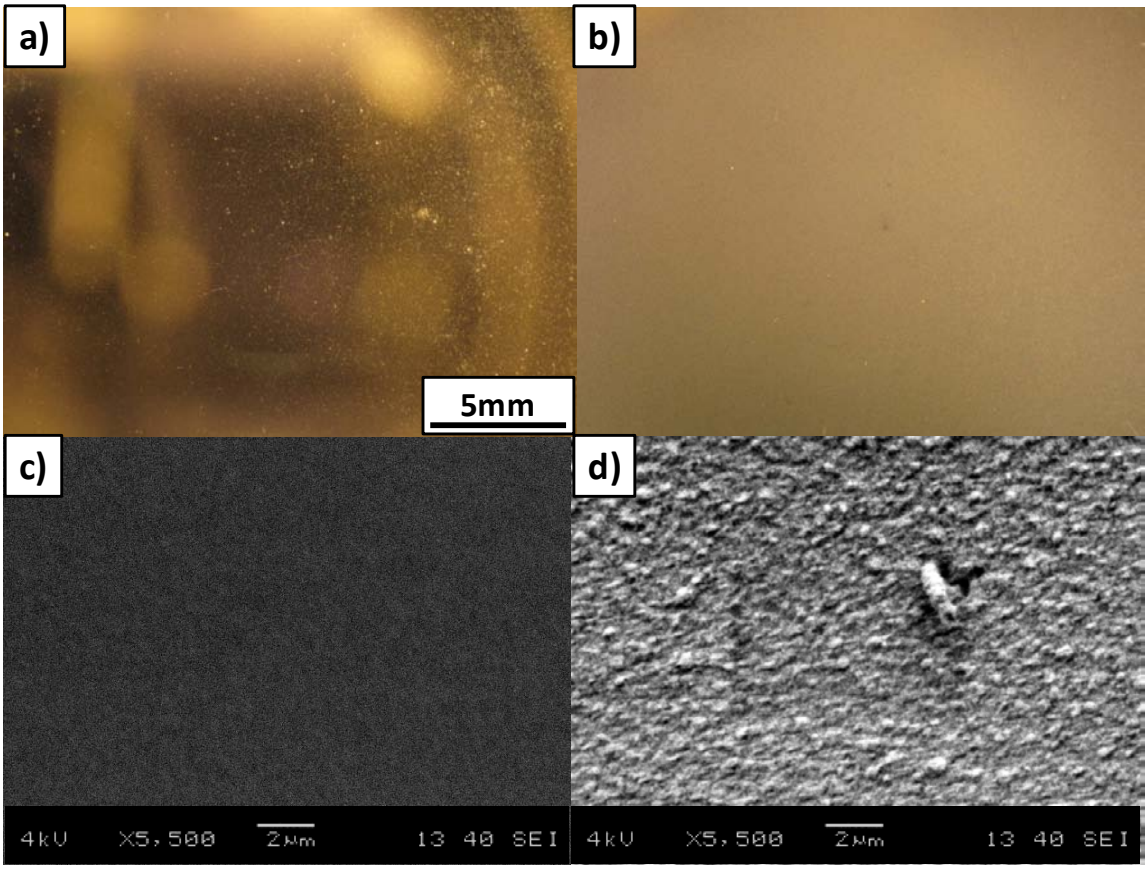

Figure 13: Au plating images – a) An optical micrograph of the commercial Au coated substrate which is quite lustrous. **b)** An optical micrograph of the same substrate with an additional 1.5 µm of Au electroplated on top of the as received Au substrates which has now become dull and lustreless. **c)** The SEM image of the commercial Au coated substrate is seen to be featureless and smooth. **d)** The SEM image of the electroplated Au with many rough features which enhances polymer adhesion onto the Au substrate.

2.1.2.2 Lithography

A simple lithography process was employed for fabricating the structures designed on the printed masks (Figure 10). The operating procedures defined in the NSFL laboratory manuals were strictly followed for all the instruments, although specific parameters were optimized for the fabrication of the device. The general lithography process

(detailed in the following paragraphs) proceeds by first applying a layer of photoresist which must then be soft-baked. The photoresist is then patterned by exposing the substrate to an ultraviolet (UV) source through the designed mask and then developed in a solution to reveal the pattern of the desired structure. A final hard bake is done so that the photoresist patterns are able to withstand the etching process revealing the device structure.

A uniform layer of photoresist was applied to the Au slide by placing the sample onto the Spintech S-102 Coater vacuum chuck. A negative photoresist, Megaposit SPR 3012 (Rohm and Hass Electronic Materials LCC), was evenly applied to the Au slide which can be used to create the smallest design feature of 2 µm. An initial rotation of 500 rotations per minute (rpm) for 5 seconds (s) was used to evenly coat the substrate, then ramped to 3500 rpm and held for 20 s. The selected parameters have been optimized by Rohm and Hass to yield a thickness of 1.4 µm using Megaposit SPR 3012 photoresist, which was also confirmed by profilometery (Section 2.2.5).

After evenly coating the Au sample with photoresist, a soft-bake is required to drive off solvent within the film. The purpose of driving off the solvent is to increase photoresist adhesion onto the substrate thereby preventing defects that may occur throughout the fabrication process.[127] Using a HPO-200 vacuum soft-bake oven at a temperature of 110^0C, the photoresist was evenly soft-baked. The process was completely automated once the coated Au slides were placed onto the loading tray of the soft-bake oven. The settings chosen for an initial proximity timer (to control how much time the substrate

will lay close to, but not touching the hot plate) was 5 s and the contact timer (which controls the actual contact of the substrate with the hot plate) set for 100 s. Once the soft-bake process was complete the samples were cooled for at least 15 minutes (min) before further processing.

After the soft-bake process, the pattern of the device was transferred from the mask (Figure 10a) onto the sample using the mask alignment system (ABM Inc.). The substrate was placed onto the vacuum stage and the available patterns were aligned onto the substrate using the microscope aligner. Once all the dimensions were properly set, the respective contacts were made. The sample was then exposed to a UV source with a maximum intensity of 40 $mW \cdot cm^{-2}$ at 400 nm. The exposure light is a broad set of wavelengths (365 to 435 nm) and the exposure time has been calibrated for all available photoresists in the NSFL. The best exposure time for Megaposit SPR 3012 photoresist with a thickness of 1.4 μm was empirically found to be 15 s. After the photoresist exposure, the newly imprinted pattern was then developed.

A beaker containing Microposit MF-701 Developer (Rohm and Hass) was used to expose the pattern for the designed device. Using a pair of PP tweezers, the glass slide was gently agitated in the developer solution to remove the photoresist from unwanted areas for ~1 min and then rinsed with DI water. The sample was thoroughly dried with N_2 and then placed in a hard-bake oven at 120^0C for approximately 20 min, completing the lithographic process.

2.1.2.3 Wet Etching

Once the samples have cooled off following the lithographic process, the selective etching process can begin. A premade Au etching solution of 1 g $I_{2(S)}$ + 4 g $KI_{(s)}$ + 40 mL DI water was used to etch away both the electroplated and e-beam deposited Au. The sample was placed into a glass beaker containing the Au etching solution and agitated for about ~6 min. After 4 min, the samples need to be continually checked so as to reveal the smallest feature of 2/5 μm without over-etching any of the patterns, thereby completely destroying the device structure.

The next etching process uses a buffered oxide etch (BOE) (a combination of ammonium fluoride (NH_4F), hydrogen fluoride (HF), and DI water) to remove the Ti adhesion layer. *Buffered oxide etch is an extremely hazardous solution and all precautionary measures must be taken from dressing in the appropriate chemical attire to proper rinsing and disposal procedures that are assigned for the specific laboratory.* Samples and equipment that have been used with the BOE process must be thoroughly rinsed with DI water at least five times. Similar to the Au etching process, etching times can vary using BOE, however complete etching of Ti takes ~5 min. Since the Ti layer is simply an adhesion layer for Au onto the Pyrex substrate, it is very thin and transparent, making it difficult to determine when Ti is completely removed; therefore both an Olympus BX51 microscope and multimeter (to measure the resistance) were used to ensure that the etching process was complete.

2.1.2.4 Device Preparation

After the Au parallel bars were patterned onto the glass substrate, the Pyrex slide was cut so that individual pieces can fit into the edge connector (Figure 14). The remaining photoresist on the patterned design was removed using acetone and another layer of photoresist was coated on top of the entire substrate in order to protect the sample from debris while making the required cuts. The cutting procedure requires a water cooled resinoid blade which contaminates the sample surface and can lead to problems during polymer deposition. The device was cut to a height of 2 centimetres (cm) and length of 2 cm allowing precise electrical contacts into a commercial edge connector (Digi-Key) containing 20 Au contacts with a 1 mm pitch (Figure 14). The commercial edge connector was soldered to a custom printed circuit board (Digi-Key) connected to pushpin connectors (Digi-Key) for the sole purpose of making simple leads from the fabricated device to the CH Instrument workstation.

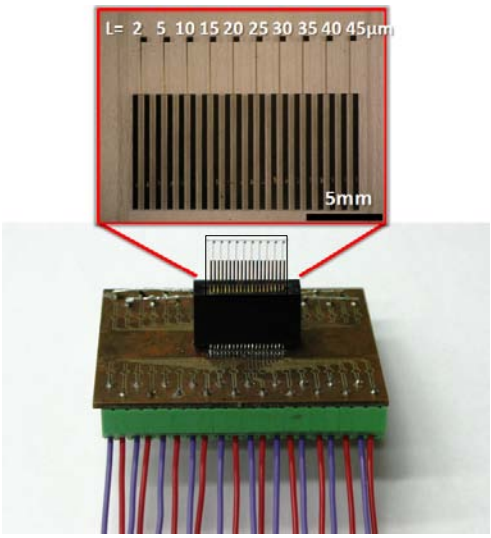

Figure 14: Edge connector socket – A custom printed board connected to an edge connector socket where each lead is connected to a single push pin connector. The push pin connector allows for simple contacts to the patterned device. The zoomed image shows a single patterned device without a photoresist controlled window showing the length of each spacing *(L)*.

The wafer saw (Diamond Touch Technologies Inc.) in the NSFL was used to make the precise cuts. The sample was vacuum seated onto the stage and aligned for cutting using a resinoid blade designed for Pyrex and glass substrates. The system was set to an air pressure of 85 pounds per square inch (psi) and a water flow of 20 gallons per hour (GPH) to cool the blade rotating at 12000 rpm. The sample was then cut partially through using a height of 0.3 mm above the surface of the stage at a rate of 1.5 $mm \cdot s^{-1}$. The entire sample was then separated into the individual pieces, rinsed with DI water and dried with N_2.

2.1.2.5 Control Windows

After the device was cut into the desired dimensions, the protective photoresist was removed using acetone and isopropanol then rinsed with DI water. The sample was first dried using N_2 and then allowed to further dry while rotating on the Spintech S-102 Coater. The sample was then coated with 7 drops of Megaposit SPR-3012 photoresist and spun using the same settings previously mentioned in Section 2.1.2.2. The same lithographic process for creating the Au electrodes (Section 2.1.2.2) was followed with the exception that the 100 μm window mask (Figure 10b) was used to expose a deposition area for the polymer. Once the final hard-bake process was complete, devices were immediately brought to the electrochemistry lab and the proceeding polymer deposition was conducted.

2.2 Experimental Procedure and Instruments

2.2.1 Materials and Reagents

Pyrrole (98% reagent grade), dodecylbenzenesulfonic acid sodium salt (NaDBS) (technical grade), and lithium perchlorate ($LiClO_4$) (ACS reagent≥95%) were purchased from Sigma-Aldrich Chemical. The as-received NaDBS (technical grade) is not simply a linear 12-carbon alkyl chain attached to a benzene ring but contains several isomers with chain lengths ranging from 10 to 13 carbons, previously determined by Smela et al. and any effect of these isomers has yet to be reported.[81] The pyrrole monomer was

distilled upon arrival and kept at -30^{0}C or lower to prevent oxidation. Pyrrole films were grown on the fabricated electrodes using an aqueous solution of 0.1 M pyrrole monomer (brought to room temperature) and 0.1 M electrolyte of NaDBS. Deionized water was chosen as the solvent since it readily dissolves NaDBS but does not dissolve the protective window of photoresist patterned onto the device. The photoresist can easily be removed by organic solvents since they are polymers designed for lithographic processes. Silicon dioxide was not chosen as the protective window due to poor coverage along the edges of the electrode which would result in uncontrolled polymer growth. The PPy(DBS^-) films were then reduced in 1.0 M $LiClO_4$ to incorporate enough Li^+ into the polymer to charge balance the DBS^-.

2.2.2 Electrochemical Synthesis of Polypyrrole and Associated Derivatives

All electrochemical experiments were conducted using a CH Instrument CHI-760C Bipotentistat workstation connected and controlled through a desktop/laptop personal computer. Deposition proceeded via a three-electrode setup, where the fabricated device, fully inserted into the edge connector socket (Figure 14) with all leads connected to each of the Au bars, operating as the working electrode. Other connections included within the setup were a Pt wire which functions as the counter electrode, and an Ag/AgCl electrode as the reference. The three-electrode setup was placed over a water

bath at a constant temperature of 20^0C (Figure 15) to maintain uniform deposition of the polymer films.

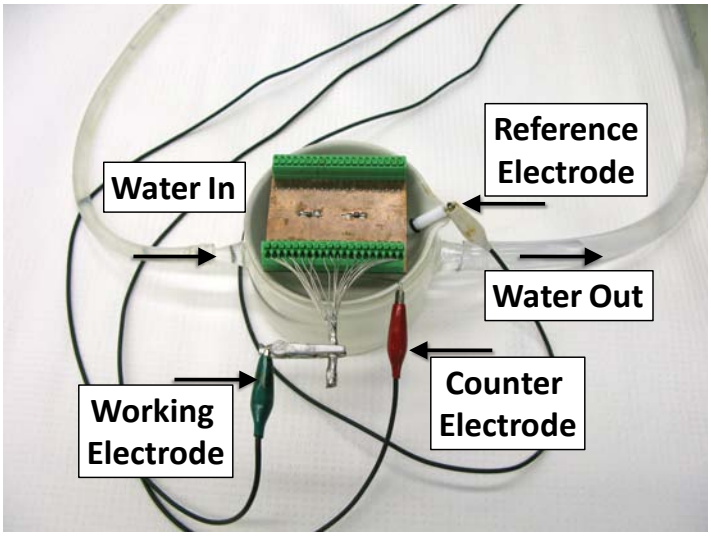

Figure 15: Electrochemical setup for polymer deposition and reduction – The entire electrochemical setup was placed over a water bath to maintain a constant temperature. All leads of the working electrode (*green lead*) were connected through the socket and only the area that was to be deposited on was placed into solution. The Ag/AgCl reference electrode (*white lead*) and Pt counter electrode (*red lead*) were placed into solution making sure not to contact the other leads. All leads of the setup were connected and controlled by the CH Instrument workstation.

2.2.2.1 Optimized Conditions for Oxidative Polymerization of PPy(DBS^-)

All three electrodes were placed into a solution containing 0.1 M pyrrole monomer and 0.1 M NaDBS. The CV was scanned from 0 to 0.7 V at a rate of 50 $mV \cdot s^{-1}$ to determine the optimal growth of PPy(DBS^-) which proceeds via constant current deposition of ~1.0 microamp (µA) (Figure 16). While constant potential or potentiodynamic deposition could be used, they were found to produce films that grew at irregular rates based on

the measured height:width ratios. A certain amount of charge was passed which was determined from a calibration done by Smela et al., relating charge per unit area to thickness.[81] For a film to be grown 25 µm thick, based on Smela's calibration, a charge of 6.135 x 10^{-3} C was required, calculated for a presumed area of 1.227 x 10^{-3} cm^2. A constant current of 1 µA for a period of 6135 s was enough to sufficiently bridge the spacings from 2 to 45 µm and compensate for the overgrowth onto the insulating layer of photoresist (Figure 17).

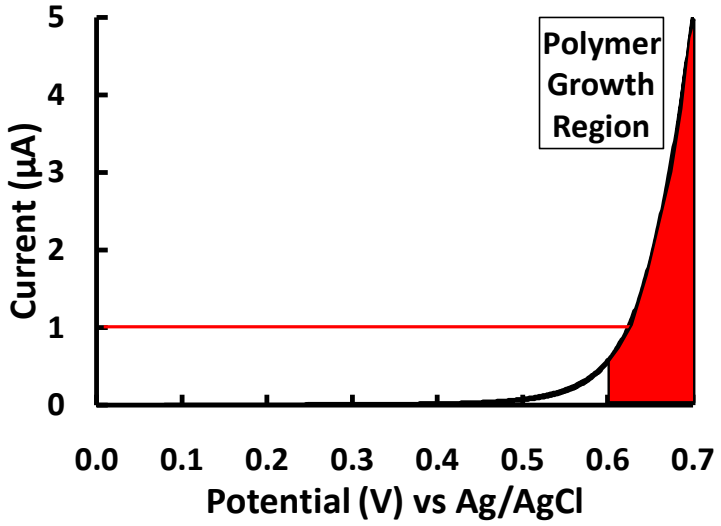

Figure 16: CV of 0.1 M pyrrole and 0.1 M NaDBS – A potential from 0 to 0.7 V was scanned at a rate of 50 $mV \cdot s^{-1}$ to measure the associated current. The red area signifies an optimal deposition potential and the red line indicates the optimal current used for deposition which lies within the red region.

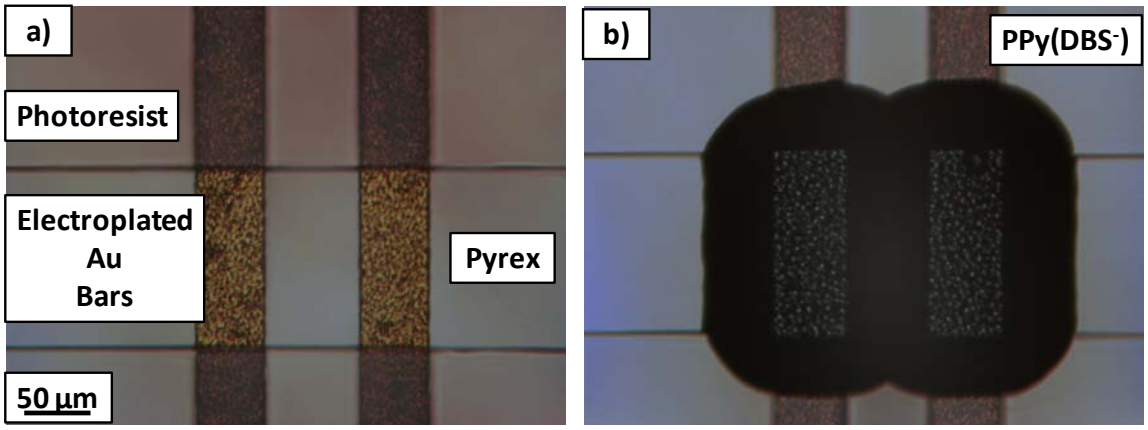

Figure 17: Optical Micrograph of a 45 µm Gap Spacing – The probe station was used to obtain optical micrographs of **a)** a 100 µm control window of photoresist covering a set of 50 µm electroplated Au bars and **b)** ~20 µm thick PPy(DBS^-) deposited onto Au bars with slight overlap onto the photoresist layer.

The thickness of the polymer was then measured with profilometry (Section 2.2.5), and determined to be ~20 µm thick (Figure 18). The axes in the plots are not symmetric, as the width has been expanded by almost an order of magnitude more than the height. The ratio of width to height growth rate is about 2 to 1, which assumes a non-uniform growth unlike Smela's work where the polymer growth (on a homogeneous electrode surface) is quite uniform. To understand the growth properties of PPy(DBS^-), the profiles were measured from various calculated thickness following Smela's calibration (Figure 19). The calculated and measured thicknesses deviate due to the polymer growth (> 1 µm) quickly depositing over the layer of photoresist which contribute to the total area of the deposited polymer.

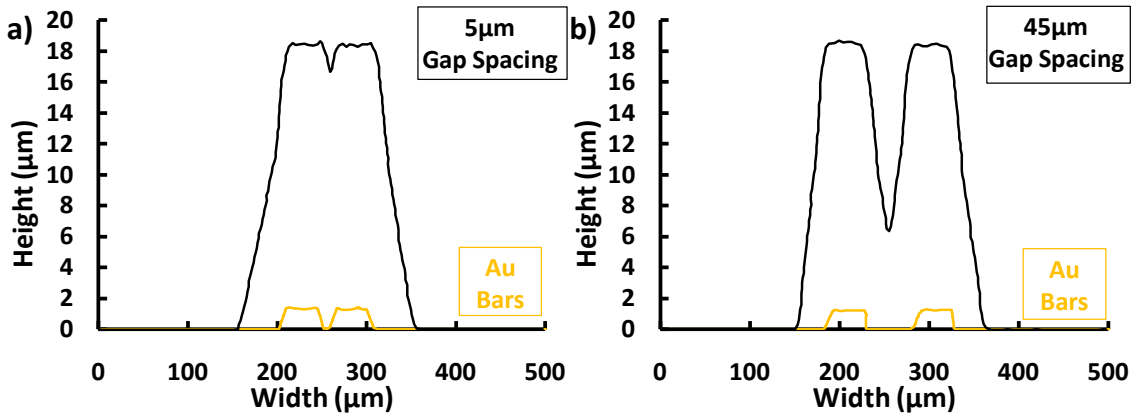

Figure 18: Profile of PPy(Li^+DBS^-) deposited on Au parallel bars – Both the **a)** 5 µm and **b)** 45 µm polymer profiles can be seen to show similar growth at a rate of 2:1 horizontal to vertical which can be compared to Au parallel bars.

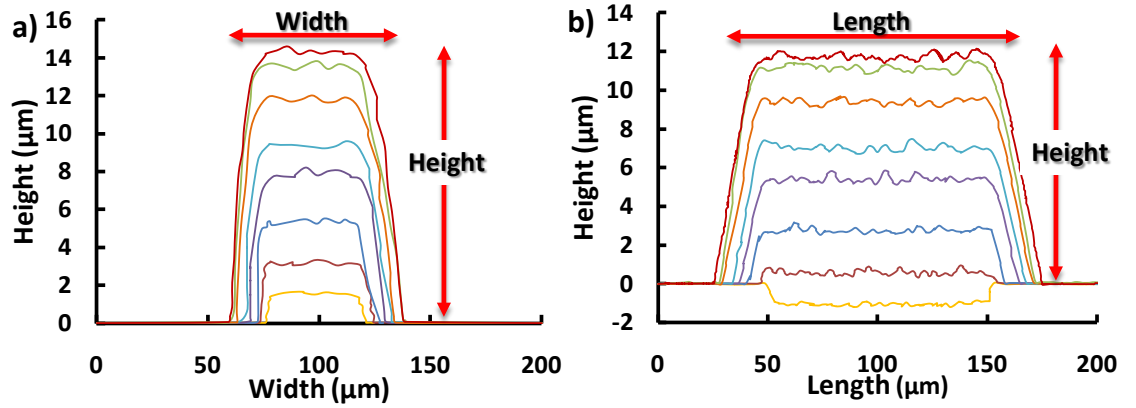

Figure 19: Sequential polymer growth on a Au bar measured using the profilometer – **a)** On a single Au bar PPy(DBS^-) (*- line*) was grown to calculated thickness associated to charge (*100*, *250*, *500*, *750*, *1000*, *1250*, and *1500* $mC \cdot cm^{-2}$) and measured using the profilometer. **b)** On the 100 µm of photoresist the length was initially measured using the profilometer to show the depth of the deposition window while the polymer growth is well over the photoresist layer.

With the height, width, and length plotted versus the charge per unit area (actual measured area from Figure 19) the growth is shown to be linear in all directions (Figure 20). From Figure 18 and Figure 19 it can be seen that the non-uniform polymer growth

rate is about double that in the horizontal than in the vertical direction. Since previous calibrations were done on a homogeneous electrode of indium tin oxide (ITO) it is difficult compare to our electrode geometry. Therefore for the particular parallel electrode geometry a calibration based on our system was required and conducted using a single Au bar with PPy(DBS^-) oxidatively grown on top.

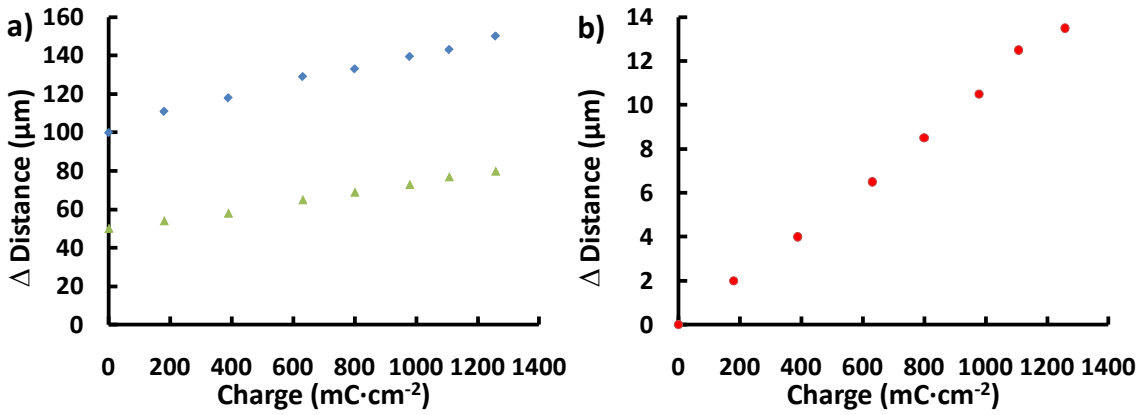

Figure 20: Polymer deposition growth rate conditions – a) The polymer was grown to various calculated thicknesses (Figure 19) the width *(green triangles)*, and length *(blue diamonds)* were plotted by the charge per unit area (experimentally measured). **b)** The height *(red circles)* indicates the growth at a significantly lower rate.

To determine what effect polymer thickness would have on the parallel bar geometry, the drain current (DC – the current measured from source to drain) of a single junction was subsequently measured after polymer was deposited for a 100 s at 1 µA. The current was measured by applying a potential of 0.4 V which is low enough not to induce polymerization but large enough to obtain a measurable current (Figure 16). The effect of polymer thickness once the junction has been bridged is minimal as seen with the levelling off of current after the connection has been made; it requires less

deposition cycles (the number of times the polymer was deposited onto the Au electrodes) for the 5 µm gap spacing (~10) compared to the 45 µm gap spacing (~ 75) (Figure 21).

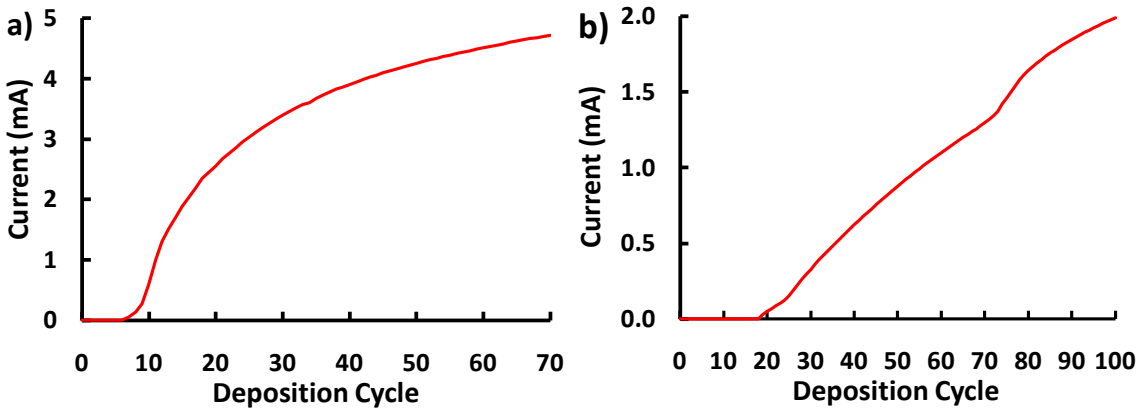

Figure 21: The drain current of a junction measured at 0.4 V after applying a deposition current of 0.1 µA for 100 s – The polymer hybrid was grown on a **a)** 5 µm and **b)** 45 µm gap spacing for 100 s using a constant current of 0.1 µA. After each deposition cycle a DC at 0.4 V was measured to give the associated graph.

After depositing PPy(DBS^-) on the Au bars the films were first rinsed with DI water, and then dried with a stream of N_2. The control window of photoresist must be removed using acetone prior to polymer reduction, as the layer degrades at negative potentials and enters into solution, interfering in the reduction process (Figure 22). There was only a slight change in current observed after the use of acetone to rinse the polymer films which can be considered negligible (Figure 23). To determine the oxidized state of the polymers the *I-V* was measured to 10 mV in air for each set of electrodes, which typically had current measurements within the hundreds of µA region. Scanning to a

low potential of 10 mV ensures that the possibility to react with the atmosphere and residual solvent does not occur within the polymer.

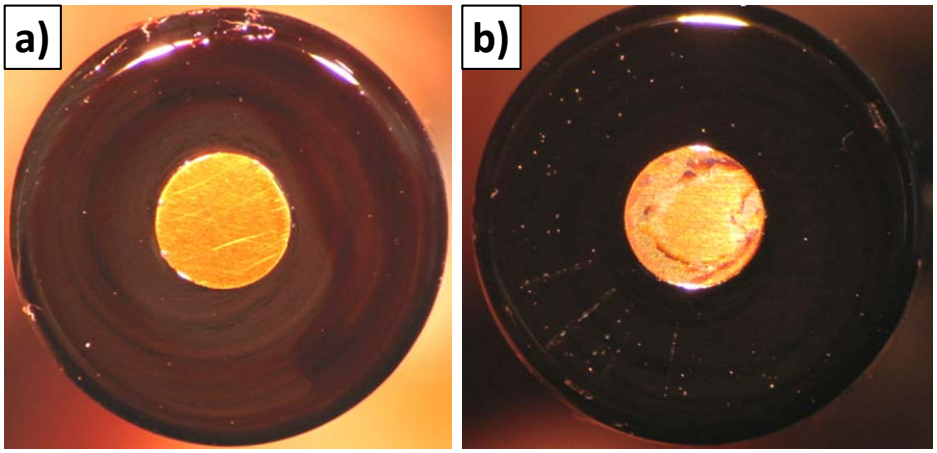

Figure 22: Reduction of photoresist – a) A layer of photoresist was applied to an Au disk electrode and then **b)** reduced at -1.2 V in a solution of $LiClO_4$ to show the degradation that occurs.

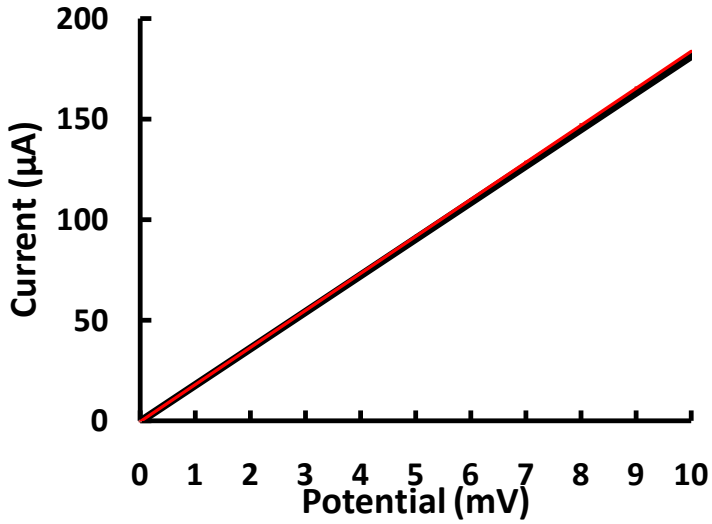

Figure 23: Current before and after photoresist removal – The current of a 5 µm gap spacing was measured before the removal of the control deposition window of photoresist *(black line)*. When the photoresist was removed using acetone the measured current slightly deviates from the previously measured current *(red line)*.

2.2.2.2 Optimized Conditions for Reduction of PPy(Li^+DBS^-)

The PPy system with dopant anions of DBS^- incorporated can present a high degree of strain upon reduction.[128-132] Smela et al. determined that the use of water as a solvent can cause the internal structure of the polymer film to significantly change upon reduction, [111-113] which can also be seen with our system. The reduction strain was a challenge for the new electrode architecture, although the approach to promote adhesion helped to overcome those challenges (Figure 24).[125]

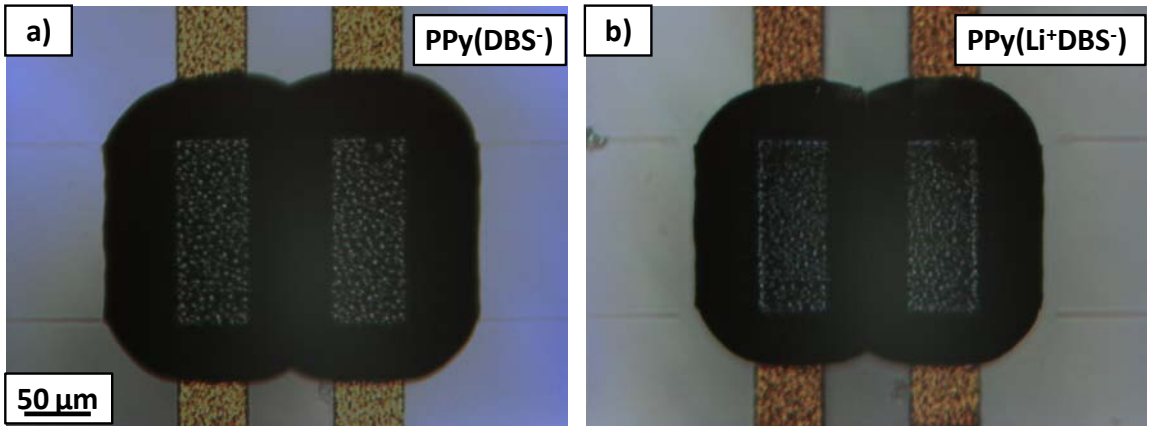

Figure 24: Optical Micrograph of a 45 µm Gap Spacing – Optical micrographs **a)** without the photoresist layer showing the oxidized polymer PPy(DBS^-) and **b)** after the reduction to PPy(Li^+DBS^-) with slight volume changes.

The lower concentration of 0.1 M $LiClO_4$ previously reported could not reduce the current of the polymer an order of magnitude or greater, therefore a higher concentration of 1.0 M $LiClO_4$ was chosen instead. To determine an optimal reduction potential, a CV was obtained by scanning a potential window from -1.2 to 0.4 V at a rate of 0.1 $V \cdot s^{-1}$ (Figure 25). A constant potential of ~-1 V (depending on the condition of the

Ag/AgCl reference electrode REDOX peaks can shift) was applied to all electrodes for a variable amount of time until the current dropped by an order of magnitude or greater (Figure 26). When the reduction process was complete the device was rinsed off with DI water and then dried with N_2.

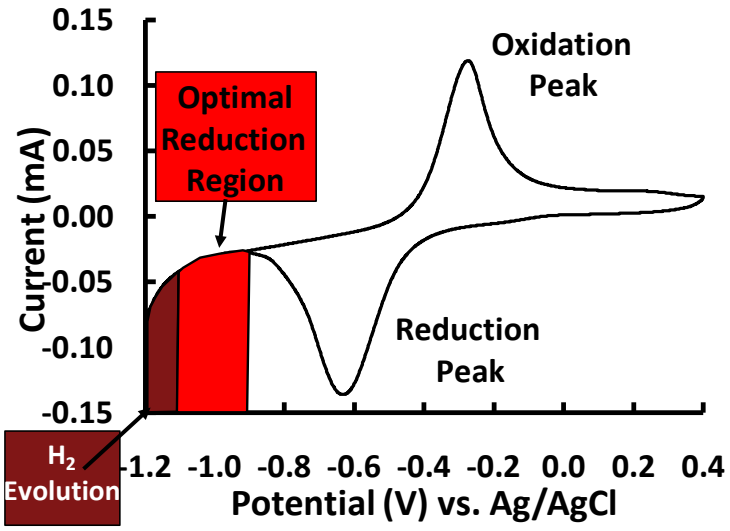

Figure 25: CV of PPy(DBS^-) in 1.0 M $LiClO_4$ – The oxidation and reduction peaks of PPy(DBS^-) in 1.0 M $LiClO_4$ was obtained by scanning a potential window from -1.2 to 0.4 V at a rate of 0.1 $V \cdot s^{-1}$. The red area indicates an optimal reduction potential for the polymer hybrid to create PPy(Li^+DBS^-). The darker region is where H_2 begins to evolve which can degrade the properties of the polymer. In many cases the polymer would delaminate or contract destroying the junction.

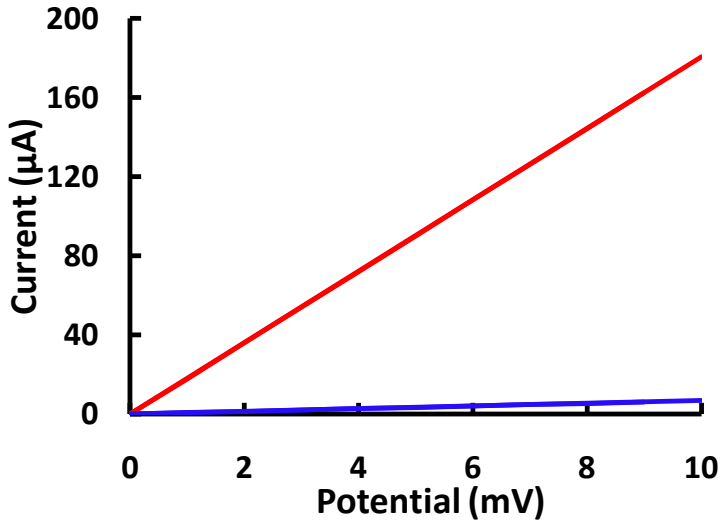

Figure 26: *I-V* measurement of a 5 µm gap spacing before and after the reduction process – The polymer hybrid of PPy(Li^+DBS^-) in the oxidized state PPy(DBS^-) *(red line)* drops in current at least two orders of magnitude to confirm the completion of the reduction process *(blue line)*.

2.2.2.3 Optimized Polymerization for Polypyrrole

A control polymer of PPy without any ions inserted was deposited spanning the variable lengths of the fabricated Au parallel bars. The same oxidative polymerization method (Section 2.2.2.1) was followed although ClO_4^- was chosen as the counterion instead of DBS^-, by combining 0.1 M PPy with 0.1 M $LiClO_4$. Upon reduction, the ion of ClO_4^- is small enough to drift back into solution creating the neutral polymer of PPy upon reduction following the same procedure outlined in Section 2.2.2.2.

2.2.2.4 Optimized Drying Conditions

The average humidity of most rooms range from 30 to 50 % relative humidity (RH) which is standard to minimize the growth of most biological contaminants such as mold.[133] Hydration effects have been reported at 50% RH within PPy doped systems [134-139] and can alter the electronic response. Therefore, the polymer was left in a dry N_2 atmosphere for ~5 days (Figure 27b) prior to any further experimentation as the available vacuum systems were insufficient to thoroughly drive out the solvent within the polymer (Figure 27a). Further electronic analysis (*I-V* and potential step experiments) in a two electrode setup (*red* and *white leads* connected as first electrode and *green lead* as the second electrode) were conducted in an inert atmosphere of N_2 to avoid any potential side reactions with the atmosphere. When conducting experiments in the presence of water or oxygen, issues such as poor reproducibility of the *I-V* between samples arose but under N_2 these issues disappeared.

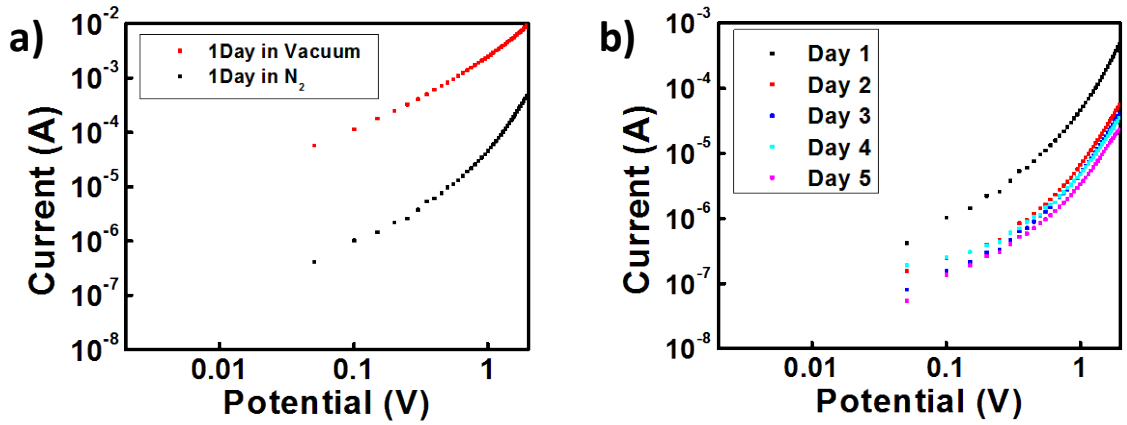

Figure 27: *I-V* measurements made over several days – a) Preliminary testing on IDAs determined that drying the polymer 1 day in N_2 was significantly faster than vacuum. **b)** The *I-V* measurements were followed for 5 days of drying in N_2.

2.2.3 Surface Imaging

A PM5 probe station (SUSS MicroTec) was used to obtain the various optical images for the Au and the various polymers deposited onto the Au substrates using a 20x magnification lens. Images were captured using an Infinity 2 digital camera attached to the probe station.

2.2.4 Scanning Electron Microscopy

Both the bare and polymer deposited Au bars were imaged with a Cambridge Stereoscan 120 Scanning Electron Microscope. The polymer substrates were sputter-coated (Edwards) with a thin layer of Au for imaging. The samples were imaged using a

20 keV electron accelerator beam. Three polymer systems of PPy (Section 2.2.2.3), PPy(DBS^-) (Section 2.2.2.1), and PPy(Li^+DBS^-) (Section 2.2.2.2) were examined on each gap spacing using SEM. The SEM images are discussed in detailed within Chapter 3 Section 3.2.1 and 3.2.2.

2.2.5 Surface Profilometry

An Alpha Step 500 general surface profiler was used to measure film thickness and characterize the device structure. Since a large area (100's of µm) was required to be scanned, atomic force microscopy (AFM) or scanning tunnelling microscopy (STM) could not be done. The profilometer was set up by placing the samples onto the stage and aligning the profiling tip, the sample was then scanned to determine the heights of the various electrode structures and deposited polymer. The distances between the two electrodes were also obtained to confirm the resolution of the fabrication process (Figure 28). The gap spacing of 2 µm was usually difficult to achieve as the spacing was either over-etched or not separated during the etching process and therefore not used for experimental analysis. For gap spacings≤ 10 µm a ≥ 10 % standard deviation can result for these lower spacings (Figure 28). While gap spacings that are > 10 µm a ≤ 5 % standard deviation occurs for the larger spacings (Figure 28).

Gap Spacing (µm)	Min (µm)	Max (µm)	Average (µm)	Standard Deviation (µm)
2.00	4.36	5.54	**5.07**	0.56
5.00	6.73	8.52	**7.70**	0.74
10.00	11.48	13.70	**12.58**	0.99
15.00	16.24	18.20	**17.42**	0.85
20.00	20.99	22.38	**21.94**	0.64
25.00	25.74	28.00	**27.00**	0.95
30.00	30.89	32.90	**32.28**	0.95
35.00	36.04	38.21	**37.17**	0.95
40.00	40.08	42.71	**41.87**	1.22
45.00	45.93	47.52	**46.67**	0.66

Figure 28: The error of gap spacing that occurs due to the fabrication process – The smaller gap spacing of 2 µm was usually harder to achieve due to the etching process as compared to the larger gap spacing of 45 µm which can be easily patterned.

2.2.6 Temperature Measurements

Temperature dependence measurements were conducted to further understand carrier mobility within the system. A range of temperatures from ~268, 283, 298, and 313 K was applied to the system while obtaining electronic measurements in a two electrode setup. A specially designed glass chamber was created and attached to a Fisher Scientific Isotemp 3016 refrigerated circulator capable of controlling the temperature (Figure 29). The fabricated device was encapsulated within the chamber under an inert atmosphere of N_2 and connected by leads to the CHI-760C workstation.

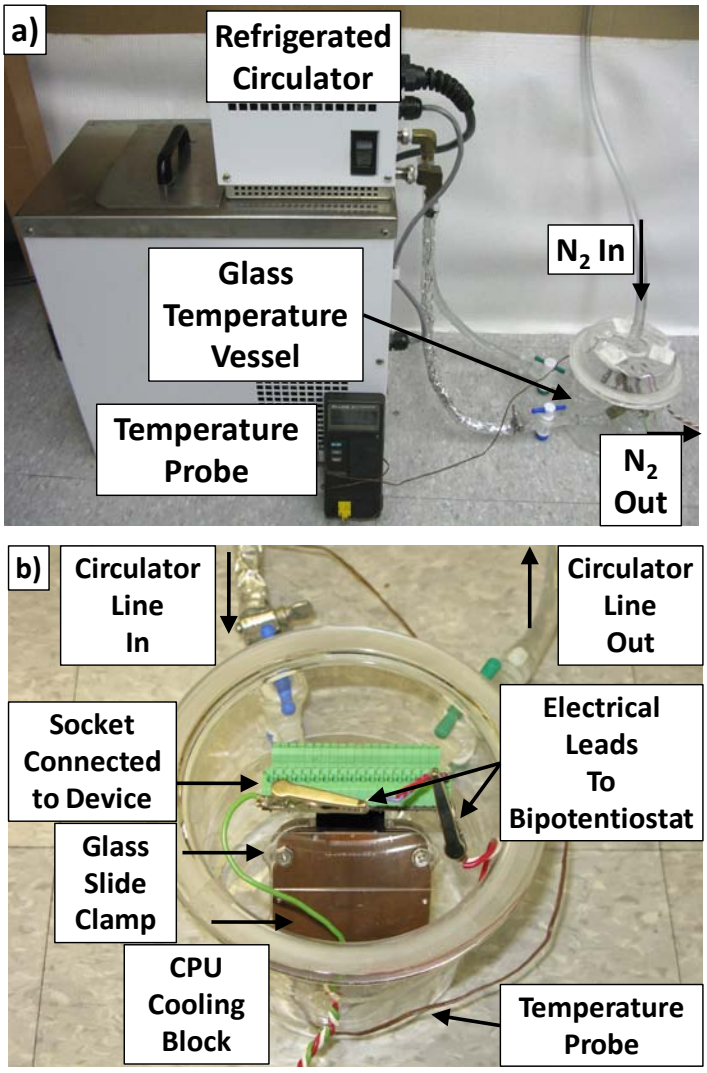

Figure 29: Temperature Dependence Setup – a) A refrigerated circulator connected to the custom glass temperature chamber. **b)** A close-up of the glass chamber with a device placed onto the temperature controlled surface.

2.2.7 Simulation

To understand how the system is affected by the changes in dimensions of electrode spacing, computer simulations were conducted using Comsol Multiphysics 3.5. Computer simulation allows the modeling of behaviour based on the material and

architecture to gain insight into parameters dominating device performance correlating experimental data. When designing the computer model, the specific experimental parameters such as dimension and current were chosen and explained within the subsequent paragraphs.

Initially, a 2-dimensional (2-D) symmetric simulation was performed using a basic design of one Au electrode and half the polymer to save on computational processing and time. The Au electrode design was chosen with a width of 50 µm, a height of 1.5 µm and a 0.1 V applied potential. A polymer material with a thickness of 20 µm, and a width of 100 µm was placed on top of the electrode. The electrode spacing was varied from 5 to 45 µm, by moving the 0.1 V electrode half the distance from the grounded side of the polymer. The current at the ground electrode was obtained by altering the conductivity in the x and y dimensions (Figure 30). Further discussion will proceed in Chapter 3 Section 3.2.1.1 based on the changes in conductivity and the currents obtained to correlate the experimental data.

When designing a more realistic model in 3-D, a similar model of two ohmic contacts of Au with a width of 50 µm, length of 150 µm, height of 1.5 µm and conductivity of 4.5 x 10^9 $S \cdot m^{-2}$ was chosen (discussed further in Chapter 3 Section 3.2.2.1). The spacing between the two electrodes was again varied based on the predefined distances of the fabricated parallel bars from 5 to 45 µm. A polymer material was chosen with a thickness of 20 µm, a length of 100 µm and a width of 180 µm plus the gap spacing. The predefined polymer material was altered by changing the conductivity in three

dimensions to x=100 $S \cdot m^{-1}$, y=100 $S \cdot m^{-1}$, and z=1 $S \cdot m^{-1}$. By applying a constant potential of 2 V to a single electrode and setting the other electrode as the ground, the current through the polymer was set to 1 x 10^5 $A \cdot m^{-2}$ (calculated from experimental data at 2 V). The parameters were meshed as an extruded rectangle to incorporate 100 elements within the polymer while the Au bars only had 10. The polymer hybrid system was then solved for the electric field and potential (Figure 31). Detailed discussion regarding the simulation data will proceed in Chapter 3 Section 3.2.2.1, including an explanation of the correlation to the experimental data.

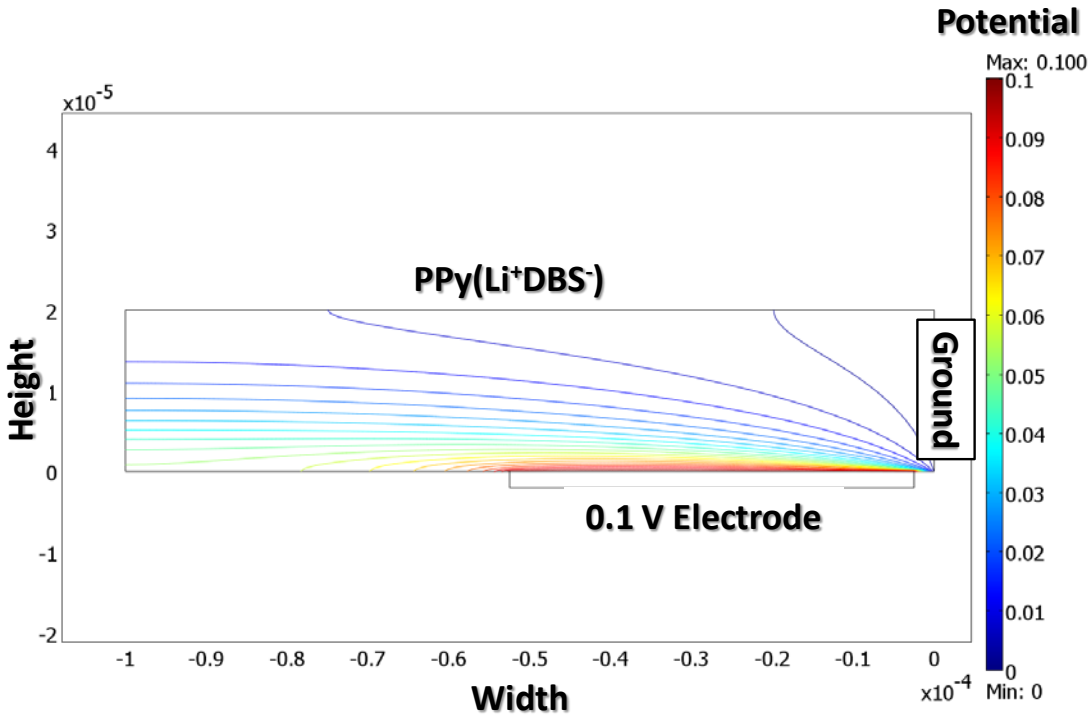

Figure 30: 2-D simulation image description – The above image is generated as a half model from the computer simulation for the polymer system using the indicated parameters. The generated current was solved at the ground electrode, which is considered to be the mid-point of the polymer material. The data obtained is used for Figure 46 and Figure 47 in Chapter 3 Section 3.2.1.1

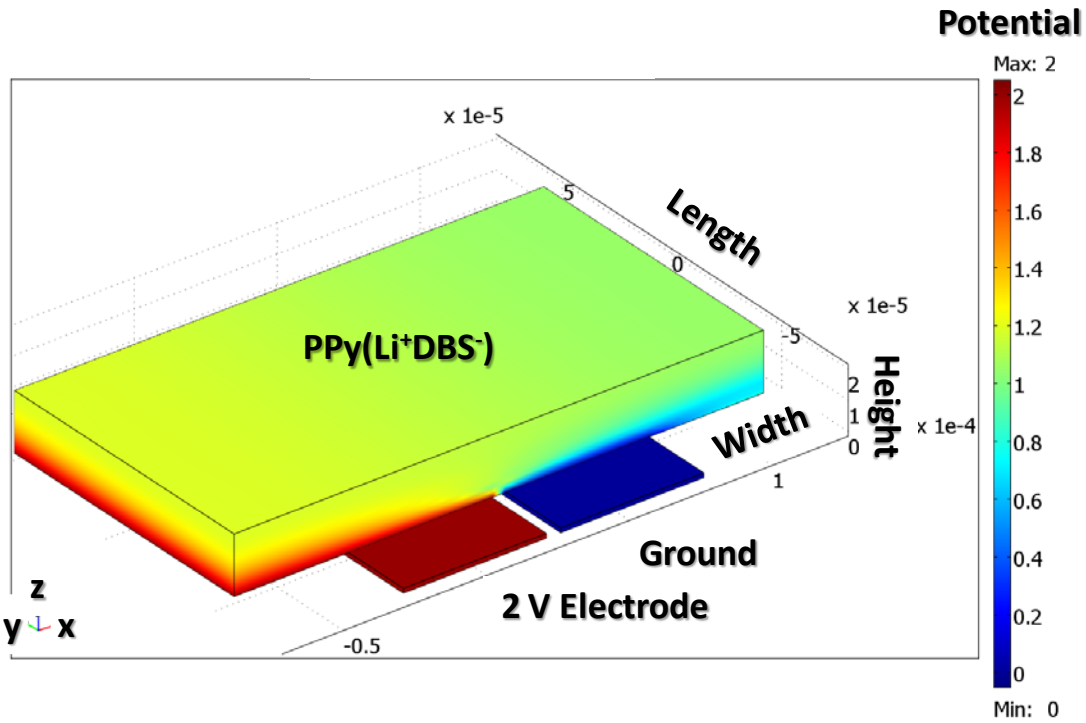

Figure 31: 3-D simulation image description – The above image is generated when inputting the indicated parameters to solve for the polymer systems potential map. Labels are added to define each area to explain the images within Chapter 3 Section 3.2.2.1.

Chapter 3 Scaling Properties of PPy(Li^+DBS^-)

3.1 Conduction Mechanisms of Polymers and Related Materials

3.1.1 General Overview

The various memory materials and designs currently being researched have shown promise over conventional devices; however they are hindered by specific disadvantages. Currently, DRAM based on the 1T-1C cell is able to operate with read and write times less than 15 nanoseconds cycled countless times.[5] The main limitation of DRAM based devices is their inability to further scale down dimensions within the fabrication process due to limitations of the required materials and methods. Scaling issues related to further increasing the density of current devices (previously discussed in Chapter 1 Section 1.1.3) has brought forth alternative technological designs and devices to potentially revolutionize the memory industry.

Polymer based memory devices need to have read and write times within the nanosecond region in order to be a competitive alternative to current DRAM based devices. These times have been achieved by Yang et al. with a polyaniline hybrid containing nanoparticles,[140] although a thorough study of the stability of the polymer system has not been performed. Galatsis et al. have stated that polymeric materials are promising alternatives for non-volatile applications as they are beneficial in lowering processing costs, although further investigation of their overall stability is required.[34]

There are several polymer systems presented with the possibility for integration into electronics as a memory device, although a thorough understanding of these systems is considerably lacking. The polymer hybrid system of PPy(Li^+DBS^-) has been previously reported with micrometer wide electrodes of an interdigitated array (IDA) [28] and then down to the nanometre region using the crossbar geometry [71] with the ability to demonstrate characteristic electronic signals (*I-V* and potential step) due to field induced ion mobility. A comparison of the currents generated for the two electrode geometries (despite the very different designs) were reported to increase by an order of magnitude from the IDA to the crossbar. The change in current would suggest that the dimensional factor of electrode spacing was the basis for the increase and therefore the polymer could display an even better response as the dimensions were further reduced. By systematically studying the scaling properties of the polymer hybrid PPy(Li^+DBS^-), the electronic response of a device with dimensions smaller than previously fabricated can be understood.

The different conduction regions of ohmic, space-charge-limited current (SCLC) and field generated charge carrier current (FGCC) (presented under the nonlinear curve of PPy(Li^+DBS^-) in Figure 32) will be thoroughly discussed in the subsequent sections. Different solid-state polymers (in the absence of electrolyte) were examined on IDAs so as to better understand the hybrid system (Figure 32a). Both the oxidized PPy (*red line*) and reduced PPy (in the absences of ion pairs *black line*) display typical ohmic behaviour. In contrast, the reduced PPy containing Li^+ and DBS^- (*blue line*) exhibits

unique nonlinear behaviour attributed to the movement of cations. This system exhibits ohmic behaviour at low fields, space-charge-limited current (SCLC) at intermediate fields, and field generated carrier currents at larger fields (FGCC). A similar response of nonlinear behaviour can be seen with a crossbar junction of PPy(Li^+DBS^-) exhibiting the different conduction regions (Figure 32b).

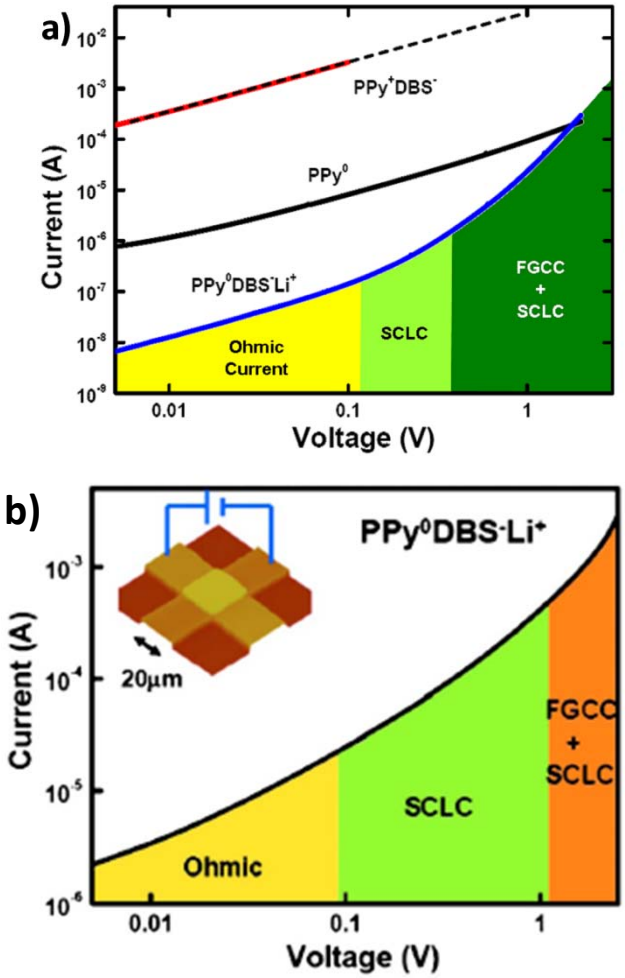

Figure 32: *I-V* behaviour of various polymers – a) Different solid-state polymers were examined on IDAs of the oxidized PPy(DBS^-) (*red line*), and reduced PPy (*black line*) display typical ohmic behaviour. [28] The reduced PPy containing both Li^+ and DBS^- (*blue line*) exhibits ohmic behaviour at low fields, space-charge-limited current (SCLC) at intermediate fields, and field generated carrier currents at larger fields (FGCC). **b)** A crossbar junction showing similar nonlinear behaviour with the different conduction regions exhibited by PPy(Li^+DBS^-).[71]

The conductivity of conjugated polymers between the oxidized (doped) to the reduced (undoped) form have been reported to range 15 orders of magnitude due to the different doping levels and various composites.[141] The high conductivity is usually

reported in the doped oxidized state while the undoped is typically very low in conductivity and not utilized for many studies. There are many reports of different conductivities based on the solvent [142] and electrochemical conditions [143] by which the polymer is grown. By far the most studied condition for PPy growth is associated with the counter ion. While PPy(DBS^-) conductivity has previously been reported within an electrolytic medium, solid-state studies are rarely seen.[100, 144]

The solid-state polymer hybrid of PPy(Li^+DBS^-) can initially be considered as an undoped neutral polymer with low conductivity; the presence of a field results in Li^+ drifting, leaving behind DBS^- and allowing the region to become doped (i.e. injection of charge carriers is balanced by DBS^-). Since there are no charge carriers within the polymer hybrid of PPy(Li^+DBS^-), it is analogous to compensation doping (a common method utilized to develop intrinsic inorganic semiconductors to compensate charge carriers by creating impurities).[145] Compensation doping of the polymer hybrid is used to create a region that contains a sufficient level of anions to support the doped form of the polymer upon movement of the compensating ion.[146]

3.1.2 Ohm`s Law

Under low potential, current flows through the polymer hybrid following Ohm`s law which states that the current (*I)* through a conducting medium is directly proportional to

the potential difference (*V)* and inversely proportional to the resistance (*R)* of the material (Equation 3.1) (Figure 6b).

$$I = \frac{V}{R} \tag{3.1}$$

Resistivity *(ρ)* is simply the inverse of the conductivity *(σ)* and can be further related by

$$\rho = \frac{1}{\sigma} = R\frac{A}{L} \tag{3.2}$$

where *R* is the resistance of the material, *A* is the area of the electrical contact, and *L* is the length of conducting material or the distance between two electrical contacts. Literature typically reports the conductivity of PPy within a variety of ranges depending on the polymerization conditions and incorporated counterions (Figure 33). Comparing the obtained data from the oxidized polymer of PPy(DBS^-) the conductivity is generally high ~10^1 $S{\cdot}cm^{-1}$ similar to previously reported conductivities. Once reduced the conductivity of the polymer hybrid of PPy(Li^+DBS^-) drops several orders to ~10^{-2} $S{\cdot}cm^{-1}$ which is higher than the reduced undoped form of PPy but still lower than the doped PPy systems.

Polymer	PPy	PPy	PPy/pTS	PPy/MS	PPy/DS	PPy/DBS
Counterions		ClO_4^- BF_4^-	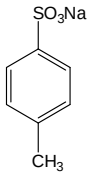	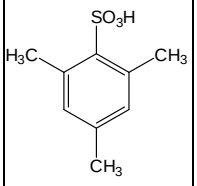	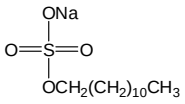	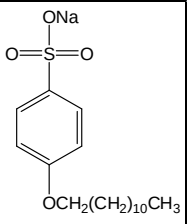
Conductivity ($S \cdot cm^{-1}$)	10^{-10}-10^{-9}	90-110	90-110	50-70	40-150	50-80

Figure 33: Conductivity of polypyrrole films with some common counterions – The conductivity can range from 10^{-10} - 150 $S \cdot cm^{-1}$ [100, 141, 144, 147-149] depending on the growth conditions, counterion, solvent temperature, and applied potential.[81]

An equation commonly employed to measure the ability of a material to conduct a current (*I*) through a given area (*A)* is defined as the current density *(J)* with units of $A \cdot cm^{-2}$ (Equation 3.3).

$$J = IA^{-1} = I[HW]^{-1} \tag{3.3}$$

Area is often broken down into height *(H)* and width *(W)* where these dimensions are shown graphically in Figure 34. The current response is seen to scale with all three dimensions (Equation 3.4), as indicated in the above equations.

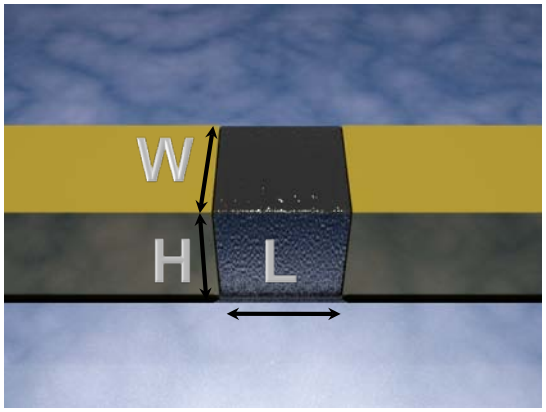

Figure 34: Three different dimensional parameters of H, W and L between two ohmic contacts – The path of current flow would be through the shortest distance between two electrical contacts which would provide the least resistance.

$$I \propto \frac{HW}{L} \tag{3.4}$$

The current *(I)* for semiconductors is associated with the drift of positive (holes) (Equation 3.5) and negative (electrons) (Equation 3.6) charge carriers.[150]

$$I = qp\mu_p \frac{V \cdot HW}{L} \tag{3.5}$$

$$I = qn\mu_n \frac{V \cdot HW}{L} \tag{3.6}$$

Where q is the elementary charge (1.6 x 10^{-19} C), μ is the mobility of charge carriers ($m^2 \cdot (V \cdot s)^{-1}$), V is the applied potential (V), and H, W and L are the dimensions described above. Previously reported time-of-flight measurements have shown that the bulk limited transport of the positive carriers *(p)* concentration in polyphenylene vinylene (PPV) (a conjugated, undoped polymer) dominates the *I-V* characteristics.[151] Using

similar techniques, the contribution of the injection and transport of the negative carrier *(n)* concentration was determined to be negligible for the *I-V* characteristics of the PPV system.[152] By utilizing Equation 3.5 an ohmic current within PPy(Li^+DBS^-) can be calculated based on the positive carriers of a finite mobility *(μ_p)*. Thus, only current resulting from *p* will be considered and not the current resulting from the *n* and negative carrier mobility *(μ_n)*. In order to determine how the ohmic current would scale, if all dimensions of *H, W* and *L* were reduced by a factor of *S* each component would be HS^{-1}, WS^{-1}, and LS^{-1}; as per Equation 3.5 the current *(I)* would then be proportional to S^{-1} (Equation 3.7). This is similar to conventional resistors where the current would decrease by an order of magnitude when all dimensions were reduced.

$$I \propto S^{-1} \tag{3.7}$$

In contrast to this, the current of capacitors and diodes scale as a factor of S^{-2}. Devices comprised of capacitors and diodes scale differently since they scale as a function of area and thus independent of *L*. The scalability of these devices is limited due to the quantum effects that occur when dimensions are reduced past 10 nm (Chapter 1 Section 1.1.3).

3.1.3 Space-Charge-Limited Current

Space-charge-limited current (SCLC) is another mechanism by which current flows through PPy(Li^+DBS^-). When a system is in the region where SCLC dominates, only one

type of charge carrier (holes in this case) are injected into the material from a contacting electrode and are collected at the counter electrode to give the resulting current (Figure 6b). For SCLC the model assumes a perfect trap free material (where there are no restrictions for the movement of holes and electrons) and an electrode is assumed to be an infinite source for carriers. The *I-V* behaviour can be described by the Mott-Gurney square law [150, 153-157]

$$J = \frac{9}{8}\varepsilon_r \varepsilon_0 \mu \frac{V^2}{L^3} \tag{3.8}$$

where ε_r is the dielectric constant, ε_0 is the permittivity of free space (8.854 x 10^{-12} F·m), μ is the finite mobility of charge carriers, V is the applied potential, and L is the path length between ohmic contacts. The permittivity of free space (ε_0) and dielectric constant (ε_r) can be combined as the permittivity of the polymer $\varepsilon=\varepsilon_0\varepsilon_r$.[154] The SCLC is a result of positive charge carriers (a common conduction method for conjugated polymers) [154] where the mobility (μ) is designated as the mobility of holes (μ_p) and therefore the current flow through the polymer hybrid can be defined as

$$I = \frac{9}{8}\varepsilon \mu_p \frac{V^2 \cdot HW}{L^3} \tag{3.9}$$

The SCLC scales with changes in dimensions of *H, W*, and *L* as defined by Equation 3.9, therefore the current is determined by a factor of L^{-3} making the system highly dependent to changes in the length of material between electrodes. In the case of SCLC, if all dimensions of *H, W* and *L* were reduced by a factor of *S* each component would be

HS^{-1}, *WS*$^{-1}$, and *LS*$^{-1}$. As per Equation 3.9, the current *(I)* would be proportional to *S* (Equation 3.10). The current in this case will increase as dimensions are decreased in contrast to materials dominated by ohmic currents.

$$I \propto S \tag{3.10}$$

The parameters such as μ_p and ε of the polymer hybrid PPy(Li^+DBS^-) have yet to be determined. Previously reported time-of-flight measurements have determined the μ_p = 5 x 10^{-11} $m^2 \cdot V^{-1}$ in PPV,[1, 158-161] although measurements based on the polymer hybrid PPy(Li^+DBS^-) have yet to be conducted. There are prior reports regarding the ε_r, ranging from 2.5 to 3.5 for PPy colloid dispersions [162, 163] but there have been no reports for PPy films containing ions of Li^+ or DBS^-. Comparing previously reported values of different polymer systems cannot be quantitatively done due to the unique properties of the polymer hybrid PPy(Li^+DBS^-). A direction for future work could be to conduct a thorough investigation regarding the μ_p and ε_r of PPy(Li^+DBS^-), but was not examined within this work.

3.1.4 Field Generated Charge Carrier Current

The solid-state polymer hybrid of PPy(Li^+DBS^-) shows an electronic response at higher fields that can be explained by the field induced motion of Li^+ (Figure 6c and Figure 36). Models of ion mobility have previously been reported by Heeger et al.,[164] Friend et al.,[160] and Leger et al. [165] in response to an applied external field with defined regions

within a light-emitting electrochemical cell (LEC) of polyethylene oxide (PEO - a polymer electrolyte) (Figure 35).

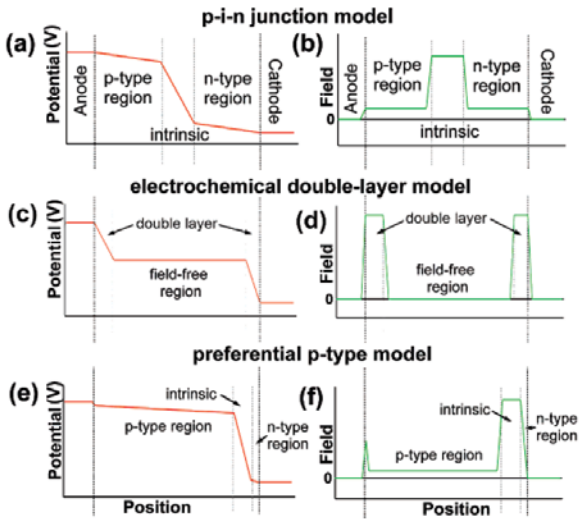

Figure 35: Various proposed models of the potential profiles and electric fields within light-emitting electrochemical cells – Initial brought forth by Heeger et al. as a p-i-n junction model (**a** and **b**) then as an electrochemical double layer model by Friend et al. (**c** and **d**) and the preferred p-type model defined by Leger et al. (**e** and **f**). The definition of the potential profiles is set as positive at the anode and negative at the cathode.[166]

Heeger et al. presented a model based on the formation of a p-type/intrinsic/n-type (p-i-n) junction as a result of doping. The p- and n-type regions are created near the electrodes while an intrinsic area (where most of the potential drop occurs) is formed in the middle.[164] The model that Friend et al. proposed has the formation of an electrochemical double layer being created near the electrodes resulting in a large field drop near the electrodes with a nonexistent field throughout the bulk of the material.[160] The most recent model proposed by Leger et al. defines a field contained mainly within the bulk of the material with an intrinsic region created near a contacting electrode.[165]

The double layer effect of PPy(Li^+DBS^-) is theorized as a result from the molecular reconfiguration of the ionic species Li^+ at the cathodic electrode when an external field is applied (Figure 36).[28] Heeger et al. suggests that doping occurs at both electrodes due to the mobility of both cations and anions.[164] The model proposed by Friend et al. suggests that the formation of a double layer can occur without doping.[160] Since the devised system of PPy(Li^+DBS^-) can result in the movement of only cations, where the anions are "locked" in a spatial distribution to support the doped form of the polymer, a combined model involving both the doping and double layer formation may exist.[167] There have been previous reports utilizing the field induced mobility of ionic species to gain an understanding of systems that generate unique electronic signals for applications in dynamic memory.[168, 169]

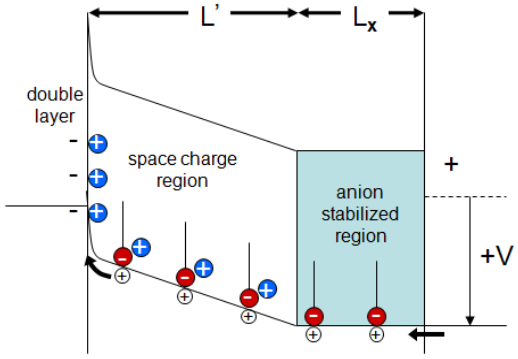

Figure 36: Proposed conduction model of field generation carrier current.

The field induced drift of Li^+ results in a double layer leaving behind DBS^- to create a region of PPy(DBS^-). The region where there is only DBS^- *(L_x)* would support the injection

of charge carriers thereby reducing the original conduction length *(L)* to a smaller length *(L')* (Figure 36 and Equation 3.11). Under these conditions, SCLC would remain a mechanism of conduction, although through a smaller effective *L*, the movement of cations must be taken into account therefore the current of Equation 3.8 can be altered using a new distance *(L')* resulting in Equation 3.12.

$$L^{'} = L - L_x \tag{3.11}$$

$$I = \frac{9}{8}\varepsilon\mu_p \frac{V^2 \cdot HW}{L^{'3}} \tag{3.12}$$

Similar to the SCLC region the current in the FGCC should scale accordingly to the dimensional length of *-3.* Since the distance between the two electrodes decreases under these conditions even further, if all dimensions of *H, W* and *L* were reduced by a factor of *S* each component would be HS^{-1}, WS^{-1}, and LS^{-1}. As per Equation 3.12 with the decrease of *L* to *L'* the current *(I)* in the FGCC region should scale greater than in the SCLC region (Equation 3.13).

$$I \propto S^{n}, \quad n > 1 \tag{3.13}$$

3.1.5 Temporal Behaviour

To further understand the basis for the reconfiguration of ionic species within PPy(Li^+DBS^-) the time-dependant behaviour of current can be examined. The current

within the conduction regions of ohmic and SCLC exhibited by PPy(Li^+DBS^-) reaches steady-state values virtually instantaneously. However, from the proposed model of Figure 36, FGCC it is expected to exhibit temporal behaviour associated with the ionic drift. The application of an external field to the system creates a conducting region where DBS^- can support hole injection due to the drift of Li^+. The field associated with the Li^+ double layer drives the system back to the initial state in the absence of an external field.

When the potentials are low where ionic drift is not significant, the temporal behaviour of the current does not change as a function of time. Once a large potential is applied, the current will increase until reaching a higher steady state current. Both the movement to create the double layer and the subsequent relaxation causes the polymer hybrid to exhibit a unique electronic response once an intermediate negative potential has been applied after a positive potential (Figure 37).

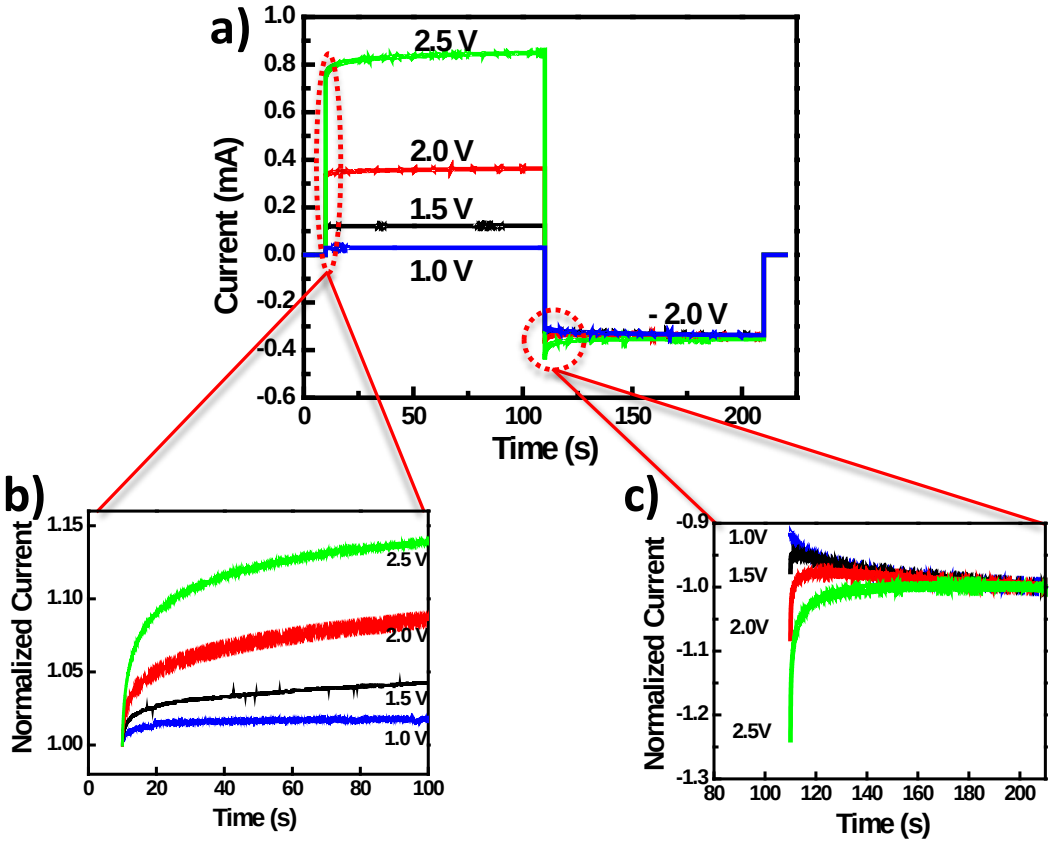

Figure 37: Potential step experiments at various potentials – a) The results of a double potential step experiment with the overlaid increasing positive potentials and the same negative intermediate potential. The first step shows a progressively larger current being generated as potential increases which is a behaviour associated with ion drift **(b)**. The second step reverses the field, exhibiting the transient behaviour associated with the distribution of ions established in the first step **(c)**.

The time scale of the transients in working memory devices will operate independent of cross-sectional area, but will be determined by ion drift (i.e., FGCC), which is in turn determined by the electric field ($E=V\cdot L^{-1}$) and the distance the ions must drift (L_x) to produce a signal. For a constant applied potential,

$$v_x = \frac{L_x}{t_x} = \mu_i(T)\frac{V}{L} \tag{3.14}$$

it is expected that the velocity (v_x) will increase, decreasing L to L' effectively decreasing the distance ions will have to drift (Equation 3.11). Therefore it is expected that the time scale (t_x) dependence will decrease as per the scaling factor within the FGCC (Equation 3.13). The ion mobility (μ_i) indicated in Equation 3.14 is associated with the mobility of the Li^+ relating the associated current within the FGCC region (Figure 38). Normalized current (current divided by the lowest current measured) is plotted as a function of time to measure the instantaneous current rise to a steady state where ions have completely moved. This is observed qualitatively in the crossbar geometry where currents reach steady state values on the order of seconds (Figure 39), whereas IDA structures reach a steady state current on the order of tens of seconds (Figure 37).

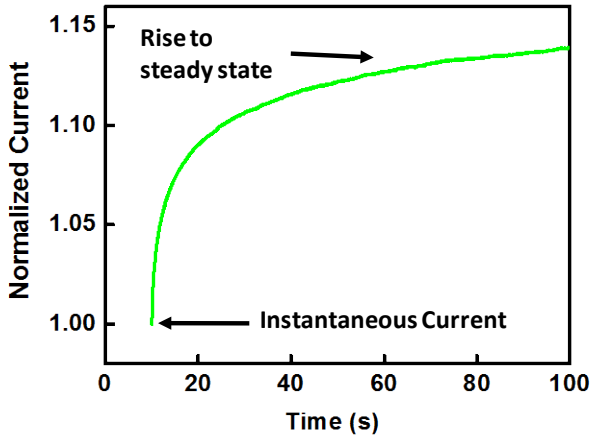

Figure 38: The associated current resulting from the mobility (μ_i) of Li^+– Applying a large potential of 2.5 V causes the system to rise rapidly to a steady state current. Since the potential is large enough to destabilize the ion pairing of Li^+ with DBS^- the current rises further due to the induced movement of Li^+.

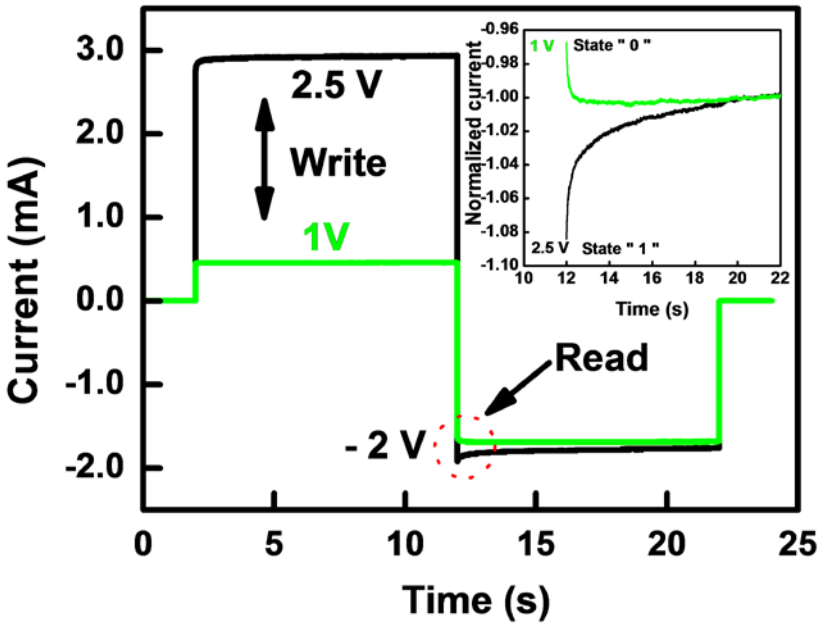

Figure 39: Crossbar potential step and memory effect – The resulting behaviour can be used as the basis for storing two states (*0/1*) in memory devices. The storing states are based on the reconfiguration of ions in the presence of a field (*write*) and the effect on current upon reversing the field (*read*).

The potential for the polymer hybrid of PPy(Li^+DBS^-) for memory devices can be seen in Figure 39 where the write state can be created by using a high or low field, producing significantly different currents. Upon reversal of the field to a negative intermediate potential, the current response can be differentiated and therefore used as the read state. Understanding how the polymer system should scale using the predefined spacing of the parallel bar geometry with variable distances of *L* ranging from 5 to 45

µm can explain the changes seen in the current magnitude from the dimensions in the micrometer of the IDA down to the nanometer crossbar array.

3.2 Scaling Properties of the Current-Voltage Behaviour as a Function of:

3.2.1 Gap Spacing at Low Fields

Using the parallel bar electrodes of controlled gap spacing ranging from 5 to 45 µm and a window of 100 µm, the polymer hybrid of PPy(Li^+DBS^-) was simultaneously deposited on each set of electrodes to yield the oxidized polymer PPy(DBS^-), and subsequently reduced to incorporate Li^+ until the current dropped at least two orders of magnitude (Figure 40).

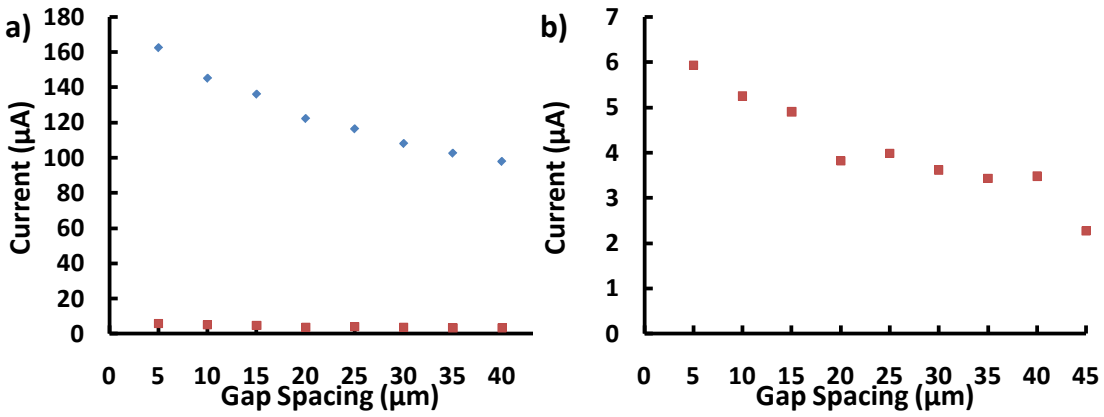

Figure 40: Current measured for each spacing in the oxidized and reduced state of PPy(Li^+DBS^-) – a) The current of the oxidized polymer PPy(DBS^-) (*blue diamonds*) was measured at 10 mV in air for each set of bars where the polymer would generally exhibit current in the range of 100-200 µA. **b)** Upon reduction the current of the reduced polymer PPy(Li^+DBS^-) (*red squares*) would decrease about two orders of magnitude.

The polymer hybrid of PPy(Li^+DBS^-) was grown on each gap spacing to a measured thickness of ~20 µm. The oxidized current at 10 mV was measured in the range of 100-200 µA indicating a relationship of decreasing current with increasing gap spacing following Ohm`s law (Figure 40a). When characterizing the oxidized polymer of PPy(DBS^-) using SEM, the images show a uniform growth on the roughened Au parallel bars (Figure 41). Polymer initially grows within the defined area outlined by the photoresist, but quickly deposits over the insulating layer (i.e. photoresist) contributing to the total area of deposited polymer (previously shown by profilometry measurements in Chapter 2 Section 2.2.2.1). Also the well defined morphology of PPy(DBS^-) can be seen in the SEM images where small nodular growths occur directly on the parallel bars while the surrounding polymer is quite smooth. The nodular growth can be explained by the nucleated growth on the rough surface of the Au plating onto the parallel bars. While the rapid lateral growth can be explained by the hemi-micelle formation due to the use of DBS^-, a surfactant as the counterion.[109]

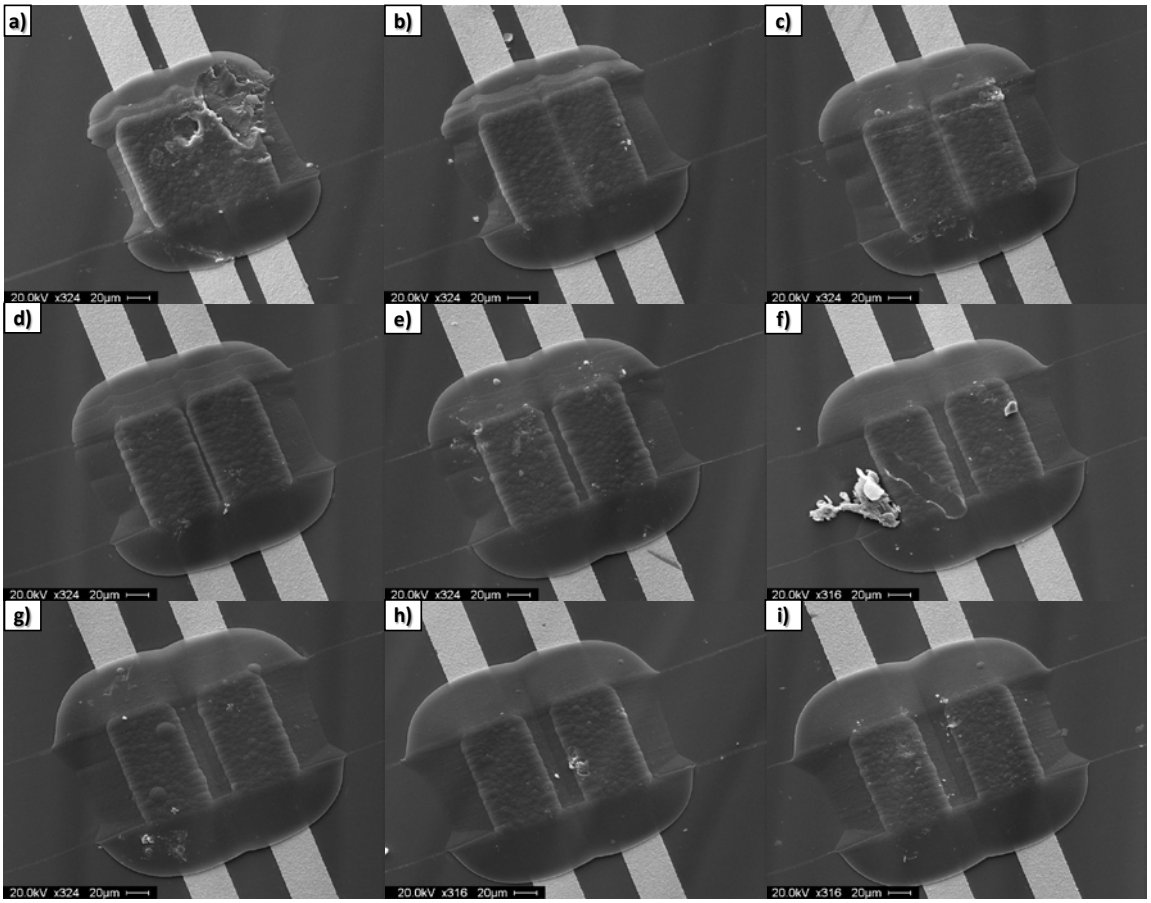

Figure 41: SEM images of the PPy in the oxidized form – PPy(DBS^-) deposited to a calculated thickness of 25 µm on all gap spacings of **a)** 5 µm **b)** 10 µm **c)** 15 µm **d)** 20 µm **e)** 25 µm **f)** 30 µm **g)** 35 µm **h)** 40 µm and **i)** 45 µm

Reduction of the polymer (Figure 40b) results in the current typically dropping two orders of magnitude down to the 1-10 µA range. The same trend seen in the oxidized currents remains in the reduced form where a decreasing current is associated with increasing gap spacing. The fluctuation within the trend is most likely caused by the mechanical stress during reduction, resulting in slight delamination which in turn impacts the total area of electrical contact (Figure 42). The mechanical shrinking due to

the reduction process occurs within all the junctions ranging from the smallest of 5 µm (Figure 42a) to the largest of 45 µm (Figure 42i) where the junction has broken. The reduction strain on the gap spacing of 45 µm was great enough to break apart the junction due to a decreased amount of polymer between the two Au electrodes (Figure 18).

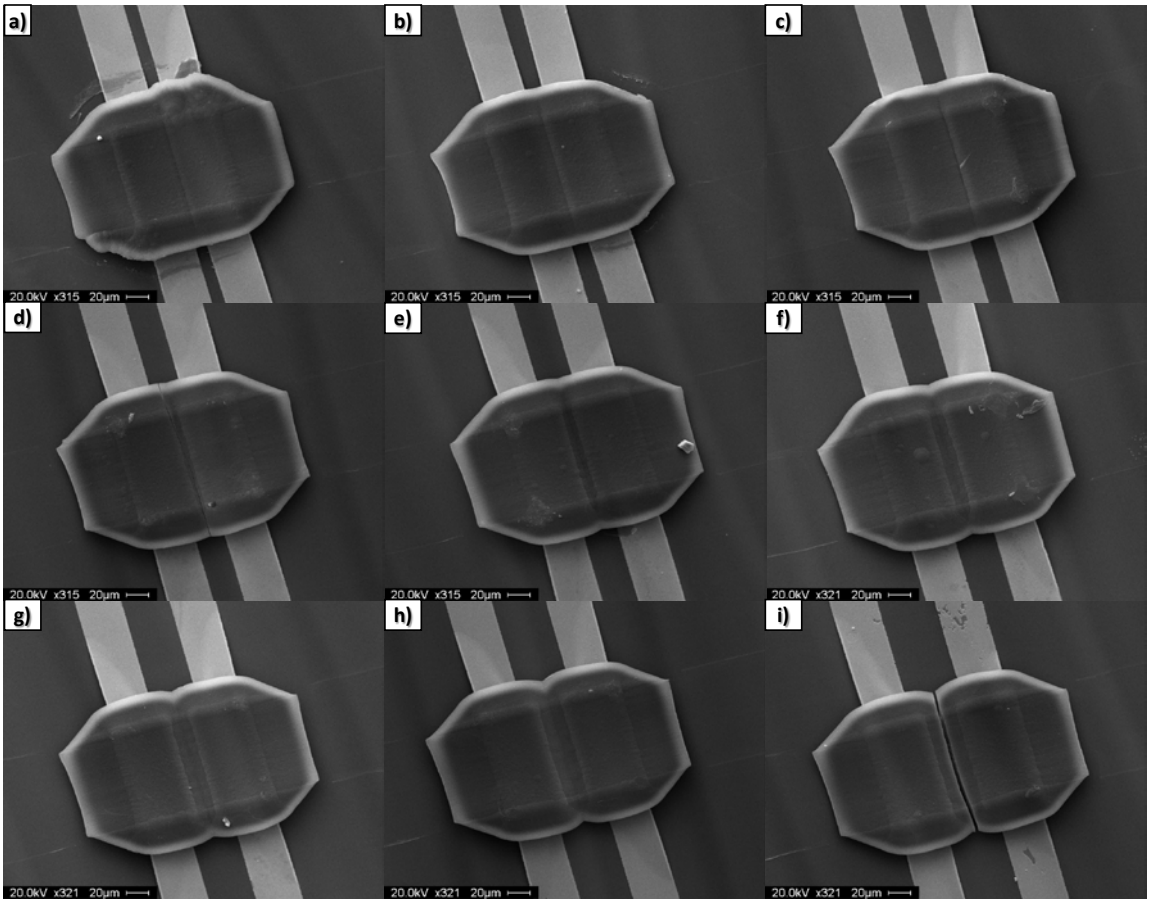

Figure 42: SEM Images of the PPy hybrid – PPy(Li^+DBS^-) deposited to a calculated thickness of 25 µm on all gap spacings of **a)** 5 µm **b)** 10 µm **c)** 15 µm **d)** 20 µm **e)** 25 µm **f)** 30 µm **g)** 35 µm **h)** 40 µm and **i)** 45 µm (broken junction)

Junction defects commonly occur during the reduction process but can also occur during deposition (Figure 43). Defects that can occur are faulty connections leading to Au bars with little or no polymer deposited, rendering the junction useless for further analysis (Figure 43a and b). In cases where there are large mechanical stresses during the reduction process, fractures within the polymer can occur (Figure 43c and d). The *I-V* behaviour of these irregular junctions is either very low or simply results in an open circuit where no current flows through the polymer (Figure 44).

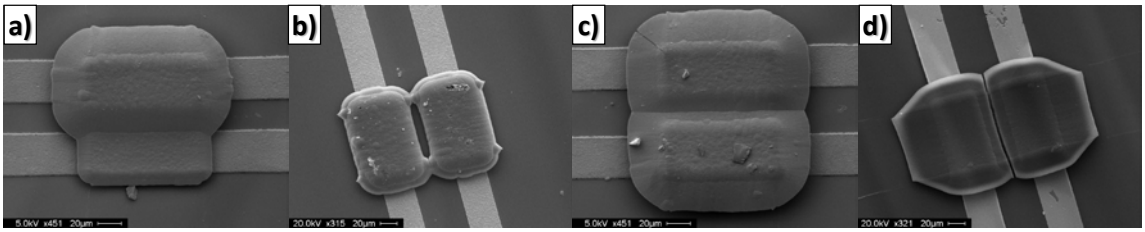

Figure 43: SEM images of irregular junctions – a) A junction where polymer grows from one bar to the next due to a faulty connection in the socket. **b)** When there is not enough polymer deposited, a junction will connect only at the top and bottom and not through the middle. **c)** A slight crack in the junction resulting in poor contacts onto the Au electrode. **d)** A completely broken junction due to polymer contraction during the reduction process.

Another indication of an irregular junction can be clearly seen when plotting the current for each junction at 10 mV. Similar to Figure 40 the current of a defective junction can be seen to deviate from the general trend (Figure 44). An inset SEM image is shown to indicate what the junction looks like when a data point deviates from the associated trend in the oxidized and reduced currents. Aside from observing the gap spacing

optically and determining whether it has been properly formed, a comparison of the current can indicate if the junction will be suitable for further analysis.

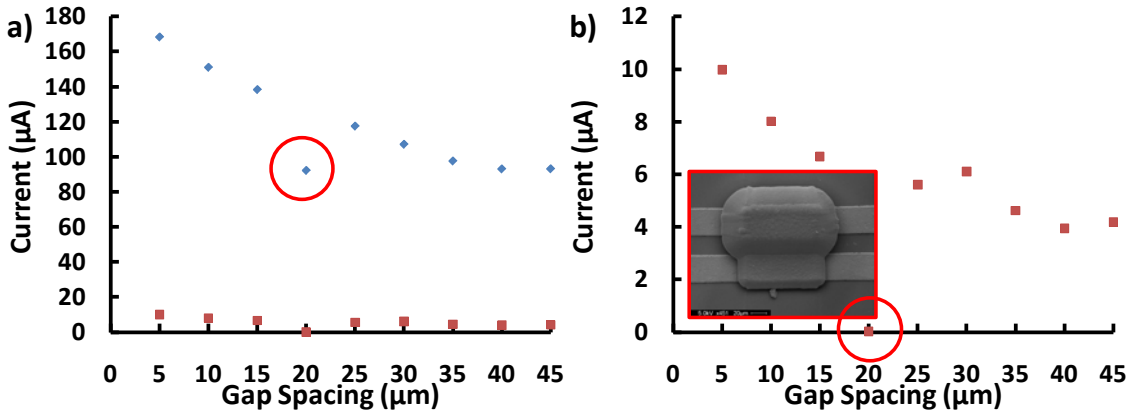

Figure 44: Trends generally seen with irregular junctions – a) The current in the oxidized (*blue diamonds*) and reduced state (*red squares*) of PPy(Li^+DBS^-) was measured at 10 mV in air for each set of bars where the 20 µm spacing deviates from the general trend. **b)** The reduced currents show the two orders of magnitude drop in current but for the 20 µm spacing the current measures as an extremely low current with the inset of an SEM of the junction.

The data of the oxidized current of PPy(DBS^-) is normalized by the largest current (smallest spacing) and the same trend of decreasing current with increasing gap spacing can be seen (Figure 45 *blue diamonds*). Assuming that ohmic behaviour dominates at low fields and assuming parallel plate geometry (1-dimensional), the current (Equation 3.5) should have a L^{-1} dependence. Based on Ohm`s law the calculated normalized currents expected for this trend deviates significantly from the initial normalized currents (Figure 45 *red line*). This is the first indication that system is less dependent upon electrode spacing than initially presumed and that there is another factor not being considered. The assumptions behind Ohm`s law do not hold, for example, as the

field drops linearly between the contacting electrodes it could possibly be related to spatial or directional homogeneity of the material.

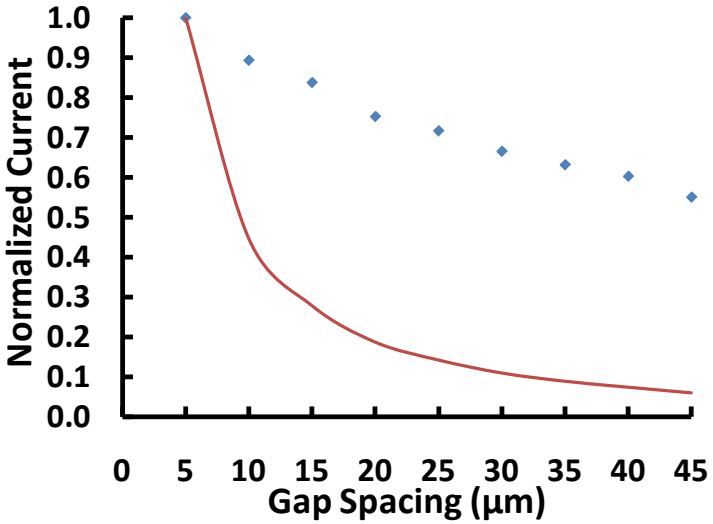

Figure 45: The normalized current of the oxidized polymer and normalized current for the expected ohmic behaviour – The current for the oxidized polymer PPy(DBS^-) measured at 10 mV is normalized to the largest current (smallest spacing) (*blue diamonds*). Based on ohms law one would expect a L^{-1} dependence and the calculated currents expected for this trend (*red line*). The expected dependence (*red line*) and the actual (*blue diamonds*) differ significantly and show that the system is less dependent on changes of electrode spacing.

3.2.1.1 Simulation at Low Fields

The polymer hybrid system being less dependent upon electrode spacing (*L)* than previously expected indicates that there could be some degree of anisotropy present within the system. There are several reports of anisotropic (a material which presents different values depending on the given direction) properties within PPy attributed to the growth conditions utilized for polymerization which is consistent with the similar

development of the system used within these studies.[99, 170-172] For the polymer hybrid of PPy(Li^+DBS^-), observations based on the different growth rates determined through profilometry measurements (Chapter 2 Section 2.2.2.1 Figure 18 and Figure 19) and SEM images indicate the anisotropic nature of the polymer (Figure 42 and Figure 43). To estimate the degree of anisotropy that exists in PPy(Li^+DBS^-), a computer simulation of a 2-D model was designed to reproduce the expected current as a function of the anisotropic nature following the experimental setup in Section 2.2.7.

The simulated currents were obtained and normalized to the largest current (smallest gap spacing of 5 µm) and various anisotropic conductivities were compared (Figure 46). The general trend of the simulation results indicate an increase in the conductivity parallel to the surface which suggests that there is a decreased dependence based on spacing. The increase in anisotropic conductivity from 2 to 200 results in a progressively decreasing dependence based on electrode spacing. The conductivity becomes less dependent when it is increased from 100 to 200 as there are only slight changes within the currents produced.

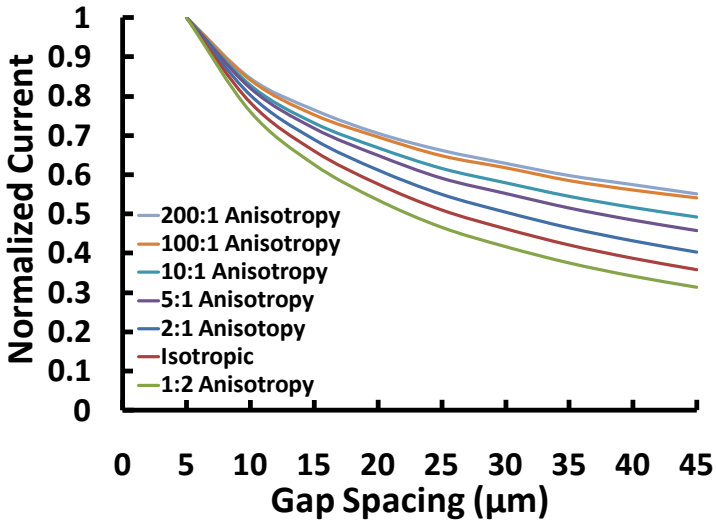

Figure 46: Simulation data obtained from various length:height anisotropic conductivity – The current is normalized by the largest current (smallest spacing) to compare and contrast the differences between the data sets. The geometry chosen was a Au electrode with a width of 50 µm, a height of 1.5 µm and 0.1 V applied potential to the polymer material on top with a thickness of 20 µm, and a width of 100 µm. As the anisotropy of the system increases up to 200 fold from an isotropic system in the x dimension the curvature decreases.

The currents generated by an isotropic system did not follow any of the previous experimental data of the oxidized currents at 10 mV. Also, the dependence based on the L^{-1} from Ohm`s law did not follow the trend of an isotropic polymer system. The simulated system was set up in 2-D, which makes the design completely square and symmetric to save on computational time (Chapter 2 Section 2.2.7). The actual polymer system varies in geometry with the edges rounded off creating a "V" at the middle of the polymer (Figure 18). Determined from the DC measurements in Figure 21, once the gap has been bridged the contribution from the rest of the polymer is less significant and is also consistent with the anisotropic growth conditions. Adding rounded edges

and a “V” at the center to the actual shape of the polymer system would correlate experimental data more closely but would not account for the large deviation without altering the anisotropy of the system.

An anisotropic system above 50:1 provides a more reasonable match to the experimental data of the oxidized polymer rather than a completely isotropic system. Comparing the different anisotropic conductivities, the ratio that was chosen to best correlate the experimental data was the 100:1 conductivity (Figure 47). Adjusting the normalized oxidized current, the 100:1 anisotropic conductivity fits within experimental uncertainty. The molecular anisotropy, which in turn impacts conductivity, can be related to the anisotropy of the oxidized polymer PPy(DBS^-). This suggests that the hemi-micelle’s formed by the surfactant DBS^- can direct the molecular orientation to produce different directional conductivity.[109] The electrochemical growth rate for PPy(DBS^-) has been determined to be about a 2:1 ratio in width to height (Figure 18) which can also correlate the anisotropic behaviour determined from the simulation measurements.

During the polymerization process, the use of DBS^- (a common surfactant) as the counterion can result in hemi-micelle formation and therefore direct the orientation of polymerization within hydrophobic regions and interfaces.[109] This would support the directional polymerization and the anisotropic nature of conductivity that occurs within PPy(DBS^-). Increased anisotropy within PPy systems have been reported for high dopant to monomer molar ratios in the polymerization electrolyte [171] and mechanical stretching

[173, 174] which also occurs with PPy(Li^+DBS^-). For polymer systems seen to increase in molecular anisotropy, it is typically due to an increase in conjugation length which results in an increased electrical conductivity.[141]

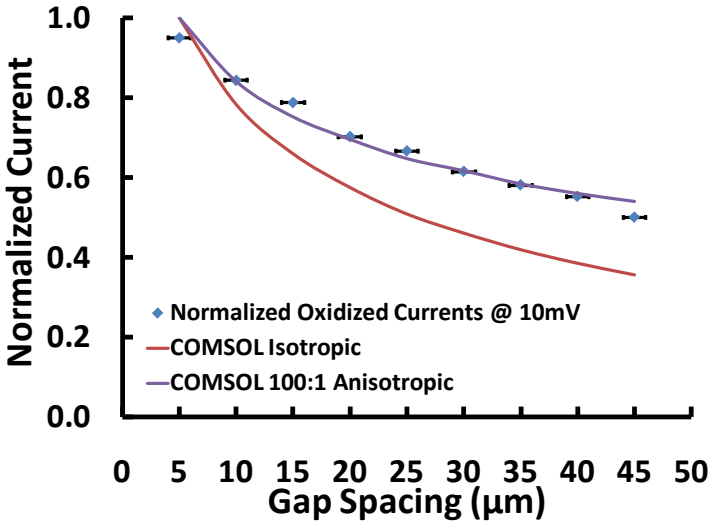

Figure 47: The normalized current of the oxidized polymer compared to the simulation data of an isotropic and 100:1 anisotropic system – When comparing the simulation data with the normalized experimental data the trend closely follows an anisotropic 100:1 system and deviates greatly from an isotropic system. The error bars of the experimental data are the deviations within the electrode spacing during the fabrication process (Figure 28).

3.2.2 Gap Spacing at High Fields

The field dependence of the fully reduced polymer of PPy(Li^+DBS^-) in the dry state has been examined. Using a 2 electrode setup using a CHI-760C workstation the junction was scanned from 0 to 2 V at a rate of 5 $mV \cdot s^{-1}$ to obtain the non linear behaviour of the polymer hybrid (Figure 48). The *I-V* measurement of PPy(Li^+DBS^-) on a 5 µm junction can be seen to deviate from linearity compared to the control polymer systems that do not

contain mobile ions, such as PPy(DBS^-) and PPy (Figure 48a). For the polymer in the oxidized state of PPy(DBS^-), the potential could only be scanned up to 100 mV due to irreversible fluctuations in current that occur above 100 mV. PPy in the absence of ions was not chosen for further experimentation due to the irregular *I-V* data in which there was no trend seen when measuring the current from the small to large gap spacings. The irregular currents for each spacing are likely due to the extremely rough morphology, with many nodular growths throughout the film leading to poor contact with the Au electrodes (Figure 49). From Figure 49 the similar lateral growth of the polymer without surfactant DBS^- suggests that surface interactions are the main cause of growth and not simply from hemi-micelle formation. The polymer hybrid of PPy(Li^+DBS^-) is shown to exhibits all 3 conduction regions of ohmic (Section 3.1.2), SCLC (Section 3.1.3), and FGCC (Section 3.1.4) and will be examined further within the subsequent figures.

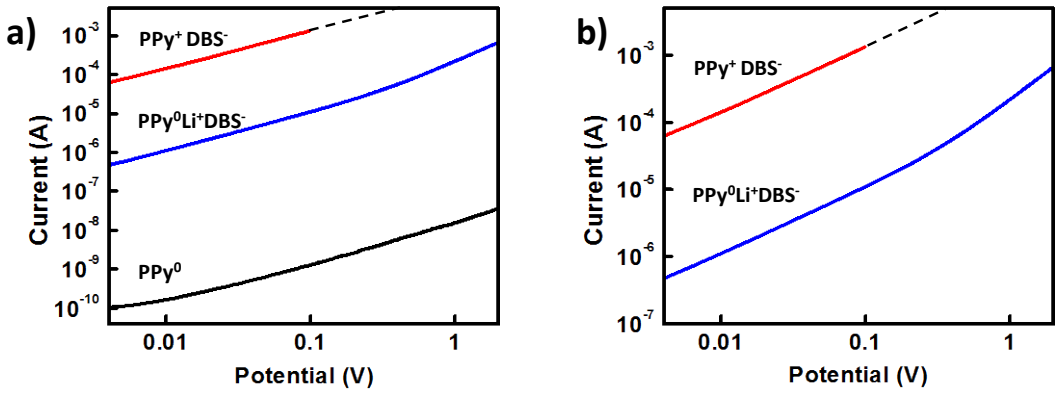

Figure 48: *I-V* behaviour of various polymers on a 5 µm gap spacing – a) A log current versus log potential plot of a 5 µm gap spacing with the various polymers *PPy(Li^+DBS^-)*, *PPy(DBS^-)*, and *PPy* deposited. **b)** A close up of the polymer with the inserted ions.

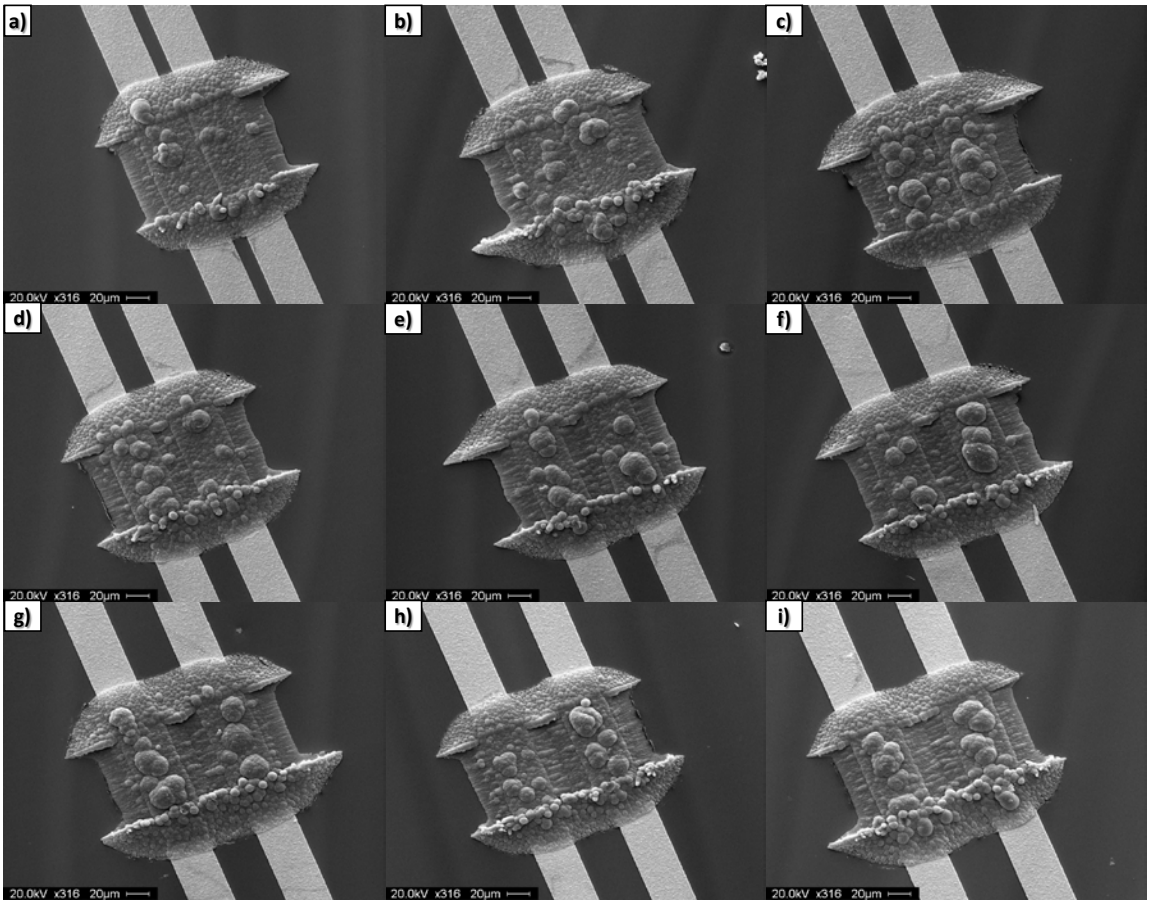

Figure 49: SEM images of the PPy without ions – PPy deposited to a calculated thickness of 25 µm on all gap spacings of **a)** 5 µm **b)** 10 µm **c)** 15 µm **d)** 20 µm **e)** 25 µm **f)** 30 µm **g)** 35 µm **h)** 40 µm and **i)** 45 µm

Of the various conduction components present within PPy(Li^+DBS^-), the ohmic component dominates at low fields. As the field continues to increase, SCLC then begins to be the main conduction component within PPy(Li^+DBS^-). The different conduction components can be separated by extrapolating out the ohmic component at low fields from the overall *I-V* measurement dominated by SCLC and FGCC. This was done with PPy(Li^+DBS^-) for a 5 µm gap spacing, as the ohmic component was extracted from the *I-V*

curve and plotted in comparison to the FGCC (Figure 50). To investigate the scaling behaviour, the ohmic region was subtracted from the FGCC for each gap spacing. The difference of the ohmic contribution into the high field region of the FGCC can then be plotted as a log *I* log *L* plot. Based on Equation 3.9 for SCLC, a slope of *-3* (*red line*) is expected, although from the experimental data the slope is closer to *-1* (*black line*) (Figure 51). The experimental current from a crossbar junction (~500 nm) was added and lies near the projected slope of the experimental data at 2 V (*black line*). Projecting the experimental slope of *-1* down to a 10 nm spacing gives predicted currents of ~20 mA. Presuming that the dimensions of the contact electrodes are reduced from 100 µm (utilized for the parallel bar geometry) to 100 nm (i.e. 10 x 10 nm crossbar junction) the current should be ~2 µA. The predicted currents retrieved from the experimental data of a slope of *-1* deviate from the presumed *-3* slope (Equation 3.13) but give a reasonable estimate as to what the currents should be for nm sized devices.

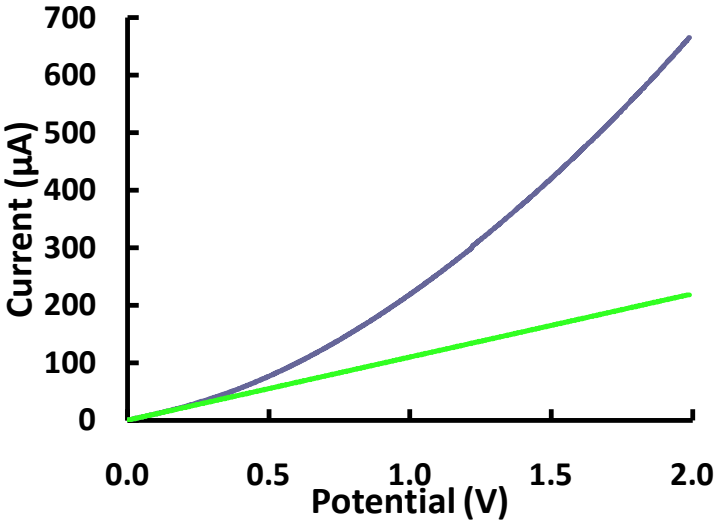

Figure 50: A 5 µm gap spacing where the ohmic component is separated from the *I-V* measurement – When a junction of the polymer hybrid of PPy(Li^+DBS^-) is setup in a 2 electrode configuration to measure the *I-V* behaviour the system proceeds through 3 different conduction regions (*blue line*). The contribution of the ohmic component was separated from the SCLC and FGCC (*green line*).

The experimental data indicates that the dependence based on spacing is much less than expected, which would be consistent with the electric field dropping close to the contacting electrodes as opposed to evenly throughout the material as assumed by Ohm`s law. Seen in the low field ohmic region, the system of PPy(Li^+DBS^-) is less sensitive to changes in *L* (the distance between two electrodes). Consequently 3-D simulation models were created to better visualize the fields throughout the polymer which cannot be completely seen utilizing the 2-D half model.

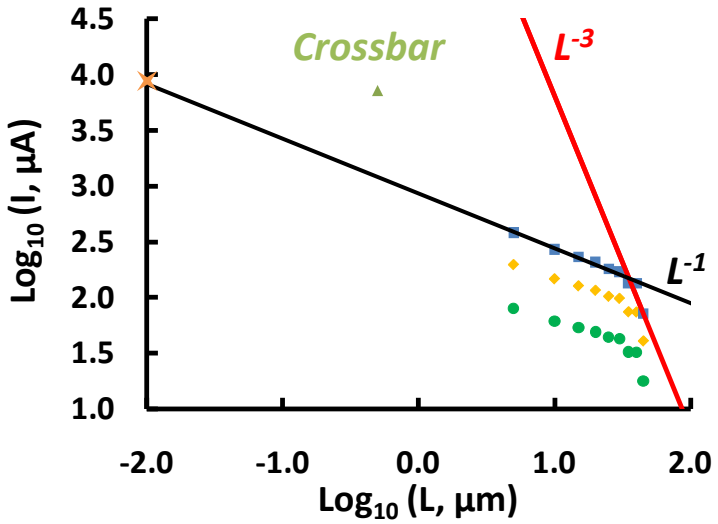

Figure 51: The current difference of the FGCC component separated from the ohmic component of Figure 50 for each gap spacing – Based on the SCLC equation the log *I* versus the log *L* should have an associated slope of *-3* (*red line*). When the different potentials (*0.5 V*, *1.0 V*, and *2.0 V*) are plotted for each gap spacing there is a general trend of increased slope. The slope at 2 V (*black line*) is extended past the crossbar junction (~500 nm *green triangle*) and extended down to 10 nm (*orange star*).

3.2.2.1 Simulation at High Fields

Further simulation using a 3-D model (Section 2.2.7) brought perspective to how the electric fields might drop within the polymer hybrid of PPy(Li^+DBS^-). By correlating several factors such as polymer conductivity and anisotropic conductivity of 100:1 (between:perpendicular to the electrode surface) a 3-D model was generated. The potential at the base of the polymer was examined for each gap spacing where the potential beginning at the 2 V electrode uniformly drops to the ground electrode (Figure 52). A plot for each gap spacing indicates that the center of the junction initially starts off at 1 V but slowly increases with increasing gap spacing. The shift in potential may be due to the meshing parameters while building the 3-D model or the equations utilized

within COMSOL to determine the conductive media. A more refined mesh could be used to create a smoother image or different equations utilized but the use of a more powerful computer to run the calculations would be required.

A comparison of the potential at the base of the polymer of a 20 µm gap spacing was also done using the anisotropic 100:1 (*blue line*) and isotropic conductivity (*red line*) (Figure 53a). While there are slight differences in the potential throughout the 20 µm junction with the anisotropic conductivities the more noticeable difference is when the potential is measured at the top of the polymer (Figure 53b). The normalized potential drop (normalized with respect to the highest potential) within the junction is still prominent with an isotropic system although for the anisotropic conductivity of 100:1 there is a very small potential drop along the surface. This correlates to the experimental data as the potential drop is near the electrodes and not throughout the entire polymer.

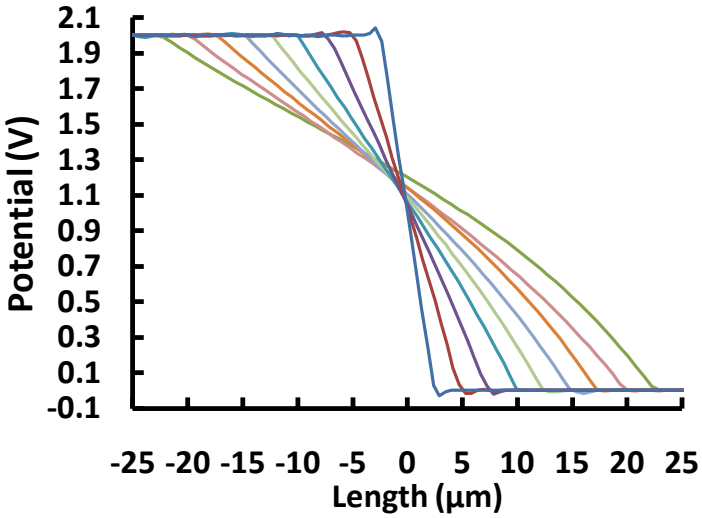

Figure 52: Simulation of the electric potential throughout the junction of the various gap spacings – As the gap spacing increases the potential drops close to linearity from the 2 V to the ground electrode.

A comparison of the 20 µm gap spacing was also done in order to correlate experimental data previously obtained using IDAs with PPy(Li^+DBS^-) ~6 µm thick (Figure 53b *green line*). The normalized data compares with the experimental anisotropic data where there is a small potential drop between the electrodes which again suggests that most of the potential drop is near the electrodes.

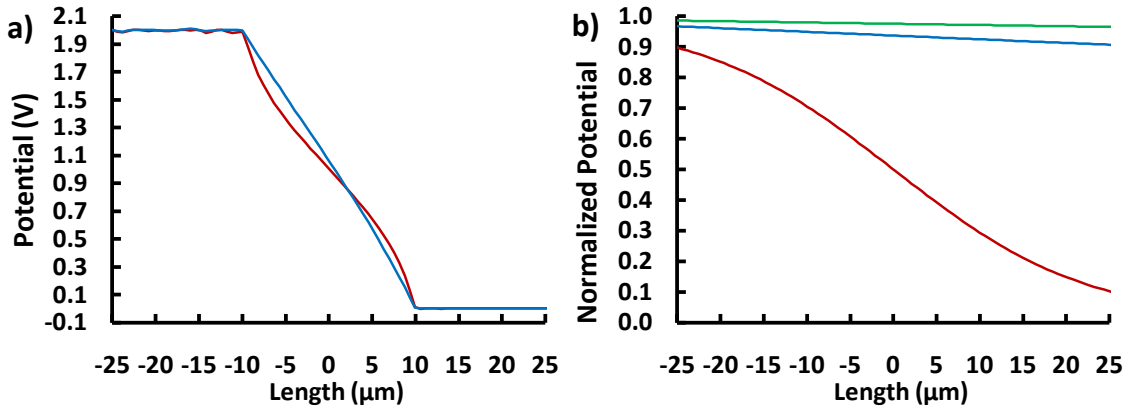

Figure 53: The potential through the polymer of a 20 µm wide junction – a) A comparison of the potential at the base of the polymer of an isotropic (*red line*) and anisotropic 100:1 (*blue line*) conductivity. **b)** A comparison of the simulated potential at the top of the polymer of an isotropic (*red line*), and anisotropic 100:1 (*blue line*) conductivity with the experimental potential measurement of an IDA electrode (*green line*).

The response at high fields of the polymer hybrid PPy(Li^+DBS^-) can be illustrated by viewing the normalized electric fields. The images were generated for a 5 to 45 µm gap spacing for an anisotropic (Figure 54a) and isotropic (Figure 54b) 100:1 conductivity. The jagged lines in the images of the electric field are due to the meshing parameters utilized when building the model. Similar to the potential plot, the images could be further refined but require greater meshing to create a smoother image possible with increased computing power.

The normalized field was chosen as an illustrative view to compare the electric fields within PPy(Li^+DBS^-), as the extrapolation and interpretation of data was done utilizing the field in the x-plane. With the electric field of all the gap spacings overlaid for an anisotropic conductivity, the field decreases as the spacing increases and remains higher

near the electrodes (Figure 54a). Contrary to this, the electric field of an isotropic conductivity is maintained throughout the electrode junction indicating a uniform colour in the image (Figure 54b).

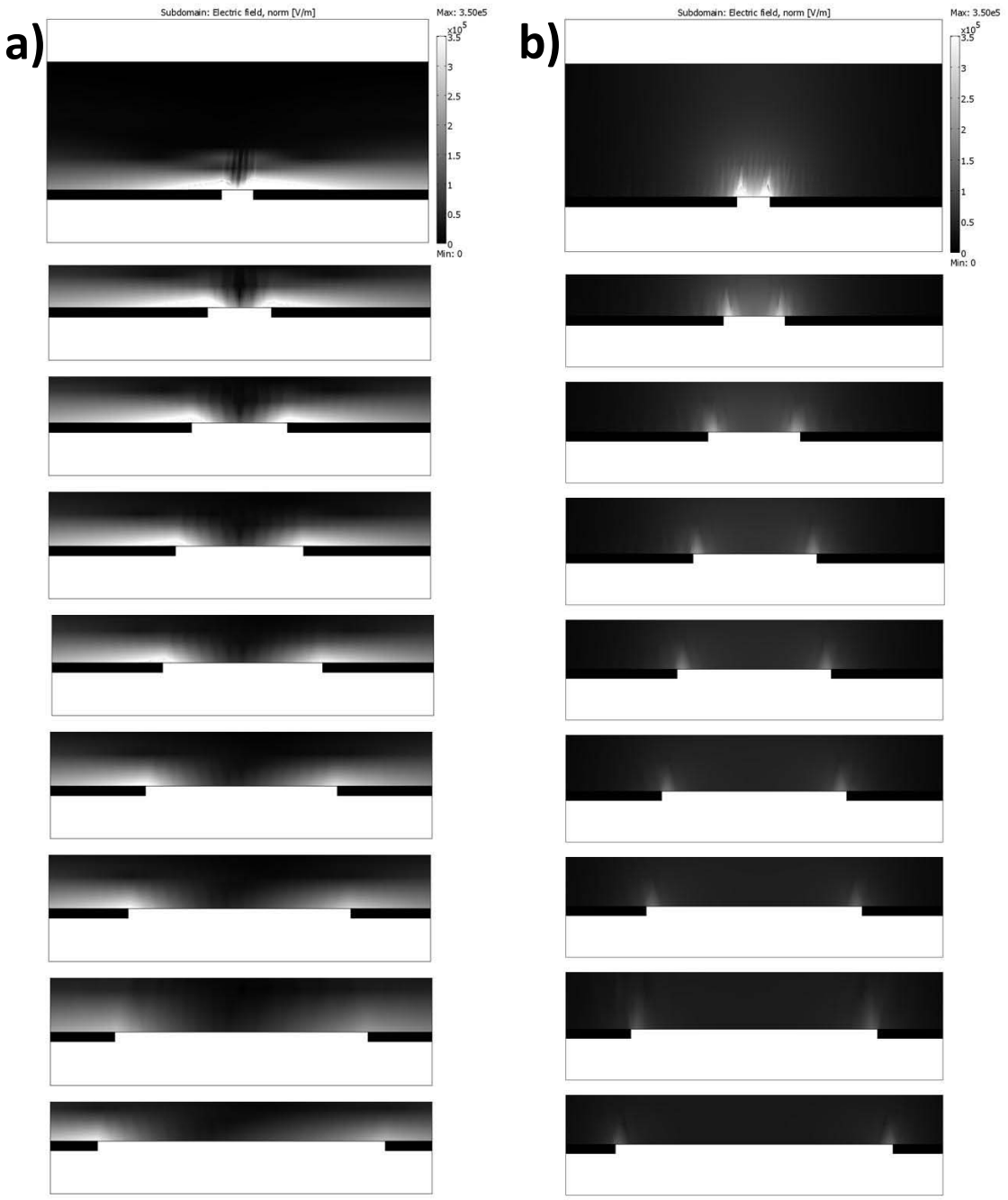

Figure 54: Simulation of the normalized electric fields – a) An anisotropic 100:1 conductivity with the overlaid gap spacings indicating that the field decreases as the spacing increases and that the field drops near the contacting electrodes. **b)** An isotropic conductivity with the overlaid gap spacings indicating that the field decreases as the spacing increases but is maintained with the junction.

A comparison of the maximum electric field (x-plane or parallel to the electrode surface) generated within the polymer of an anisotropic (*red line*) and isotropic (*blue line*) conductivity was done (Figure 55). The field of the anisotropic conductivity is lower than the isotropic conductivity but both follow a similar trend where the electric field drops off quickly from the 5 to 10 µm spacing. Since the field for anisotropic conductivity is not maintained throughout the polymer, the system becomes less dependent upon the electrode spacing of *L*. With the fields localized around the electrodes only a portion of the Li^+ can drift within the polymer hybrid thereby rendering a large portion of the polymer in either the ohmic or SCLC regions.

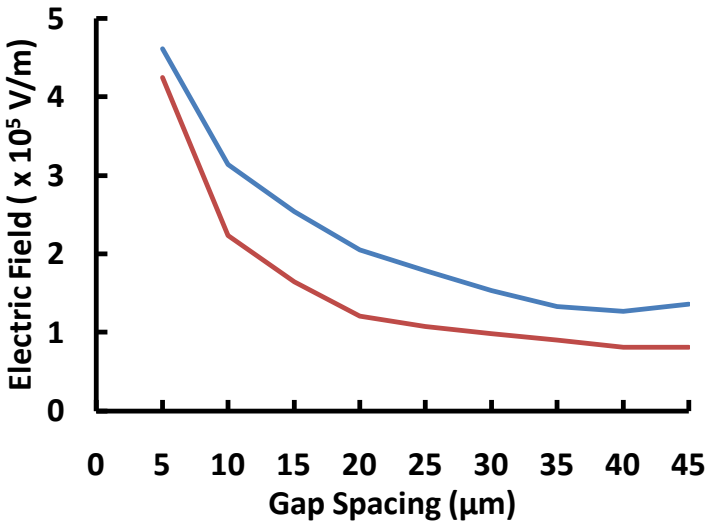

Figure 55: A comparison of the maximum electric field (x-plane) generated with the polymer of an anisotropic and isotropic conductivity – The maximum electric field of the isotropic conductivity (*blue line*) is higher than the anisotropic conductivity (*red line*).

3.2.3 Temperature

By examining the temperature dependence of conductivity from various conducting polymers in conjunction with the scaling parameters, the conduction mechanism utilized can be better understood. As well, by analyzing the conductivity of the polymers through a range of temperatures the stability can be established.[175] With the polymers of PPy(Li^+DBS^-) and PPy(DBS^-) placed in the temperature vessel (Figure 29), *I-V* measurements up to 2 V (PPy(Li^+DBS^-)) and 100 mV (PPy(DBS^-)) were conducted at temperatures of ~268, 283, 298, and 313 K (Figure 56 and Figure 57). The general trend of the current measured with increasing temperature for the polymer hybrid of PPy(Li^+DBS^-) is seen to similarly increase. The rise in current can be attributed to lattice vibrations (i.e. chain motion) resulting in intra and inter chain hopping of the charge carriers due to the increase in temperature.[176]

To further determine what conduction mechanism is governing the increase in current with temperature, an Arrhenius plot was created by plotting the average current at 2 V for PPy(Li^+DBS^-) at each temperature. The linearity of Figure 56b from the polymer hybrid of PPy(Li^+DBS^-) indicates that throughout these temperatures, it should exhibit Arrhenius behaviour. The activation energy *(E_a)* of the system is defined by the Arrhenius equation of

$$E_a = -RT\ ln\ \frac{k}{A} \tag{3.15}$$

where R is the universal gas constant (8.31451 J·(K·mol)$^{-1}$), k is the rate constant, T is the temperature (Kelvin) and A is the pre-exponential factor.

$$lnk = lnA - \frac{E_a}{RT} \tag{3.16}$$

A log log plot of the Arrhenius equation will result in a slope that is proportional to the E_a (Equation 3.17). The E_a measured for PPy(Li^+DBS^-) is 2.21 x 10^{-23} J or 0.14 meV which is several orders of magnitude lower than a previous reported system of polyethylene oxide (PEO) which has an E_a ranging from 0.2 to 1.0 eV.[177] The E_a for PEO was determined to be non-Arrhenius and associated with hole mobility within the polymer. The experimental E_a of PPy(Li^+DBS^-) is several orders of magnitude lower as these are measurements based on the movement of ions and not hole mobility which is typically reported.[155]

An E_a can also be determined from the experimental data of the polymer PPy(DBS^-) without mobile ions incorporated (Figure 57). The E_a calculated for this system is 8.03 x 10^{-24} J or 50.1 µeV. The experimental E_a determined for PPy(DBS^-) without mobile ions is several orders lower than the reported PEO E_a which can be attributed to the hole mobility that occurs within the system. In this case the system may be more rigid to decrease any chain motion that would occur to allow for intra and inter chain hopping of holes.[176]

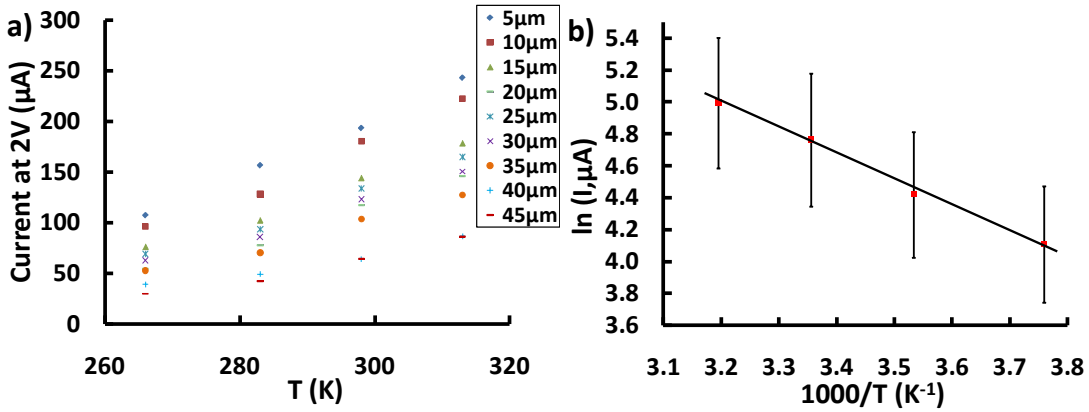

Figure 56: The current of PPy(Li^+DBS^-) measured at 2 V for each gap spacing under various temperature conditions – a) The current for each gap spacing of PPy(Li^+DBS^-) at the various temperatures is seen to increase as the temperature increases. **b)** An Arrhenius plot of the average current for all the gap spacings with the error bars indicating the standard deviation.

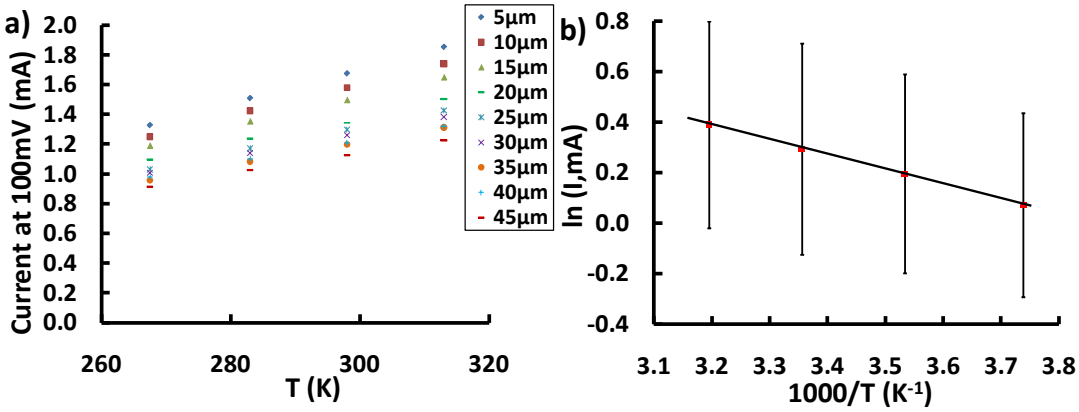

Figure 57: The current of PPy(DBS^-) measured at 2 V for each gap spacing under various temperature conditions – a) The current for each gap spacing of PPy(DBS^-) at the various temperatures is seen to increase as the temperature increases. **b)** An Arrhenius plot of the average current for all the gap spacings with the error bars indicating the standard deviation.

3.3 Scaling Properties of the Temporal Response as a Function of:

3.3.1 Gap Spacing

The double potential step experiment (Figure 58a) applies an initial 2.5 V positive potential until a steady state current is reached. Once the current has reached steady state the electric field is then reversed to an intermediate negative potential of -2 V. A large positive potential can be used to induce ionic drift within the polymer hybrid while the negative intermediate potential will cause the reversal of the field to exhibit a unique electronic response which is associated with ionic drift. Based on the discussion in Section 3.1.5, the transient behaviour is expected to be field dependent and hence dependant on *L* (Figure 58b). In order to explore that possibility, the transient behaviour (in this case the initial slope in the forward scan) was measured as a function of gap spacing. As expected, the initial slope (in the first couple milliseconds) shows a general trend of a faster rate of change as the gap spacing decreases (Figure 59a). When the slopes are compared to the maximum electric fields both the isotropic (*red squares*) and anisotropic 100:1 (*blue diamonds*) an increasing trend is seen with slight deviations (Figure 59b). The anisotropic conductivity strongly correlates several data points for the simulated electric fields with the experimental slope (*blue line*). This is an indication that the anisotropic system is well behaved as a function of the electric field within the polymer hybrid system of PPy(Li^+DBS^-). For the isotropic electric fields (*red line*), the deviation is much greater, suggesting that the system does not follow an

isotropic conductivity; which was previously established correlating low and high field experimental data but further corroborates anisotropy within PPy(Li^+DBS^-).

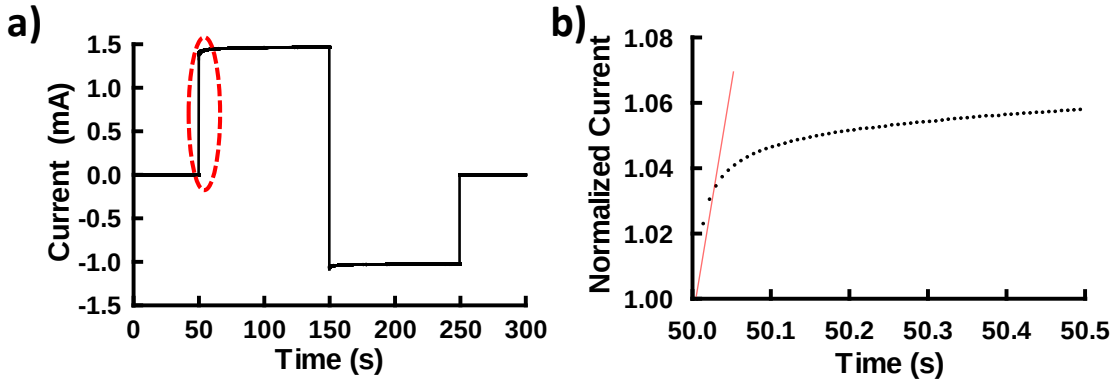

Figure 58: Potential step data extrapolation of a 5 µm gap spacing of PPy(Li^+DBS^-) – a) A potential step experiment on a 5 µm gap stepping from 0 V to a high positive potential of 2.5 V then immediately to a intermediate negative potential of -2 V. **b)** The highlighted graph is the first couple seconds after the SCLC is established where the red line is used to determine the initial slope for all the gap spacings during a potential step experiment.

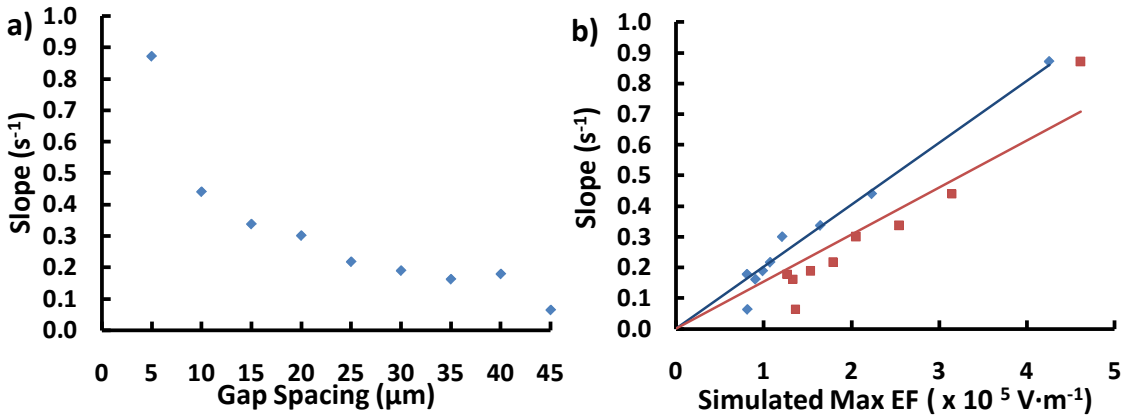

Figure 59: Potential step data analysis for all gap spacings of PPy(Li^+DBS^-) – a) The slope was extracted from the potential step experiment of PPy(Li^+DBS^-) where the rate at which it takes to reach steady state increases with decreasing gap spacing. **b)** When the slopes are compared to the maximum electric fields (EF) both the isotropic (*red squares*) and anisotropic 100:1 (*blue diamonds*) conductivity show an increasing trend with slight deviations.

3.3.2 Temperature

Similar to Section 3.2.3, the temperature dependence has been examined as a function of temporal behaviour and gap spacing. Analyzing the potential step experiments, the data indicates a consistent pattern among the various gap spacings although this does not match well with the expected behaviour (Figure 60a). To adjust for these fluctuations, the normalized slopes for all spacings were averaged at each temperature and plotted as an Arrhenius plot (similar to the current at 2 V), the linearity seen here again defines that the system should follow Arrhenius behaviour (Figure 60b). The calculated E_a for the system is 1.65 x 10^{-23} J or 0.11 meV which is similar to the energies obtained from *I-V* measurements. The low E_a can be attributed to changes in hole mobility that occur within the system due to chain motion resulting in an increase in intra and inter chain hopping.[176]

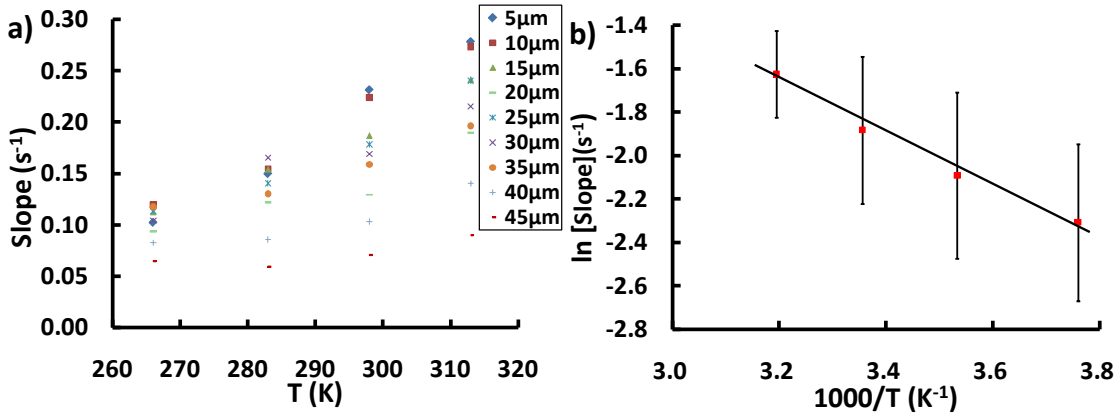

Figure 60: The slope of PPy(Li^+DBS^-) potential step experiment for each gap spacing under various temperatures – a) The normalized slope of the double potential step experiment was taken for each gap spacing at the various temperatures. **b)** An Arrhenius plot of an average of all the points in **a)** and the standard deviation of the slope among the various gap spacings.

3.4 Summary and Conclusions

A conducting polymer hybrid system, PPy(Li^+DBS^-), has been shown to exhibit novel time and potential dependent conductivity that can be utilized to create a dynamic memory device.[28] The system has been theorized to have excellent scaling properties allowing memory devices to be operated down to the nm scale which has been solidified by previous studies.[71] The polymer hybrid of PPy(Li^+DBS^-) was successfully deposited on a fabricated device of Au parallel bars which allowed for the systematic analysis of the potential and time dependent characteristics of the system.

PPy(Li^+DBS^-) was electrochemically grown on Au electrodes following the previously reported growth rate of 200 $mC \cdot cm^{-1}$ for every micrometer. The observed polymer growth on Au parallel bars occurs at a rate 2:1 in the horizontal to vertical directions. The polymer thickness as measured from profilometry differed when calculating from previously reported values of thickness and therefore had to be calibrated for our own electrode geometry. The current change in polymer thickness was also determined to be minute once the junction had been bridged, as measured through the DC. This was consistent with the field distribution observed within the simulations, where most of the field drops at the film electrode interface.

The current flow within PPy(Li^+DBS^-) structures does not scale with electrode spacing by the expected L^{-1} behaviour from the ohmic dependence. The current is seen to decrease much more slowly with increasing spacing than would be expected for

isotropic ohmic materials and anisotropic conductivity is a possible explanation for the deviation in currents seen with scaling. Simulations show that the degree of anisotropy can explain the variation of current with gap spacing. For an anisotropic conductivity of 100:1, computer simulations can correlate to the experimental results within a given uncertainty.

When comparing the experimental data to the L^{-3} dependence of conductivity within the FGCC region, a greater deviation is present indicating a dependence of L^{-1}. The experimental data suggested that there was a significant potential drop vertically but not horizontally. Through simulation modeling, the potential and electric field is seen to significantly drop near the contacting electrodes. The computer simulations were able to properly correlate the behaviour seen within the FGCC experimental data.

Temperature dependent measurements established that the current increase for the polymer hybrid within the FGCC region from the *I-V* and potential step experiments for all the gap spacings display Arrhenius behaviour. The deviation in the experimental E_a from reported literature values can be explained by ion motion within our system and not an increase in hole mobility.

Based on these studies, for devices with electrode dimensions of 10 x 10 nm, the currents are expected within a range from 1 to 10 μA. The expected currents deviate from the proposed conduction mechanisms but demonstrate important aspects to understanding devices with nm scale dimensions. The scaling properties and

conduction mechanisms for field induced ion mobility have been clarified within this thesis; undetermined parameters such as ion mobility and permittivity not examined within this work are possible directions for future work.

References

(1) Waser, R., *Nanoelectronics and Information Technology: Advanced Electronic Materials and Novel Devices*. Wiley-VCH: **2003**; p 1002.

(2) Reilly, E. D., Concise Encyclopedia of Compter Science. In *Concise Encyclopedia of Compter Science*, Fourth ed.; Reilly, E. D., Ed. Wiley: **2004**; p 640.

(3) Shaw, M., Solid State Switching. In *Encyclopedia of Physics*, 2nd ed.; Lerner and Trigg ed.: **1991**; pp 1149-1154.

(4) Reilly, E. D., *Milestones in Computer Science and Information Technology*. Greenwood Press: Westport, Conn., **2003**; p 380.

(5) International Technology Roadmap for Semiconductors. http://www.itrs.net/.

(6) Dennard, R. H.; Gaenssle.Fh; Yu, H. N.; Rideout, V. L.; Bassous, E.; Leblanc, A. R., Design of Ion-Implanted Mosfets with Very Small Physicsal Dimensions. *IEEE J. Solid-State Circuit* **1974,** *SC 9* (5), 256-268.

(7) Isaac, R., The Remarkable Story of the Dram Industry. *Solid-State Circuits Newsletter, IEEE* **2008,** *13* (1), 45-49.

(8) Frank, D. J.; Dennard, R. H.; Nowak, E.; Solomon, P. M.; Taur, Y.; Wong, H. S. P., Device Scaling Limits of Si Mosfets and Their Application Dependencies. *Proc. IEEE* **2001,** *89* (3), 259-288.

(9) Lilienfeld, J. E. Device for Rectifying or Detecting Electric Current. 1900018, **1933**.

(10) Lilienfeld, J. E. Electrolytic Condenser. 2013564, **1935**.

(11) Shockley, W. Semiconductor Amplifier. April 4, **1950**.

(12) Kahng, D. a. A., M. M. In *Silicon-Silicon Dioxide Field Induced Surface Devices*, IRE-AIEE Solid State Device Research Conference, Pittsburgh, Pa, Pittsburgh, Pa, **1960**.

(13) Moore, G. E., Cramming More Componenets onto Integrated Circuits. *Proc. IEEE* **1965,** *86* (1), 82-85.

(14) Vogel, E., Technology and Metrology of New Electronic Materials and Devices. *Nat. Nanotechnol.* **2007,** *2* (1), 25-32.

(15) Robinson, A. L., Problems with Ultraminiaturized Transistors. *Science* **1980,** *208* (4449), 1246-1249.

(16) Robinson, A. L., One Billion Transistors on a Chip: The Annual Rate of Increase in Numbers of Transistors on a Chip Is Slowing as Theoretical Limits Are Neared, but There May Be a Billion by the Year 2000. *Science* **1984,** *223* (4633), 267-268.

(17) Robinson, A. L., Transistors Head for the Trenches: Space on the Surface of a Random Access Memory Chip Is Limited; Vertical Transistors on Trench Walls Permit Denser Packing. *Science* **1986,** *231* (4735), 217-218.

(18) Davari, B.; Dennard, R. H.; Shahidi, G. G., Cmos Scaling for High-Performance and Low-Power - the Next 10 Years. *Proc. IEEE* **1995,** *83* (4), 595-606.

(19) Doyle, B., Transistor Elements for 30nm Physical Gate Lengths and Beyond. *Intel Technology Journal* **2002,** *6* (2), 42-54.

(20) Mandelman, J. A.; Dennard, R. H.; Bronner, G. B.; DeBrosse, J. K.; Divakaruni, R.; Li, Y.; Radens, C. J., Challenges and Future Directions for the Scaling of Dynamic Random-Access Memory (Dram). *IBM J. Res. Dev.* **2002,** *46* (2-3), 187-212.

(21) Moore, G. E., No Exponential Is Forever: But "Forever" Can Be Delayed! *IEEE International Solid State Circuits Conference* **2003,** *1*, 1-19.

(22) Muller, D. A., A Sound Barrier for Silicon? *Nat. Mater.* **2005,** *4* (9), 645-647.

(23) Thompson, S. E.; Chau, R. S.; Ghani, T.; Mistry, K.; Tyagi, S.; Bohr, M. T., In Search Of "Forever," Continued Transistor Scaling One New Material at a Time. *IEEE Trans. Semicond. Manuf.* **2005,** *18* (1), 26-36.
(24) Dennard, B.; Wagner, K., Discussing Dram and Cmos Scaling with Inventor Bob Dennard. *IEEE Des. Test Comput.* **2008,** *25* (2), 188-191.
(25) Song, S. C.; Zhang, Z.; Huffman, C.; Bae, S. H.; Sim, J. H.; Kirsch, P.; Majhi, P.; Moumen, N.; Lee, B. H., Integration Issues of High-K and Metal Gate into Conventional Cmos Technology. *Thin Solid Films* **2006,** *504* (1-2), 170-173.
(26) Kuekes, P. J.; Snider, G. S.; Williams, R. S., Crossbar Nanocomputers. *Sci.Am.* **2005,** *293* (5), 72.
(27) Wuttig, M.; Steimer, C., Phase Change Materials: From Material Science to Novel Storage Devices. *Appl. Phys. A-Mater. Sci. Process.* **2007,** *87* (3), 411-417.
(28) Pillai, R. G.; J. H. Zhao; M. S. Freund; D. J. Thomson, Field-Induced Carrier Generation in Conjugated Polymer Semiconductors for Dynamic, Asymmetric Junctions. *Adv. Mater.* **2008,** *20* (1), 49-53.
(29) Strukov, D. B.; Snider, G. S.; Stewart, D. R.; Williams, R. S., The Missing Memristor Found. *Nature* **2008,** *453* (7191), 80-83.
(30) Lai, S. In *Current Status of the Phase Change Memory and Its Future*, Electron Devices Meeting, **2003**. IEDM '03 Technical Digest. IEEE International, **2003**; pp 10.1.1-10.1.4.
(31) Williams, S., How We Found the Missing Memristor. *IEEE Spectr.* **2008,** *45* (12), 24-31.
(32) Ovshinsk.Sr, Reversible Electrical Switching Phenomena in Disordered Structures. *Physical Review Letters* **1968,** *21* (20), 1450.
(33) Gonzalez-Hernandez, J.; Chao, B. S.; Strand, D.; Ovshinsky, S. R.; Pawlik, D.; Gasiorowski, P., Crystallization Studies of Germanium-Antimony-Tellurium Optical Memory Materials. *Applied Physics Communications* **1992,** *11* (4), 557-81.
(34) Galatsis, K.; Wang, K.; Botros, Y.; Yang, Y.; Xie, Y. H.; Stoddart, J. F.; Kaner, R. B.; Ozkan, C.; Liu, J. L.; Ozkan, M.; Zhou, C. W.; Kim, K. W., Emerging Memory Devices - Nontraditional Possibilities Based on Nanomaterials and Nanostructures. *IEEE Circuits Devices* **2006,** *22* (3), 12-21.
(35) Hwang, Y. N.; Hong, J. S.; Lee, S. H.; Ahn, S. J.; Jeong, G. T.; Koh, G. H.; Oh, J. H.; Kim, H. J.; Jeong, W. C.; Lee, S. Y.; Park, J. H.; Ryoo, K. C.; Horii, H.; Ha, Y. H.; Yi, J. H.; Cho, W. Y.; Kim, Y. T.; Lee, K. H.; Joo, S. H.; Park, S. O.; Chung, U. I.; Jeong, H. S.; Kinam, K. In *Full Integration and Reliability Evaluation of Phase-Change Ram Based on 0.24 Um-Cmos Technologies*, VLSI Technology: Digest of Technical Papers, **2003**; pp 173-174.
(36) Samsung. http://www.samsung.com/us/index.html.
(37) Chua, L. O., Memristor - Missing Circuit Element. *IEEE Transactions on Circuit Theory* **1971,** *CT18* (5), 507-520.
(38) Chua, L. O., *Introduction to Nonlinear Network Theory*. McGraw-Hill: New York, **1969**; p 987.
(39) Wang, F. Y., Memristor and Memristive Switching Mechanism. *J. Nanophotonics* **2008,** *2*, 1-4.
(40) Yang, J. J.; Pickett, M. D.; Li, X. M.; Ohlberg, D. A. A.; Stewart, D. R.; Williams, R. S., Memristive Switching Mechanism for Metal/Oxide/Metal Nanodevices. *Nat. Nanotechnol.* **2008,** *3* (7), 429-433.
(41) Schroeder, R. C., Memristor Mechanics. *IEEE Spectr.* **2009,** *46* (2), 8-9.

(42) Yang, J. J.; Miao, F.; Pickett, M. D.; Ohlberg, D. A. A.; Stewart, D. R.; Lau, C. N.; StanleyWilliams, R., The Mechanism of Electroforming of Metal Oxide Memristive Switches. *Nanotechnology* **2009,** *20* (21), 1-9.

(43) Wu, J.; Mobley, K.; McCreery, R. L., Electronic Characteristics of Fluorene/Tio2 Molecular Heterojunctions. *Journal of Chemical Physics* **2007,** *126* (2), 024704-1-11.

(44) Argall, F., Switching Phenomena in Titanium Oxide Thin Films. *Solid-State Electron.* **1968,** *11* (5), 535.

(45) Bruyere, J. C.; Chakrave.Bk, Switching and Negative Resistance in Thin Films of Nickel Oxide. *Applied Physics Letters* **1970,** *16* (1), 40-44.

(46) Chopra, K. L., Avalanche-Induced Negative Resistance in Thin Oxide Films. *J. Appl. Phys.* **1965,** *36* (1), 184-188.

(47) Hiatt, W. R.; Hickmott, T. W., Bistable Switching in Niobium Oxide Diodes. *Applied Physics Letters* **1965,** *6* (6), 106109.

(48) Hickmott, T. W., Electroluminescence, Bistable Switching, and Dielectric Breakdown of Nb_2o_5 Diodes. *Journal of Vacuum Science & Technology* **1969,** *6* (5), 828.

(49) Beck, A.; Bednorz, J. G.; Gerber, C.; Rossel, C.; Widmer, D., Reproducible Switching Effect in Thin Oxide Films for Memory Applications. *Applied Physics Letters* **2000,** *77* (1), 139-141.

(50) Horowitz, G., Organic Field-Effect Transistors. *Adv. Mater.* **1998,** *10* (5), 365-377.

(51) Burroughes, J. H.; Jones, C. A.; Friend, R. H., New Semiconductor-Device Physics in Polymer Diodes and Transistors. *Nature* **1988,** *335* (6186), 137-141.

(52) Cheng, C. H.; Boettcher, S. W.; Johnston, D. H.; Lonergan, M. C., Unidirectional Current in a Polyacetylene Hetero-Ionic Junction. *J. Am. Chem. Soc.* **2004,** *126* (28), 8666-8667.

(53) Burroughes, J. H.; Bradley, D. D. C.; Brown, A. R.; Marks, R. N.; Mackay, K.; Friend, R. H.; Burns, P. L.; Holmes, A. B., Light-Emitting-Diode Based on Conjugated Polymers. *Nature* **1990,** *347* (6293), 539-541.

(54) Yang, Y.; Ouyang, J.; Ma, L. P.; Tseng, R. J. H.; Chu, C. W., Electrical Switching and Bistability in Organic/Polymeric Thin Films and Memory Devices. *Adv. Funct. Mater.* **2006,** *16* (8), 1001-1014.

(55) Ouyang, J. Y.; Chu, C. W.; Szmanda, C. R.; Ma, L. P.; Yang, Y., Programmable Polymer Thin Film and Non-Volatile Memory Device. *Nat. Mater.* **2004,** *3* (12), 918-922.

(56) Ouyang, J. Y.; Chu, C. W.; Tseng, R. J. H.; Prakash, A.; Yang, Y., Organic Memory Device Fabricated through Solution Processing. *Proc. IEEE* **2005,** *93* (7), 1287-1296.

(57) Bozano, L. D.; Kean, B. W.; Beinhoff, M.; Carter, K. R.; Rice, P. M.; Scott, J. C., Organic Materials and Thin-Film Structures for Cross-Point Memory Cells Based on Trapping in Metallic Nanoparticles. *Adv. Funct. Mater.* **2005,** *15* (12), 1933-1939.

(58) Chen, Q.; Zhao, L.; Li, C.; Shi, G. Q., Electrochemical Fabrication of a Memory Device Based on Conducting Polymer Nanocomposites. *J. Phys. Chem. C* **2007,** *111* (49), 18392-18396.

(59) Scott, J. C.; Bozano, L. D., Nonvolatile Memory Elements Based on Organic Materials. *Adv. Mater.* **2007,** *19* (11), 1452-1463.

(60) Ipe, B. I.; Thomas, K. G.; Barazzouk, S.; Hotchandani, S.; Kamat, P. V., Photoinduced Charge Separation in a Fluorophore-Gold Nanoassembly. *J. Phys. Chem. B* **2002,** *106* (1), 18-21.

(61) Okamoto, K.; Araki, Y.; Ito, O.; Fukuzumi, S., A Dramatic Elongation of the Lifetime of Charge-Separated State by Complexation with Yttrium Teiflate in Ferrocene - Anthraquinone Linked Dyad. *J. Am. Chem. Soc.* **2004,** *126* (1), 56-57.

(62) Peng, H. L.; Ran, C. B.; Yu, X. C.; Zhang, R.; Liu, Z. F., Scanning-Tunneling-Microscopy Based Thermochemical Hole Burning on a New Chrage-Transfer Complex and Its Potential for Data Storage. *Adv. Mater.* **2005,** *17* (4), 459-465.
(63) Kolliopoulou, S.; Dimitrakis, P.; Normand, P.; Zhang, H. L.; Cant, N.; Evans, S. D.; Paul, S.; Pearson, C.; Molloy, A.; Petty, M. C.; Tsoukalas, D., Hybrid Silicon-Organic Nanoparticle Memory Device. *J. Appl. Phys.* **2003,** *94* (8), 5234-5239.
(64) Schroeder, R.; Majewski, L. A.; Grell, M., All-Organic Permanent Memory Transistor Using an Amorphous, Spin-Cast Ferroelectric-Like Gate Insulator. *Adv. Mater.* **2004,** *16* (7), 633-637.
(65) Kozicki, M. N.; Park, M.; Mitkova, M. In *Nanoscale Memory Elements Based on Solid-State Electrolytes*, Ieee-Inst Electrical Electronics Engineers Inc: **2005**; pp 331-338.
(66) Hecker, K., White Paper " Oe-a Roadmap for Organic and Printed Electronics". *Organic Electronic Association* **2008**, 1-43.
(67) Hecker, K., White Paper " Oe-a Roadmap for Organic and Printed Electronics". *Organic Electronic Association* **2009**, 1-90.
(68) Acreo Ab. http://www.acreo.se/.
(69) Mennipos. http://menippos.de/en/company/.
(70) Thin Film Electronics. http://www.thinfilm.se/.
(71) Zhao, J. H.; Thomson, D. J.; Pillai, R. G.; Freund, M. S., Dynamic Resistive Crossbar Memory Based on Conjugated Polymer Composite. *Applied Physics Letters* **2009,** *94* (9), 092113-1-3.
(72) Shirakawa, H.; Louis, E. J.; Macdiarmid, A. G.; Chiang, C. K.; Heeger, A. J., Sythesis of Electrically Conducting Organic Polymers - Halogen Derivatives of Polyacetylene, (Ch)X. *J. Chem. Soc.-Chem. Commun.* **1977,** (16), 578-580.
(73) Freund, M. S.; Deore, B., *Self-Doped Conducting Polymers*. Wiley: Chichester, England ; Hoboken, NJ, **2007**; p 326.
(74) Wallace, G. G., *Conductive Electroactive Polymers: Intelligent Materials Systems*. Second ed.; CRC: **2002**; p 248.
(75) Bolto, B. A.; McNeill, R.; Weiss, D. E., Electronic Conduction in Polymers 3 Electronivc Properties of Polypyrrole. *Aust. J. Chem.* **1963,** *16* (6), 1090-1103.
(76) Bolto, B. A.; Weiss, D. E., Electronic Conduction in Polymers 2 Electrochemical Reduction of Polypyrrole at Controlled Potential. *Aust. J. Chem.* **1963,** *16* (6), 1076-1089.
(77) McNeill, R.; Weiss, D. E.; Wardlaw, J. H.; Siudak, R., Electronic Conduction in Polymers 1 Chemical Structure of Polypyrrole. *Aust. J. Chem.* **1963,** *16* (6), 1056-1075.
(78) Skotheim, T. A.; Reynolds, J. R., *Handbook of Conducting Polymers*. 3rd ed.; CRC: Boca Raton, Fla. ; London, **2007**; Vol. 1, p 1120.
(79) Asavapiriyanont, S.; Chandler, G. K.; Gunawardena, G. A.; Pletcher, D., The Electrodeposition of Polypyrrole Films from Aqueous-Solutions. *J. Electroanal. Chem.* **1984,** *177* (1-2), 229-244.
(80) Street, G. B., Characterization of Polypyrrole. *Abstr. Pap. Am. Chem. Soc.* **1983,** *186* (C3), 599-606.
(81) Smela, E., Microfabrication of Ppy Microactuators and Other Conjugated Polymer Devices. *J. Micromech. Microeng.* **1999,** *9* (1), 1-18.
(82) Segawa, H.; Shimidzu, T.; Honda, K., A Novel Photo-Sensitized Polymerization of Pyrrole. *J. Chem. Soc.-Chem. Commun.* **1989,** (2), 132-133.
(83) Aizawa, M. a. W., L., Enzyme-Catalyzed Oxidative Polymerization. In *Polymer Materials Encyclopedia*, First ed.; Salamone, J. C., Ed. CRC-Press: **1996**; Vol. 3, p 9600.

(84) Sadki, S.; Schottland, P.; Brodie, N.; Sabouraud, G., The Mechanisms of Pyrrole Electropolymerization. *Chem. Soc. Rev.* **2000,** *29* (5), 283-293.
(85) Genies, E. M.; Bidan, G.; Diaz, A. F., Spectroelectrochemical Study of Polypyrrole Films. *J. Electroanal. Chem.* **1983,** *149* (1-2), 101-113.
(86) Kim, K. J.; Song, H. S.; Kim, J. D.; Chon, J. K., Mechanism of Electropolymerization of Pyrrole in Acidic Aqueous-Solutions. *Bull. Korean Chem. Soc.* **1988,** *9* (4), 248-251.
(87) Qiu, Y. J.; Reynolds, J. R., Electrochemically Initiated Chain Polymerization of Pyrrole in Aqueous-Media. *J. Polym. Sci. Pol. Chem.* **1992,** *30* (7), 1315-1325.
(88) Waltman, R. J.; Bargon, J., Reactivity Structure Correlations for the Electropolymerization of Pyrrole - an Indo Cndo Study of the Reactive Sites of Oligomeric Radical Cations. *Tetrahedron* **1984,** *40* (20), 3963-3970.
(89) Waltman, R. J.; Bargon, J., Electrically Conducting Polymers - a Review of the Electropolymerization Reaction, of the Effects of Chemical-Structure on Polymer Film Properties, and of Application Towards Technology. *Can. J. Chem.-Rev. Can. Chim.* **1986,** *64* (1), 76-95.
(90) Andrieux, C. P.; Audebert, P.; Hapiot, P.; Saveant, J. M., Identification of the 1st Steps of the Electrochemical Polymerization of Pyrrole by Means of Fast Potential Step Techniques. *J. Phys. Chem.* **1991,** *95* (24), 10158-10164.
(91) Street, G. B.; Lindsey, S. E.; Nazzal, A. I.; Wynne, K. J., The Structure and Mechanical-Properties of Polypyrrole. *Molecular Crystals and Liquid Crystals* **1985,** *118* (1-4), 137-148.
(92) Naoi, K.; Lien, M. M.; Smyrl, W. H., Quartz Crystal Microbalance Analysis 1 Evidence of Anion or Cation Insertion into Electropolymerized Conducting Polymers. *J. Electroanal. Chem.* **1989,** *272* (1-2), 273-275.
(93) Pei, Q. B.; Inganas, O., Electrochemical Application of the Bending Beam Method 2 Electroshrinking and Slow Relaxation in Polypyrrole. *J. Phys. Chem.* **1993,** *97* (22), 6034-6041.
(94) Chiarelli, P.; Derossi, D.; Dellasanta, A.; Mazzoldi, A., Doping-Induced Volume Change in a Pi-Conjugated Conducting Polymer. *Polym. Gels Netw.* **1994,** *2* (3-4), 289-297.
(95) Gandhi, M. R.; Murray, P.; Spinks, G. M.; Wallace, G. G., Mechanism of Electromechanical Actuation in Polypyrrole. *Synthetic Metals* **1995,** *73* (3), 247-256.
(96) Matencio, T.; Depaoli, M. A.; Peres, R. C. D.; Torresi, R. M.; Detorresi, S. I. C., Ionic Exchanges in Dodecylbenzenesulfonate Doped Polypyrrole .1. Optical Beam Deflection Studies. *Synthetic Metals* **1995,** *72* (1), 59-64.
(97) Torresi, R. M.; Detorresi, S. I. C.; Matencio, T.; Depaoli, M. A., Ionic Exchanges in Dodecylbenzenesulfonate-Doped Polypyrrole .2. Electrochemical Quartz-Crystal Microbalance Study. *Synthetic Metals* **1995,** *72* (3), 283-287.
(98) Mitchell, G. R.; Davis, F. J.; Kiani, M. S., Influence of Synthesis on the Structure of Electrochemically Prepared Electrically Conducting Polymers. *British Polymer Journal* **1990,** *23* (1-2), 157-164.
(99) Pruneanu, S.; Graupner, W.; Oniciu, L.; Brie, M.; Turcu, R., Electrochemical and X-Ray Diffraction Studies on Polypyrrole Films. *Mater. Chem. Phys.* **1996,** *46* (1), 55-60.
(100) An, H.; Haga, Y.; Yuguchi, T.; Yosomiya, R., Synthesis of Polypyrrole by Electrochemical Polymerization Using Organic Anion Electrolytes and Its Application. *Angewandte Makromolekulare Chemie* **1994,** *218*, 137-151.
(101) Bard, A. J.; Faulkner, L. R., *Electrochemical Methods : Fundamentals and Applications*. 2nd ed.; Wiley: New York, **2001**; p 833.

(102) Bredas, J. L.; Scott, J. C.; Yakushi, K.; Street, G. B., Polarons and Bipolarons in Polypyrrole - Evolution of the Band-Structure and Optical-Spectrum Upon Doping. *Physical Review B* **1984,** *30* (2), 1023-1025.

(103) Bredas, J. L.; Themans, B.; Fripiat, J. G.; Andre, J. M.; Chance, R. R., Highly Conducting Polyprarphenylene, Polypyrrole, and Polythiophene Chains - an Abinitio Study of the Geometry and Electronic - Structure Modifications Upon Doping. *Physical Review B* **1984,** *29* (12), 6761-6773.

(104) Bredas, J. L.; Street, G. B., Polarons, Bipolarons, and Solitons in Conducting Polymers. *Accounts of Chemical Research* **1985,** *18* (10), 309-315.

(105) Wernet, W.; Wegner, G., Electrochemistry of Thin Polypyrrole Films. *Makromolekulare Chemie-Macromolecular Chemistry and Physics* **1987,** *188* (6), 1465-1475.

(106) Pernaut, J. M.; Peres, R. C. D.; Juliano, V. F.; Depaoli, M. A., Electrochemical Study of Polypyrrole Dodecyl-Sulfate. *J. Electroanal. Chem.* **1989,** *274* (1-2), 225-233.

(107) Zhong, C. J.; Doblhofer, K., Polypyrrole-Based Electrode Coatings Switchable Electrochemically between the Anion-Exchanger and Cation-Exchanger States. *Electrochimica Acta* **1990,** *35* (11-12), 1971-1976.

(108) Kelly, A. J.; Naoi, K.; Ohsaka, T.; Oyama, N., In-Situ Analysis of the Kinetic-Behavior of Ion-Transport in Electropolymerized Polypyrrole by Electrochemical Quartz Crystal Microbalance Method. *Bunseki Kagaku* **1991,** *40* (11), 835-841.

(109) Naoi, K.; Oura, Y.; Maeda, M.; Nakamura, S., Electrochemistry of Surfactant-Doped Polypyrrole Film (I) - Formation of Columnar Structure by Electropolymerization. *Journal of the Electrochemical Society* **1995,** *142* (2), 417-422.

(110) Smela, E.; Inganas, O.; Lundstrom, I., Controlled Folding of Micrometer-Size Structures. *Science* **1995,** *268* (5218), 1735-1738.

(111) Wang, X. Z.; Shapiro, B.; Smela, E., Development of a Model for Charge Transport in Conjugated Polymers. *J. Phys. Chem. C* **2009,** *113* (1), 382-401.

(112) Wang, X. Z.; Smela, E., Color and Volume Change in Ppy(Dbs). *J. Phys. Chem. C* **2009,** *113* (1), 359-368.

(113) Wang, X. Z.; Smela, E., Experimental Studies of Ion Transport in Ppy(Dbs). *J. Phys. Chem. C* **2009,** *113* (1), 369-381.

(114) Froeck, C.; Bartl, A.; Dunsch, L. In *Stm-Investigations and Afm-Investigations of One-Dimensional and Two-Dimensional Polypyrrole Structures on Electrodes*, Pergamon-Elsevier Science Ltd: **1995**; pp 1421-1425.

(115) Angelopoulos, M., Conducting Polymers in Microelectronics. *IBM J. Res. Dev.* **2001,** *45* (1), 57-75.

(116) Macinnes, D.; Druy, M. A.; Nigrey, P. J.; Nairns, D. P.; Macdiarmid, A. G.; Heeger, A. J., Organic Batteries - Reversible N-Type and P-Type Electrochemical Doping of Polyacetylene (Ch)X. *J. Chem. Soc.-Chem. Commun.* **1981,** (7), 317-319.

(117) Patil, A. O.; Ikenoue, Y.; Wudl, F.; Heeger, A. J., Water-Soluble Conducting Polymers. *J. Am. Chem. Soc.* **1987,** *109* (6), 1858-1859.

(118) Grot, W. G., Sulfonation of Acetone with Fuming Sulfuric Acid and Some Reations of Propanone-1,3-Disulfonic Acid. *Journal of Organic Chemistry* **1965,** *30* (2), 515-518.

(119) Burgmayer, P.; Murray, R. W., Ion Gate Electrodes - Polypyrrole as a Switchable Ion Conductor Membrane. *J. Phys. Chem.* **1984,** *88* (12), 2515-2521.

(120) Krieger, J. H.; Trubin, S. V.; Vaschenko, S. B.; Yudanov, N. F. In *Molecular Analogue Memory Cell Based on Electrical Switching and Memory in Molecular Thin Films*, Elsevier Science Sa: **2001**; pp 199-202.

(121) Smits, J. H. A.; Meskers, S. C. J.; Janssen, R. A. J.; Marsman, A. W.; de Leeuw, D. M., Electrically Rewritable Memory Cells from Poly(3-Hexylthiophene) Schottky Diodes. *Adv. Mater.* **2005,** *17* (9), 1169-1174.
(122) Wu, J.; McCreery, R. L., Solid-State Electrochemistry in Molecule/Tio2 Molecular Heterojunctions as the Basis of the Tio2 "Memristor". *J. Electrochem. Soc.* **2009,** *156* (1), P29-P37.
(123) Ziegler, M. M.; Stan, M. R., Cmos/Nano Co-Design for Crossbar-Based Molecular Electronic Systems. *Nanotechnology, IEEE Transactions on* **2003,** *2* (4), 217-230.
(124) Mustafa, J.; Waser, R., A Novel Reference Scheme for Reading Passive Resistive Crossbar Memories. *Nanotechnology, IEEE Transactions on* **2006,** *5* (6), 687-691.
(125) Liu, Y. Fabrication and Characterization of Polypyrrole Au Bilayer Microactuators for Bio-Mems Applications. University of Maryland Maryland, **2005**.
(126) Liew, M. J.; Roy, S.; Scott, K., Development of a Non-Toxic Electrolyte for Soft Gold Electrodeposition: An Overview of Work at University of Newcastle Upon Tyne. *Green Chem.* **2003,** *5* (4), 376-381.
(127) Rohm and Haas. http://www.rohmhaas.com/wcm/index.page.
(128) Baughman, R. H., Conducting Polymer Artificial Muscles. *Synthetic Metals* **1996,** *78*, 339-353.
(129) Baughman, R. H.; Shacklette, L. W.; Elsenbaumer, R. L.; Plichta, E. J.; Becht, C., Micro Electromechanical Actuators Based on Conducting Polymers. *Topics in Molecular Organization and Engineering* **1991,** *7* (Mol. Electron.), 267-89.
(130) Della Santa, A.; De Rossi, D.; Mazzoldi, A., Characterization and Modeling of a Conducting Polymer Muscle-Like Linear Actuator. *Smart Materials and Structures* **1997,** *6* (1), 23-34.
(131) Lewis, T. W.; Spinks, G. M.; Wallace, G. G.; DeRossi, D.; Pachetti, M., Development of an All Polymer Electromechanical Actuator. *Abstr. Pap. Am. Chem. Soc.* **1997,** *214*, 284.
(132) Sansinena, J. M.; Olazabal, V.; Otero, T. F.; daFonseca, C. N. P.; DePaoli, M. A., A Solid State Artificial Muscle Based on Polypyrrole and a Solid Polymeric Electrolyte Working in Air. *Chem. Commun.* **1997,** (22), 2217-2218.
(133) Environmental Protection Agency. http://www.epa.gov/.
(134) Okuzaki, H.; Kunugi, T., Adsorption-Induced Chemomechanical Behavior of Polypyrrole Films. *J. Appl. Polym. Sci.* **1997,** *64* (2), 383-388.
(135) Okuzaki, H.; Kunugi, T., Electrically Induced Contraction of Polypyrrole Film in Ambient Air. *J. Polym. Sci. Pt. B-Polym. Phys.* **1998,** *36* (9), 1591-1594.
(136) Okuzaki, H.; Kuwabara, T.; Kunugi, T., Theoretical Study of Sorption-Induced Bending of Polypyrrole Films. *J. Polym. Sci. Pt. B-Polym. Phys.* **1998,** *36* (12), 2237-2246.
(137) Okuzaki, H.; Kondo, T.; Kunugi, T., Characteristics of Water in Polypyrrole Films. *Polymer* **1999,** *40* (4), 995-1000.
(138) Okuzaki, H.; Funasaka, K., Electro-Responsive Polypyrrole Film Based on Reversible Sorption of Water Vapor. *Synthetic Metals* **2000,** *108* (2), 127-131.
(139) Okuzaki, H.; Kuwabara, T., Temperature Dependence of Humido-Responsive Bending of Conducting Polymer Films. *Synthetic Metals* **2005,** *153* (1-3), 101-104.
(140) Tseng, R. J.; Huang, J. X.; Ouyang, J.; Kaner, R. B.; Yang, Y., Polyaniline Nanofiber/Gold Nanoparticle Nonvolatile Memory. *Nano Lett.* **2005,** *5* (6), 1077-1080.
(141) Wallace, G. G., Conductive Electroactive Polymers: Intelligent Materials Systems. **2002**, 248.

(142) Diaz, A. F.; Lacroix, J. C., Synthesis of Electroactive Conductive Polymer-Films - Electrooxidation of Heteroaromatic-Compounds. *New J. Chem.* **1988,** *12* (4), 171-180.
(143) Peres, R. C. D.; Pernaut, J. M.; Depaoli, M. A., Polypyrrole Dodecyl-Sulfate - Effects of Different Synthesis Conditions. *J. Polym. Sci. Pol. Chem.* **1991,** *29* (2), 225-231.
(144) Kupila, E. L.; Kankare, J., Electropolymerization of Pyrrole - Effects of Ph and Anions on the Conductivity and Growth-Kinetics of Polypyrrole. *Synthetic Metals* **1993,** *55* (2-3), 1402-1405.
(145) Erwin, S. C.; Zu, L. J.; Haftel, M. I.; Efros, A. L.; Kennedy, T. A.; Norris, D. J., Doping Semiconductor Nanocrystals. *Nature* **2005,** *436* (7047), 91-94.
(146) Rahman, G. M. A.; Zhao, J.-H.; Thomson, D. J.; Freund, M. S., Compensation Doping in Conjugated Polymers: Engineering Dopable Heterojunctions for Modulating Conductivity in the Solid State. *J. Am. Chem. Soc.* **2009**.
(147) Zhao, H.; Price, W. E.; Teasdale, P. R.; Wallace, G. G., Transport across Stand-Alone Conducting Polypyrrole Membranes Containing Dodecyl-Sulfate Counterions. *React. Polym.* **1994,** *23* (2-3), 213-220.
(148) Zhao, H.; Price, W. E.; Wallace, G. G. In *Effect of the Counterion Employed During Synthesis on the Properties of Polypyrrole Membranes*, Elsevier Science Bv: **1994**; pp 47-56.
(149) Moss, B. K.; Burford, R. P.; Skyllas-Kazacos, M., Electrically Conducting Polypyrroles. *Materials Forum* **1989,** *13* (1), 35-42.
(150) Sze, S. M., *Semiconductor Devices, Physics and Technology*. 2nd ed.; Wiley: New York, **2002**; p 564.
(151) Antoniadis, H.; Hsieh, B. R.; Abkowitz, M. A.; Jenekhe, S. A.; Stolka, M., Photogeneration and Photoluminescence Studies in Bilayer Structures Containing Poly(P-Phenylene Vinylene) and Molecularly Doped Polymers. **1994**, 381-390.
(152) Campbell, A. J.; Weaver, M. S.; Lidzey, D. G.; Bradley, D. D. C., Bulk Limited Conduction in Electroluminescent Polymer Devices. *J. Appl. Phys.* **1998,** *84* (12), 6737-6746.
(153) Lampert, M. A.; Mark, P., *Current Injection in Solids*. Academic Press: New York, 1970; p 351.
(154) Blom, P. W. M.; deJong, M. J. M.; vanMunster, M. G., Electric-Field and Temperature Dependence of the Hole Mobility in Poly(P-Phenylene Vinylene). *Phys. Rev. B* **1997,** *55* (2), R656-R659.
(155) Blom, P. W. M.; de Jong, M. J. M.; Liedenbaum, C., Device Physics of Polymer Light-Emitting Diodes. *Polym. Adv. Technol.* **1998,** *9* (7), 390-401.
(156) Martens, H. C. F.; Pasveer, W. F.; Brom, H. B.; Huiberts, J. N.; Blom, P. W. M., Crossover from Space-Charge-Limited to Recombination-Limited Transport in Polymer Light-Emitting Diodes. *Phys. Rev. B* **2001,** *63* (12), 125328-1-7.
(157) Abkowitz, M. A.; Antoniadis, H.; Facci, J. S.; Hsieh, B. R.; Stolka, M. In *Space-charge-limited Injection into Trap-Free Polymers*, Elsevier Science Sa Lausanne: **1994**; pp 187-191.
(158) Bozano, L.; Carter, S. A.; Scott, J. C.; Malliaras, G. G.; Brock, P. J., Temperature- and Field-Dependent Electron and Hole Mobilities in Polymer Light-Emitting Diodes. *Appl. Phys. Lett.* **1999,** *74* (8), 1132-1134.
(159) Campbell, I. H.; Davids, P. S.; Smith, D. L.; Barashkov, N. N.; Ferraris, J. P., The Schottky Energy Barrier Dependence of Charge Injection in Organic Light-Emitting Diodes. *Appl. Phys. Lett.* **1998,** *72* (15), 1863-1865.

(160) deMello, J. C.; Tessler, N.; Graham, S. C.; Friend, R. H., Ionic Space-Charge Effects in Polymer Light-Emitting Diodes. *Phys. Rev. B* **1998,** *57* (20), 12951-12963.
(161) Gill, W. D., Drift Mobilities in Amorphous Charge-Transfer Complexes of Trinitrofluorenone and Poly-N-Vinylcarbazole. *J. Appl. Phys.* **1972,** *43* (12), 5033-5040.
(162) Arwin, H.; Aspnes, D. E.; Bjorklund, R.; Lundstrom, I., Dielectric Function of Thin Polypyrrole and Prussian Blue Films by Spectroscopic Ellipsometry. *Synthetic Metals* **1983,** *6* (4), 309-316.
(163) Kim, Y. D.; Song, I. C., Electrorheological and Dielectric Properties of Polypyrrole Dispersions. *J. Mater. Sci.* **2002,** *37* (23), 5051-5055.
(164) Pei, Q. B.; Yu, G.; Zhang, C.; Yang, Y.; Heeger, A. J., Polymer Light-Emitting Electrochemical-Cells. *Science* **1995,** *269* (5227), 1086-1088.
(165) Leger, J. M.; Carter, S. A.; Ruhstaller, B., Recombination Profiles in Poly[2-Methoxy-5-(2-Ethylhexyloxy)-1,4-Phenylenevinylene] Light-Emitting Electrochemical Cells. *J. Appl. Phys.* **2005,** *98* (12), 124907-1-7.
(166) Pingree, L. S. C.; Rodovsky, D. B.; Coffey, D. C.; Bartholomew, G. P.; Ginger, D. S., Scanning Kelvin Probe Imaging of the Potential Profiles in Fixed and Dynamic Planar Lecs. *J. Am. Chem. Soc.* **2007,** *129* (51), 15903-15910.
(167) Smith, D. L., Steady State Model for Polymer Light-Emitting Electrochemical Cells. *J. Appl. Phys.* **1997,** *81* (6), 2869-2880.
(168) Roling, B.; Murugavel, S.; Heuer, A.; Luhning, L.; Friedrich, R.; Rothel, S., Field-Dependent Ion Transport in Disordered Solid Electrolytes. *Phys. Chem. Chem. Phys.* **2008,** *10* (29), 4211-4226.
(169) Strukov, D. B.; Williams, R. S., Exponential Ionic Drift: Fast Switching and Low Volatility of Thin-Film Memristors. *Appl. Phys. A-Mater. Sci. Process.* **2009,** *94* (3), 515-519.
(170) Mitchell, G. R.; Geri, A., Molecular-Organization of Electrochemically Prepared Conducting Polypyrrole Films. *J. Phys. D-Appl. Phys.* **1987,** *20* (11), 1346-1353.
(171) Pruneanu, S.; Resel, R.; Leising, G.; Brie, M.; Graupner, W.; Oniciu, L., Structural Investigations on Polypyrrole and Poly(Vinyl Chloride)-Polypyrrole Composite Films. *Mater. Chem. Phys.* **1997,** *48* (3), 240-245.
(172) Warren, M. R.; Madden, J. D., A Structural, Electronic and Electrochemical Study of Polypyrrole as a Function of Oxidation State. *Synthetic Metals* **2006,** *156* (9-10), 724-730.
(173) Yamaura, M.; Sato, K.; Hagiwara, T.; Iwata, K., Memory Effect of Electrical-Conductivity Upon the Counter-Anion Exchange of Polypyrrole Films. *Synthetic Metals* **1992,** *48* (3), 337-354.
(174) Jang, K. S.; Moon, B.; Oh, E. J.; Hong, J. H., Characterization of Stretchable Polypyrrole Films Prepared by Chemical and Electrochemical Method. *Polym.-Korea* **2003,** *27* (4), 323-329.
(175) Shaktawat, V.; Jain, N.; Saxena, R.; Saxena, N. S.; Sharma, K.; Sharma, T. P., Temperature Dependence of Electrical Conduction in Pure and Doped Polypyrrole. *Polym. Bull.* **2006,** *57* (4), 535-543.
(176) Davidson, R. G.; Hammond, L. C.; Turner, T. G.; Wilson, A. R., An Electron and X-Ray Diffraction Study of Conducting Polypyrrole/Dodecyl Sulfate. *Synthetic Metals* **1996,** *81* (1), 1-4.
(177) Xu, G., A Novel Model for the Ionic Conducting Polymers with Non-Arrhenius Temperature-Dependence. *J. Phys.-Condes. Matter* **1994,** *6* (30), 5833-5837.